

Dissertation

# Real-Time Geometry Based Channel Emulation and Estimation

ausgeführt zum Zwecke der Erlangung des akademischen Grades  
eines Doktors der technischen Wissenschaften

eingereicht an der  
Technischen Universität Wien  
Fakultät für Elektrotechnik und Informationstechnik

von  
Dipl.-Ing. Markus Hofer

Wien, Juni 2019



TECHNISCHE  
UNIVERSITÄT  
WIEN

Supervisor

Priv.-Doz. DI Dr.techn. Thomas Zemen  
Institute for Telecommunications  
Technische Universität Wien, Austria

Begutachter

Prof. Ph.D. Fredrik Tufvesson  
Dept. of Electrical and Information Technology  
Lund University, Sweden

Ao. Prof. Dr.techn. Florian Kaltenberger  
Dept. of Communication Systems  
EURECOM, France

# Kurzfassung

Mit der Entwicklung von 5G sind eine Vielzahl von neuen Anwendungsfällen in den drei großen Kategorien massive machine type communications, enhanced mobile broadband und ultra-reliable and low latency communication (URLLC) vorgesehen. URLLC verspricht neue Technologien wie selbstfahrende Autos, Industrieautomation, Augmented Reality, taktiles Internet und viele mehr, zu ermöglichen. An die Latenz und Zuverlässigkeit von URLLC Links werden hohe Anforderungen gestellt, welches es zu einem anspruchsvollen Forschungsfeld macht.

In dieser Dissertation werden zwei Aspekte betrachtet, um URLLC zu ermöglichen. Im ersten Teil der Dissertation wird der wiederholbare Test und die Validierung von drahtlosen Kommunikationssystemen in einer Laborumgebung unter Verwendung von geometrie-basierter Echtzeitkanalemulation präsentiert. Tests im Labor bieten den Vorteil der Wiederholbarkeit und Reproduzierbarkeit, während Tests auf der Straße kostspielig und schwer zu wiederholen sind. Für Fahrzeugszenarien weist die drahtlose Kommunikation zwischen Sender und Empfänger Mehrwegeausbreitung auf, die zu einem nicht stationären zeit- und frequenzselektiven Schwundprozess am Empfänger führt. Der Schwundprozess beinhaltet sich kontinuierlich ändernde Pfadverzögerungen und Doppler-Verschiebungen welche von der Position, Geschwindigkeit und der Umgebung des Kommunikationssystems abhängen. Um URLLC Verbindungen zu ermöglichen, muss das Kommunikationssystem in einer solchen Umgebung auf wiederholbare Art und Weise getestet werden, einschließlich der Möglichkeit von Echtzeit-Updates der Trajekturen welche durch Regelalgorithmen angepasst werden. Aktuelle Kanalemulationslösungen basieren auf einem angezapften Laufzeitkettenmodell, welches nur Pfadverzögerungen als ganzzahliges Vielfaches der Abtastzeit erlaubt. Um dieses Problem zu lösen, haben wir eine geometriebasierte Echtzeit Kanalemulation entwickelt. Der Emulator ist als eine Kombination aus einem Multicore-Computer und einer frei programmierbaren Funkplattform implementiert. Auf dem Multicore-Computer wird das geometriebasierte Kanalmodell in Echtzeit in Abhängigkeit der Positionen, Geschwindigkeiten und Beschleunigungen der sich bewegenden Objekte aktualisiert, während die frei programmierbare Funkplattform für die zeitvariante Faltung der Kanalimpulsantwort mit dem zu übertragenden Signal verwendet wird. Die Datenrate der Kanalimpulsantwort wächst quadratisch mit der emulierten Bandbreite und wird schnell zum Engpass, wenn die zeitvariante Kanalimpulsantwort

zwischen den Geräten übertragen werden muss. Um die Datenrate zu reduzieren, wird ein Unterraumprojektionsalgorithmus mit reduziertem Rang basierend auf diskreten abgeflachten sphäroidalen Sequenzen verwendet, um die Kanalimpulsantwort mit einer kleinen Anzahl von Basiskoeffizienten zu approximieren. Der Algorithmus ermöglicht eine Echtzeit Implementierung des geometriebasierten Kanalmodells. Die Funktionalität des Emulators wird durch den RUSK Lund Channel Sounder validiert, welcher die emulierte Kanalimpulsantwort misst. Schließlich wird der Echtzeit-Kanalemulator bei Fahrzeug-in-der Schleife Tests verwendet.

Im zweiten Teil der Dissertation werden adaptive, iterative nicht-stationäre Kanalschätzer für nicht zusammenhängende, äquidistante Pilotmuster vorgestellt. Konkret wird der Kanalschätzer auf den Downlink von long term evolution (LTE) angewendet. Ein Hypothesentest wird verwendet, um die statistischen Eigenschaften der aktuellen Kanalrealisierung auf Framebasis zu bestimmen. Dies ermöglicht eine schnellere Konvergenz des iterativen Schätzalgorithmus. Die Anzahl der Hypothesen für den Hypothesentest wird durch numerische Simulationen optimiert, was eine Reduktion der Rechenkomplexität im Empfänger ermöglicht. Schließlich wird eine speziell ausgewählte Hypothesenwahl vorgestellt, die einen guten Kompromiss zwischen Rechenkomplexität und Leistung bietet.

# Abstract

With the development of 5G, a variety of use-cases in three broad categories, massive machine type communications, enhanced mobile broadband and ultra-reliable and low latency communication (URLLC), are envisioned. URLLC promises to enable new technologies such as self driving cars, industry automation, augmented reality, the tactile internet and many more. Stringent requirements are placed on the latency and the reliability of URLLC links which makes it a challenging research field. In this thesis two aspects to enable URLLC are considered.

In the first part of the thesis, the repeatable test and validation of wireless communication systems in a laboratory environment using *real-time geometry based channel emulation* is presented. Tests in a laboratory environment offer the benefit of repeatability and reproducibility, while testing on the road is costly and difficult to repeat. In vehicular scenarios the wireless communication channel between transmitter and receiver exhibits multi-path propagation, leading to a non-stationary time- and frequency selective fading process at the receiver. The fading process is the result of continuously changing path delays and Doppler shifts, depending on the position, velocity and the environment of the communication system. To enable URLLC links, the communication system has to be tested in such an environment in a repeatable fashion including the possibility of real-time trajectory updates by vehicular control algorithms (e.g. connected autonomous vehicles or advanced driver assistance systems). Current channel emulator solutions are based on a tap delay line model, which only allows for path delays as integer multiples of the sampling time. To tackle this problem, we investigate real-time geometry-based channel emulation. The emulator is implemented using a multi core computer in combination with a software defined radio. On the multi-core computer, the geometry-based channel model is updated in real-time dependent on the positions, velocities and acceleration of moving objects, while the software defined radio is used to perform the time-variant convolution of the channel impulse response with the transmitted signal. The data rate needed for the streaming of the channel impulse response between devices grows quadratically with the emulated bandwidth and quickly becomes a bottleneck. To reduce the data rate, a reduced-rank subspace projection algorithm, based on discrete prolate spheroidal sequences to approximate the channel impulse response with a small amount of basis coefficients, is utilized. The algorithm allows for a real-time implementation of the geometry-based channel model. The functionality of the emu-

lator is validated by the RUSK Lund channel sounder, which measures the emulated channel impulse response. Lastly, the real-time channel emulator is validated in a vehicle-in-the-loop test on a proofing ground.

In the second part of the thesis, an adaptive iterative non-stationary channel estimation algorithm for non-contiguous, equidistant pilot patterns is presented for the LTE downlink. A hypothesis test is utilized to determine the characteristics of the current channel realization on a per frame basis. This allows for a faster convergence of the iterative channel estimation algorithm. The number of hypotheses for the hypothesis test is optimized using numerical simulations, which enables a computational complexity reduction at the receiver side. Finally, a specially chosen hypothesis setup is presented, that offers a good trade-off between computational complexity and performance.

# Acknowledgment

First of all, I want to express my gratitude to my advisor Thomas Zemen. Thanks to his guidance, continuous support and by sharing his knowledge he made pursuing this PhD possible.

I want to thank Fredrik Tufvesson, who agreed to review my thesis and act as an examiner, and who, furthermore, gave me the great opportunity of a research visit at Lund University to perform measurements. In this context, I would also like to thank Dimitrios Vlastaras for his time and great support during my stay.

I am grateful to Florian Kaltenberger, for showing interest in my work and acting as an examiner. His work served as one of the cornerstones of my research.

I want to thank all my colleagues, whom I had and have the pleasure to spend time with, for their continuous support, feedback and constructive criticism, that helped to greatly improve the quality of this work. I would especially like to thank my former colleagues of the Telecommunication Research Center Vienna (ftw.), Zhi-nan Xu, Martin Wolkerstorfer, Mingming Gan, Sandra Drakulic and Driton Statovci with whom I started my PhD journey for many fruitful discussions, on- and off-topic, putting me back on track when needed and for creating a welcoming atmosphere, which made working there pleasant. I would also like to thank my new colleagues at the AIT Austrian Institute of Technology, David Löschenbrand, Stefan Zelenbaba, Anja Dakic, Laura Bernadó and Benjamin Rainer, who helped me to gain knowledge and perspective in various aspects and who make working in the office highly enjoyable. Also, I would like to thank Axelle, Manuela, Marina, Birgit, Martin, Carina, Mario, Agi and Dieter, just to name a few, for all the joint lunches and fun get-togethers that make AIT a place you enjoy working at.

A great thank you goes to all my friends friends, for their time, open ears in tough times and ensuring the much needed balance outside of work by putting my mind on other (equally as) important aspects of life. Particularly, I would like to thank Martin T., Martin M., Michael, Josep, Simon, Ines, Fabian, Max, Stefan, Dominik, Paul, Jenny, Maria, Marlene and Norbert. Thanks for being who you are.

Abschließend möchte ich meiner Familie von ganzem Herzen für ihre kontinuierliche Unterstützung, ihr Verständnis und ihre Liebe danken, ohne die ich jetzt nicht da wäre wo ich bin.

Most of the research work in this thesis has been carried out in the project "RE-ALTIME", a joint effort between the AIT and the Austrian Research Promotion

Agency (FFG).

# Contents

<b>1</b>	<b>Introduction</b>	<b>1</b>
1.1	Scope . . . . .	1
1.1.1	Ultra-Reliable and Low Latency Communication . . . . .	2
1.1.2	Wireless Communication Channel . . . . .	2
1.2	Outline and Contribution . . . . .	3
1.3	Notation . . . . .	6
<b>I</b>	<b>Real Time Wireless Channel Emulation</b>	<b>7</b>
<b>2</b>	<b>Wireless Channel Models</b>	<b>9</b>
2.1	Fading Effects . . . . .	9
2.2	System Theoretic Description of Wireless Channel . . . . .	11
2.2.1	SISO Channel Models . . . . .	12
2.2.2	MIMO Channel Model . . . . .	13
2.3	Stochastic Description of the Wireless Channel . . . . .	14
2.3.1	Wide-Sense-Stationary Uncorrelated-Scattering (WSSUS) . . . . .	14
2.3.2	Non-WSSUS . . . . .	15
2.4	Channel Model Categorization . . . . .	16
<b>3</b>	<b>Wireless Channel Emulation</b>	<b>19</b>
3.1	State of the Art Channel Emulation . . . . .	20
3.1.1	Commercially Available Channel Emulators . . . . .	20
3.1.2	Software Defined Radio Based Channel Emulators . . . . .	21
3.1.3	Shortcomings of current Channel Emulator Solutions . . . . .	22
3.2	System Model . . . . .	22
3.2.1	Non-Stationary Fading Process as Concatenation of Stationarity Regions . . . . .	23
3.2.2	Channel Impulse Response Data Rate . . . . .	26
3.2.3	Geometry-Based Channel Emulation Architecture . . . . .	27
3.2.4	Basis Expansion Model . . . . .	29
3.2.5	Approximate Basis Projection . . . . .	30

3.2.6	Time-Variant Channel Impulse Response . . . . .	32
3.3	Error Analysis . . . . .	33
3.3.1	Basis Expansion Model Bias . . . . .	34
3.3.2	Approximate Basis Projection Bias . . . . .	34
3.3.3	Error Analysis of the Piecewise Constant Doppler Assumption . . . . .	35
3.3.4	Narrow Band Approximation Error . . . . .	37
3.4	Data Rate and Complexity Analysis . . . . .	38
3.4.1	Data Rate Analysis for PC-SDR Link . . . . .	38
3.4.2	Complexity Reduction Analysis . . . . .	39
3.5	Hardware Implementation Aspects . . . . .	40
3.5.1	Software Defined Radio . . . . .	40
3.5.2	Channel Impulse Response Reconstruction on FPGA . . . . .	40
3.5.3	Local Oscillator Leakage . . . . .	41
3.6	Measurement and Validation Setup . . . . .	41
3.6.1	Numerical Simulation . . . . .	42
3.6.2	Emulation Parameters . . . . .	42
3.6.3	Measurement Description . . . . .	42
3.7	Measurement Results . . . . .	45
3.7.1	One-Path Channel Model . . . . .	45
3.7.2	Geometry-Based Stochastic Channel Model . . . . .	48
3.7.3	ETSI TDL Channel Models . . . . .	53
<b>4</b>	<b>Channel Emulation in Vehicle-in-the-Loop Tests</b>	<b>57</b>
4.1	Scenario Description . . . . .	58
4.2	Vehicle-in-the-Loop Tests . . . . .	59
4.2.1	Description of the ViL Test . . . . .	59
4.2.2	Wireless Channel Emulation . . . . .	60
4.3	Measurement and Validation . . . . .	62
4.4	Discussion . . . . .	65
<b>II</b>	<b>Adaptive Iterative Channel Estimation</b>	<b>67</b>
<b>5</b>	<b>Adaptive Iterative Non-Stationary Channel Estimation for LTE Communications</b>	<b>69</b>
5.1	Introduction . . . . .	69
5.2	System Model . . . . .	70
5.3	Iterative Channel Estimation . . . . .	72
5.3.1	Wiener Filter . . . . .	73
5.3.2	Soft Symbol Calculation . . . . .	73

5.3.3	Robust Reduced Rank Approximation . . . . .	75
5.4	Adaptive Subspace Selection for a Non-Contiguous Equidistant Pilot Grid . . . . .	76
5.4.1	Non-Contiguous, Equidistant Pilot Pattern Partitioning . . . . .	77
5.4.2	Hypothesis Design . . . . .	79
5.4.3	Hypothesis Test . . . . .	80
5.5	Simulation Results . . . . .	81
5.6	Determining the Optimum Number of Hypotheses . . . . .	85
5.6.1	System Model for a Frequency Flat Channel . . . . .	85
5.6.2	Numerical Optimization of the Number of Hypotheses . . . . .	86
5.6.3	Specifically Chosen Hypotheses Setup . . . . .	87
5.6.4	Simulation Results . . . . .	87
<b>6</b>	<b>Conclusion</b>	<b>93</b>
6.1	Summary . . . . .	93
6.2	Key Findings . . . . .	95
6.3	Outlook . . . . .	96
<b>A</b>	<b>Hypothesis Test for the Frequency Flat Channel</b>	<b>99</b>
<b>B</b>	<b>List of Acronyms</b>	<b>101</b>
	<b>Bibliography</b>	<b>105</b>



Die approbierte gedruckte Originalversion dieser Dissertation ist an der TU Wien Bibliothek verfügbar.  
The approved original version of this doctoral thesis is available in print at TU Wien Bibliothek.

# List of Figures

1.1	5G use case categories [1]. . . . .	1
2.1	Influence of the environment on wireless communication. . . . .	10
2.2	Relation between linear-time variant system functions [2]. . . . .	11
2.3	Example of a SISO communication system with the transmit filter $h_{\text{TX}}(\tau)$ and the receive filter $h_{\text{RX}}(\tau)$ . . . . .	12
2.4	Example of a MIMO communication system with $m$ transmit antennas and $n$ receive antennas. Different transmit filters $h_{j,\text{TX}}(\tau)$ and receive filters $h_{i,\text{RX}}(\tau)$ are utilized. . . . .	14
3.1	Schematic representation of a channel emulator implemented in the digital domain to test communication systems. The transmitted signal is convolved with the emulated time-variant channel impulse response. . . . .	19
3.2	Piecewise constant Doppler shift approximation of the instantaneous Doppler shift $\omega_p$ for different stationarity regions. . . . .	25
3.3	Linear change of delay within stationarity regions. . . . .	25
3.4	Geometry-based channel emulator structure . . . . .	27
3.5	Frame structure of periodic transmission of basis coefficients for stationarity regions $s$ . . . . .	28
3.6	Indicator function $e_{\text{FD}}^2(\Delta\omega_p) < E_{\text{th}}^2$ for piecewise constant Doppler shift vs. Doppler shift change and stationarity region length $T_{\text{stat}}$ . The white region shows the area where the condition is satisfied. . . . .	36
3.7	Exemplary narrowband approximation error vs. time and frequency index for $\omega_{\text{pmax}} = 2.11$ kHz, $T_{\text{stat}} = 256$ $\mu$ s, $f_c = 5.7$ GHz and $T_C = 50$ ns (cf. Table 3.2). . . . .	39
3.8	Measurement setup for the validation. . . . .	43
3.9	Comparison of the normalized PDPs for one propagation path with changing Doppler shift from $-2$ kHz to $2$ kHz. . . . .	46
3.10	Comparison of the normalized DSDs for one propagation path with changing Doppler shift from $-2$ kHz to $2$ kHz. . . . .	47
3.11	Top view of the investigated intersection (N55°42'38", E13°11'14") in the city of Lund with the trajectories of TX and RX respectively [3] . . . . .	48
3.12	Scatterer distribution of the channel model for a road intersection [3] . . . . .	49

3.13	Comparison of the normalized PDPs for the road intersection scenario.	50
3.14	Comparison of the normalized DSDs for the road intersection scenario.	51
3.15	Comparison of PDP and DSD error for a road intersection scenario.	52
3.16	Comparison of the second order statistics of the road intersection scenario.	53
3.17	Comparison of the normalized PDPs of ETSI channel model rural LOS	54
3.18	Comparison of the normalized DSDs of ETSI channel model rural LOS	55
4.1	Illustration of the basic scenarios.	59
4.2	Test track recreated in simulation.	60
4.3	Schematics of wireless channel emulation in ViL.	61
4.4	Trajectories of the vehicles for the “sight blocked” scenario and the geometry considered for real-time channel emulation with the GSCM. The white trajectory corresponds to the test vehicle, the yellow trajectory to the sight blocking VW T5 and the black trajectory to the crossing vehicle (VW Passat)	62
4.5	Average RSSI with (dashed line) 95 % confidence intervals (filled area) of the ViL test and the measurement on the proving ground versus the travel distance for the “sight blocked” scenario	63
4.6	PER of the ViL test and the measurement on the proving versus the travel distance for the “sight blocked” scenario.	64
5.1	SISO LTE downlink system model	71
5.2	OFDM time-frequency grid of one LTE subframe with normal CP length and partitioned index sets $\mathcal{I}_c$ and $\mathcal{I}_d$	78
5.3	MSE vs. Doppler bandwidth $\nu_D$ for $\text{SNR} \in \{0, 10\}$ dB for adaptive subspace selection in the time domain with $N_{\text{SUBF}} \in \{1, 2\}$	82
5.4	MSE vs. normalized PDP support $\theta_P$ for $\text{SNR} \in \{0, 10\}$ dB for adaptive subspace selection in the frequency domain	83
5.5	PER vs. number of iterations for $\text{SNR} = 13$ dB and relative velocities $v \in \{50, 200, 400\}$ km/h; $R = 0.479$ , 16-QAM symbol alphabet	84
5.6	One sided normalized Doppler support and dimension for the hypothesis setup ‘Dim. max’ (green) and ‘Dim. mid’ (magenta); $\Delta_t = 1$ , $M = 42$ , $v_{\text{max}} = 200$ km/h, $\text{SNR} = 10$ dB	88
5.7	$\overline{\text{MSE}}_{A_i}$ vs. hypothesis size $A_i$ for a time-variant frequency-flat channel; $\Delta_t = 1$ , $M = 42$ , $v_{\text{max}} = 200$ km/h, $\text{SNR} = 10$ dB	89
5.8	$\overline{\text{MSE}}_b$ vs. $\nu_D$ ; $\Delta_t = 1$ , $M = 42$ , $v_{\text{max}} = 200$ km/h, $\text{SNR} = 10$ dB	91
5.9	$\overline{\text{MSE}}_b$ vs. $A_i$ ; $\Delta_t = 1$ , $M = 42$ , $v_{\text{max}} = 200$ km/h, $\text{SNR} = 10$ dB	92

# 1 Introduction

## 1.1 Scope

5G, as the successor to 4G, aims to be a leap forward in terms of data rates, latency, massive connectivity, network reliability and energy efficiency [4]. 5G is envisioned to support a diverse variety of use cases in three broad categories [1, 4–6] as shown in Fig. 1.1.

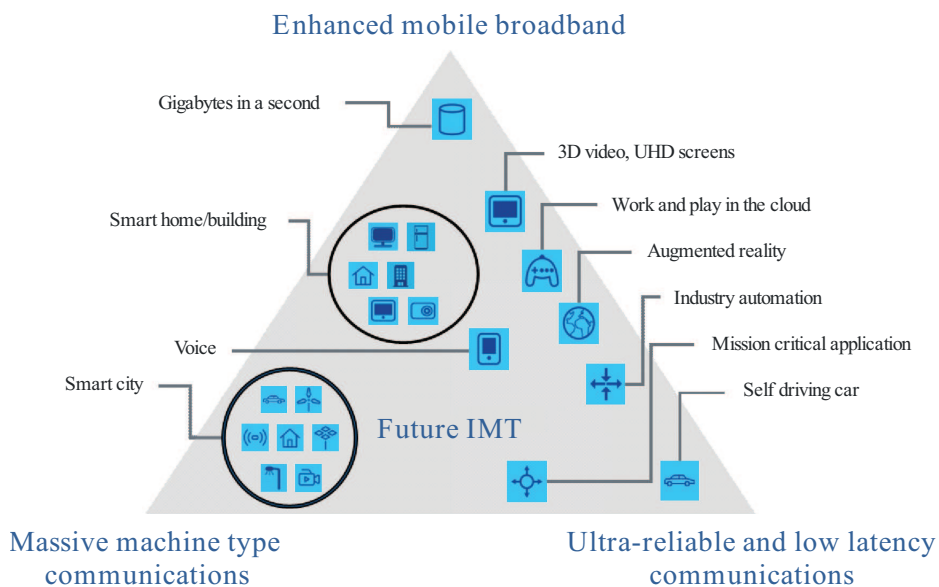


Figure 1.1: 5G use case categories [1].

- Enhanced mobile broadband aims at provisioning high data rates with improved performance.
- Massive machine type communications considers communication of a very large number of devices with low data rate and non-delay-sensitive data.
- Ultra-reliable and low latency communication (URLLC) aims to provide communication links that support stringent latency and reliability requirements of (partly) mission-critical applications

### 1.1.1 Ultra-Reliable and Low Latency Communication

URLLC will play an essential role for time-sensitive applications for different vertical industries such as connected autonomous vehicles, industrial automation, smart grids, tactile internet and more [7–19]. The performance requirements on URLLC depend on the scenario [7, 11, 20].

Consider for instance connected autonomous vehicles in intelligent transportation systems (ITSs) that exchange information over wireless communication links to increase road safety, reduce traffic congestion, minimize fuel consumption and enhance the overall driving experience [7, 15–19]. In fully automated driving systems, real-time control algorithms integrated in the automated vehicle’s control unit, will use this information to adapt the driving route and velocity to the current traffic situation. This will require information to be disseminated among vehicles reliably within short time intervals. The authors of [7] expect links with end-to-end latency of 5-10 ms and a packet error rate (PER)  $< 10^{-5}$ .

In future industrial automation the replacement of cabled connections with wireless communication links will allow reduced manufacturing costs, higher long term reliability and more flexibility [7]. Multiple sensors and actuators (e.g. robots) collaborate within closed-loop control networks utilizing control algorithms that require communication links with latencies  $< 1$  ms and PER  $< 10^{-9}$  for the exchange of information [7–10].

These stringent requirements make URLLC a challenging research field. To enable URLLC, different aspects have to be investigated. While some aspects consider the further development of the core network and mobile edge computing, others consider advancements in the physical layer, like smaller transmission time intervals, different sub-carrier spacing, robust modulation and coding schemes, diversity schemes, grant free access and multi connectivity [10].

### 1.1.2 Wireless Communication Channel

The performance of wireless communication systems is fundamentally determined by the wireless communication channel properties. In vehicular scenarios the wireless communication channel between transmitter (TX) and receiver (RX) exhibits multi path propagation leading to a non-stationary time- and frequency selective fading process at the RX. The statistic of the fading process depends on the position and velocity of TX and RX as well as the environment (i.e. its geometry and physical properties). In industrial environments sensors and actuators move in a surrounding with many metallic reflectors creating a non-stationary time- and frequency-selective fading channel with an increased number of diffuse components.

To validate URLLC, a repeatable test of the investigated aspects together with

real-time control algorithms in the considered scenarios is of utmost importance. Tests in the laboratory have the benefit of easy repeatability and reproducibility, while tests on the road, are typically costly, labor intensive and difficult to repeat. For the test in the laboratory the wireless communication channel has to be emulated in real-time dependent on the environment and the position of the TX and the RX.

Furthermore, advanced channel estimation techniques that adapt to the current channel properties are required to allow for communication links with high reliability.

## 1.2 Outline and Contribution

This thesis is divided into two parts.

In **Part I** of the thesis we present geometry-based real-time wireless channel emulation, which allows for the repeatable test of URLLC communication devices in realistic wireless communication scenarios. A realistic validation requires to update the wireless channel properties in real-time with continuous variations in delay and Doppler shift of each propagation path, according to the change of the position and velocity of TX and RX as well as a moving environment. Part I is outlined as follows:

- **Chapter 2** provides an overview of the theory of wireless channel models. A system theoretic description of channel models by linear time-variant systems is shown. We present single-input single-output (SISO) and multiple-input multiple-output (MIMO) channel models based on a double-directional channel model and discuss the stochastic description of the wireless communication channel. At the end of the chapter, the channel models are classified into deterministic, stochastic and geometry-based stochastic channel models.
- At the beginning of **Chapter 3**, state of the art wireless channel emulators and their short comings to emulate wireless propagation channels with real valued path delays and Doppler shifts are discussed. The mathematical theory of channel emulation is presented and the implementation of a real-time geometry-based channel emulator using a software defined radio (SDR) platform is described. Our emulator can be parameterized by *all known channel models* presented in Chapter 2. In this thesis we specifically focus on non-stationary time-variant wireless vehicular communication channels. We discuss the problem of streaming channel impulse responses (CIRs) with a large number of taps and high streaming bandwidth to the SDR. We show how discrete prolate spheroidal (DPS) sequences can be utilized to find an approximated representation of the CIR, which leads to a significant bandwidth reduction.

A detailed error analysis of the approximation errors is delivered. We show measurements of the emulated CIR conducted with the RUSK Lund channel sounder. Finally, a comparison between numerical simulation and measured emulation is shown.

- In **Chapter 4** real-time channel emulation is applied in a vehicle-in-the-loop (ViL) test of a left turn scenario of a road crossing. We use common-off-the-shelf modems to record the receive signal strength indicator (RSSI) and PER in two scenarios: (a) on the proving round and (b) in a ViL test. The comparison of the results shows that real-time channel emulation can reproduce the effect of realistic wireless communication channels.

In **Part II** we present advanced channel estimation techniques to enable low latency communication links. Especially in vehicular settings low latency communication links require channel estimation techniques that are able to quickly adapt to non-stationary channel statistics on a per frame basis.

- In **Chapter 5** we describe adaptive iterative estimation for LTE downlink for non-stationary channels. We utilize a hypothesis test to estimate the delay and Doppler support of the current channel realization on a per frame basis. We investigate a subspace design using DPS sequences for a non-contiguous, equidistant pilot pattern as used in LTE. Finally, the optimum number of hypotheses for the hypothesis test is investigated numerically and a special hypothesis setup that allows for a good trade-off between computational complexity and performance is presented.

The contributions described in this thesis are presented to a large extent in the following papers:

- [21] M. Hofer and T. Zemen, “Iterative Non-Stationary Channel Estimation for LTE Downlink Communications,” in *2014 IEEE International Conference on Communications Workshops (ICC)*. IEEE, Jun. 2014, pp. 26–31.
- [22] M. Hofer, Z. Xu, and T. Zemen, “On the optimum number of hypotheses for adaptive reduced-rank subspace selection,” in *2015 IEEE 82nd Vehicular Technology Conference (VTC2015-Fall)*, Sep. 2015, pp. 1–5.
- [23] M. Hofer, Z. Xu, and T. Zemen, “Real-time channel emulation of a geometry-based stochastic channel model on a SDR platform,” in *IEEE 18th Int. Works. Signal Process. Adv. Wireless Commun. (SPAWC)*, Sapporo, pp. 1-5 Japan, Jul. 2017.

- [24] M. Hofer, Z. Xu, D. Vlastaras, B. Schrenk, D. Loeschbrand, F. Tufveson, and T. Zemen, "Validation of a real-time geometry-based stochastic channel model for vehicular scenarios," in *IEEE 87th Veh. Technol. Conf. (VTC-Spring)*, Jun. 2018, pp. 1–5
- [25] M. Hofer, Z. Xu, D. Vlastaras, B. Schrenk, D. Loschenbrand, F. Tufveson, and T. Zemen, "Real-time geometry-based wireless channel emulation," *IEEE Transactions on Vehicular Technology*, 2019, pp. 1–15.
- [26] M. Hofer, L. Bernadó, B. Rainer, Z. Xu, G. Temme, S. Khan, D. Behnecke, F. Utesch, M. Mahmood, and T. Zemen, "Evaluation of vehicle-in-the-loop tests for wireless V2X communication," in *IEEE 90th Vehicular Technology Conference (VTC2019-Fall)*, Sep. 2019 to be presented, pp. 1–5.
- [27] Hofer and T. Zemen, "Method for Emulating a Radio Channel," *WO 2018/085769 A1*, May 2018.

## 1.3 Notation

We use the notation presented in Table 1.1 throughout this thesis:

Symbol	Description
$f(t)$	function of a continuous variable
$f[m]$	function of a discrete variable
$\mathbf{a}$	column vector
$a[i]$	$i$ -th element of $\mathbf{a}$
$\mathbf{A}$	matrix
$[\mathbf{A}]_{i,\ell}$	$i, \ell$ -th element of $\mathbf{A}$
$\mathbf{A}^T$	transpose of $\mathbf{A}$
$\mathbf{A}^H$	conjugate transpose of $\mathbf{A}$
$\text{diag}(\mathbf{a})$	diagonal matrix with entries $a[i]$
$\mathbf{I}_Q$	$Q \times Q$ identity matrix
$a^*$	complex conjugate of $a$
$\lfloor a \rfloor$	largest integer, lower or equal than $a \in \mathbb{R}$
$\lceil a \rceil$	smallest integer, greater or equal than $a \in \mathbb{R}$
$ a $	absolute value of $a$
$\ \mathbf{a}\ $	$\ell_2$ norm of vector $\mathbf{a}$
$E_x\{\cdot\}$	expectation of $\{\cdot\}$ with respect to $x$
$\text{vec}(\mathbf{A})$	stacks all columns of matrix $\mathbf{A}$ in a single vector
$j$	$\sqrt{-1}$

Table 1.1: Notation used throughout this thesis.

# Part I

## Real Time Wireless Channel Emulation



Die approbierte gedruckte Originalversion dieser Dissertation ist an der TU Wien Bibliothek verfügbar.  
The approved original version of this doctoral thesis is available in print at TU Wien Bibliothek.

## 2 Wireless Channel Models

In this chapter we present methods to model wireless communication channels. After a short introduction to channel fading effects in Section 2.1, Section 2.2 presents the system theoretic linear time-variant (LTV) description of the wireless channel [2] and discusses the double-directional channel model in more detail. In this thesis, we show SISO and MIMO channel models, however, we will focus on SISO channel models for the implementation. In Section 2.3 the stochastic description of the wireless channel by wide-sense-stationary uncorrelated-scattering (WSSUS) and non-WSSUS processes is discussed. Finally, in Section 2.4 known channel models are categorized.

### 2.1 Fading Effects

The performance of wireless communication systems is fundamentally determined by the wireless communication channel. The transmitted signal interacts with the environment leading to multiple propagation paths due to line-of-sight (LOS), reflection, penetration, diffraction and diffuse scattering. These effects are depicted in Fig. 2.1. At the receive antenna, multiple attenuated and delayed copies of the transmitted signal add up. Hence, they interfere with each other either constructively or destructively. The resulting random process is called fading and manifests itself as a variation of the received signal power in time, frequency and space. Different fading effects can be distinguished [2, 28, 29]:

- The received signal power decreases with increasing distance between TX and RX. For free space propagation the received signal power decreases quadratically with the distance and is modeled by Friis law [2]

$$P_{\text{RX}} = P_{\text{TX}} G_{\text{TX}} G_{\text{RX}} \left( \frac{\lambda}{4\pi d} \right)^2, \quad (2.1)$$

where  $P_{\text{TX}}$  denotes the transmit power,  $G_{\text{TX}}$  and  $G_{\text{RX}}$  denote the gain of the transmit and the receive antenna, respectively. The distance between RX and TX is denoted by  $d$  and  $\lambda$  denotes the wavelength. Friis law is valid in the far field. In case of a different environment, i.e., foliage, terrain, objects in the

surrounding, etc., the received power is proportional to  $d^{-n}$  where  $n$  denotes the path loss coefficient. Depending on the environment  $2 < n < 6$  have been observed [2, 28].

- Shadowing due to hills, large objects or dense vegetation leads to a reduction of the received signal power. Receivers in a shadowed area experience an almost constant reduction of the received signal over a few hundred wavelengths. This effect is called large-scale fading. For most environments it can be modeled by a log-normal distribution [2].
- Small-scale fading is the result of constructive or destructive interference of multi-path components (MPCs) at the RX antenna. If there exists no dominant MPC, e.g. for non-line of sight (NLOS) conditions, the amplitude of the received signal can be modeled by a Rayleigh distribution, if a sufficiently high number of MPC within the same delay bin interfere with each other. This is the consequence of the central limit theorem [2], where a superposition of many statistically independent variables leads to a Gaussian distribution of the field strength and, hence, to a Rayleigh distribution of the amplitude. In case of a dominant MPC, e.g., for LOS conditions, the amplitude is often modeled by a Rician distribution [2, 29].

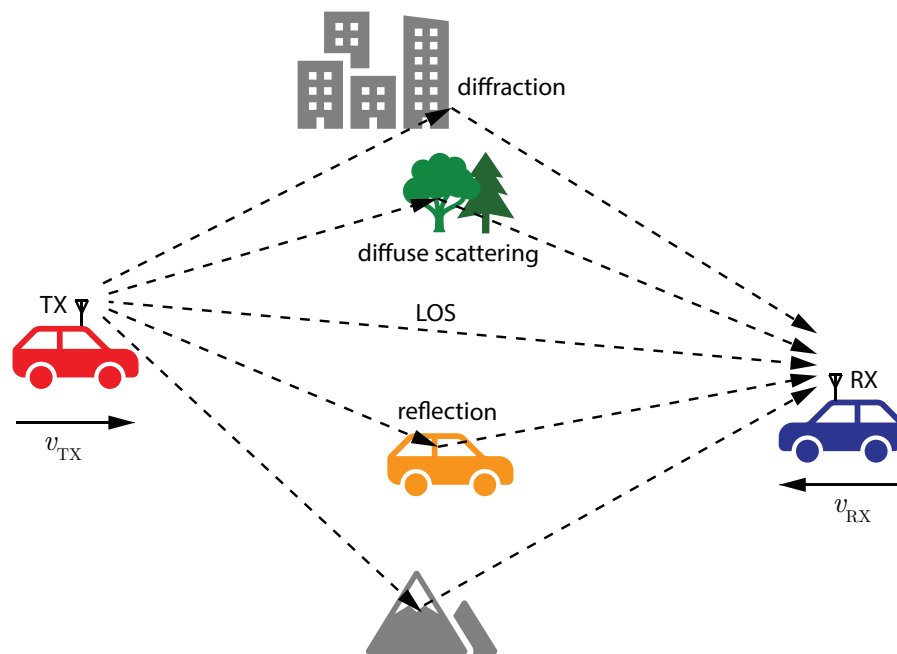


Figure 2.1: Influence of the environment on wireless communication.

## 2.2 System Theoretic Description of Wireless Channel

The effect of the wireless communication channel on a transmitted signal  $x(t)$  can be modeled by an LTV system [2, 28–31]. Four equivalent representations of the system function are linked by the Fourier transform as shown in Figure 2.2.

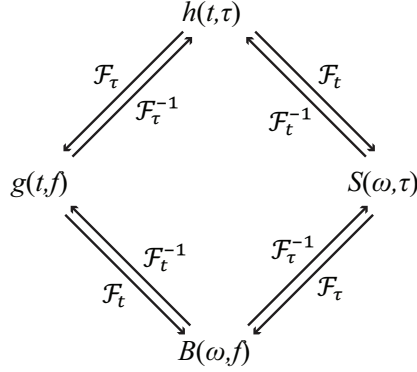


Figure 2.2: Relation between linear-time variant system functions [2].

We will start with the system description by the time-variant channel impulse response (CIR)  $h(t, \tau)$ . The received signal  $y(t)$  is obtained by

$$y(t) = \int_{-\infty}^{\infty} h(t, \tau)x(t - \tau)d\tau, \quad (2.2)$$

where  $t$  denotes absolute time and  $\tau$  time delay, respectively. Alternatively, the channel transfer function (CTF) describes the channel in time  $t$  and frequency  $f$ . It is obtained by the Fourier transform of the CIR with respect to  $\tau$

$$g(t, f) = \int_{-\infty}^{\infty} h(t, \tau)e^{-j2\pi f\tau}d\tau. \quad (2.3)$$

The Doppler-variant impulse response, also known as spreading function  $S(\omega, \tau)$ , is obtained by a Fourier transform of  $h(t, \tau)$  with respect to  $t$

$$S(\omega, \tau) = \int_{-\infty}^{\infty} h(t, \tau)e^{-j2\pi\omega t}dt, \quad (2.4)$$

where  $\omega$  denotes the Doppler shift. The function  $S(\omega, \tau)$  describes how the transmit signal is spread in the delay and the Doppler domain. Finally, the Doppler-variant transfer function  $B(\omega, f)$  is obtained by a Fourier transform of  $S(\omega, \tau)$  with respect to  $\tau$ .

$$B(\omega, f) = \int_{-\infty}^{\infty} S(\omega, \tau)e^{-j2\pi f\tau}d\tau. \quad (2.5)$$

### 2.2.1 SISO Channel Models

Communication systems use filters at the transmitter and at the receiver to ensure the limitation to a specified bandwidth  $B'$ . A schematic overview of a SISO communication system is shown in Fig. 2.3.

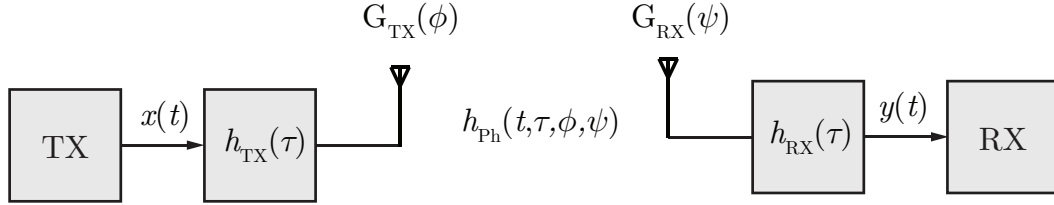


Figure 2.3: Example of a SISO communication system with the transmit filter  $h_{\text{TX}}(\tau)$  and the receive filter  $h_{\text{RX}}(\tau)$ .

The time variant CIR is obtained by

$$h(t, \tau) = h_{\text{TX}}(\tau) * h_{\text{Ph}}(t, \tau) * h_{\text{RX}}(\tau), \quad (2.6)$$

where  $*$  denotes the time-variant convolution,  $h_{\text{TX}}(\tau)$  and  $h_{\text{RX}}(\tau)$  denote the transmit and receiver filters and  $h_{\text{Ph}}(t, \tau)$  denotes the non-bandlimited physical communication channel. In the frequency domain this can be equivalently formulated as

$$g(t, f) = g_{\text{TX}}(f)g_{\text{Ph}}(t, f)g_{\text{RX}}(f) \quad (2.7)$$

where  $g_{\text{TX}}(f)$  and  $g_{\text{RX}}(f)$  denote the transmit and receive filter in the frequency domain and  $g_{\text{Ph}}(t, f)$  denotes the non-bandlimited CTF of the physical channel.

In a time-variant environment, not taking polarization into account, the CIR of the non band-limited physical propagation channel of a SISO system can be described by a double-directional channel model [29, 32–35]

$$h_{\text{Ph}}(\mathbf{r}_{\text{TX}}, \mathbf{r}_{\text{RX}}, t, \tau, \phi, \psi) = \sum_{p=0}^{P(t)-1} h_p(\mathbf{r}_{\text{TX}}(t), \mathbf{r}_{\text{RX}}(t), \tau(t), \phi(t), \psi(t)). \quad (2.8)$$

Here,  $\mathbf{r}_{\text{TX}}(t)$  and  $\mathbf{r}_{\text{RX}}(t)$  denote the time-variant positions of the transmitter and the receiver,  $P(t)$  denotes the time-variant number of propagation paths and the variables  $\tau_p(t)$ ,  $\phi_p(t)$  and  $\psi_p(t)$  denote the time-variant delay, the time-variant direction of departure (DOD) and the time-variant direction of arrival (DOA), of the  $p$ -th propagation path, respectively. For planar waves the contribution of the  $p$ -th MPC, can be modeled by [35]

$$h_p(\mathbf{r}_{\text{TX}}(t), \mathbf{r}_{\text{RX}}(t), \tau(t), \phi(t), \psi(t)) = \eta'_p(t)\delta(\tau - \tau_p(t))\delta(\phi - \phi_p(t))\delta(\psi - \psi_p(t)), \quad (2.9)$$

where  $\eta'_p(t)$  denotes the time-variant complex weighting factor of path  $p$ .

For brevity we will neglect the dependency on  $t$  of the MPC parameters in the following equations and will only point it out for specific cases. We reformulate (2.8) by

$$h_{\text{Ph}}(\mathbf{r}_{\text{TX}}, \mathbf{r}_{\text{RX}}, t, \tau, \phi, \psi) = \sum_{p=0}^{P-1} h_p(\mathbf{r}_{\text{TX}}, \mathbf{r}_{\text{RX}}, t, \tau, \phi, \psi), \quad (2.10)$$

where  $h_p(\mathbf{r}_{\text{TX}}, \mathbf{r}_{\text{RX}}, t, \tau, \phi, \psi) = h_p(\mathbf{r}_{\text{TX}}(t), \mathbf{r}_{\text{RX}}(t), \tau(t), \phi(t), \psi(t))$  denotes the time-variant CIR of the  $p$ -th path. We obtain  $h_{\text{Ph}}(t, \tau)$  from the double directional channel model in (2.10) by

$$h_{\text{Ph}}(t, \tau) = \int_{\phi} \int_{\psi} h_{\text{Ph}}(\mathbf{r}_{\text{TX}}, \mathbf{r}_{\text{RX}}, t, \tau, \phi, \psi) G_{\text{TX}}(\phi) G_{\text{RX}}(\psi) d\phi d\psi \quad (2.11)$$

where  $G_{\text{TX}}(\phi)$  and  $G_{\text{RX}}(\psi)$  represent the transmit and receive antenna patterns, respectively.

### 2.2.2 MIMO Channel Model

For MIMO communication systems the transmitter and the receiver are equipped with more than one antenna. Figure 2.4 shows a schematic presentation of a MIMO system. The MIMO channel has to be described for all pairs of transmit and receive antennas. For a system with  $m$  transmit and  $n$  receive antennas we obtain [35]

$$\mathbf{H}(t, \tau) = \begin{pmatrix} h_{11}(t, \tau) & h_{12}(t, \tau) & \dots & h_{1m}(t, \tau) \\ h_{21}(t, \tau) & h_{22}(t, \tau) & \dots & h_{2m}(t, \tau) \\ \vdots & \vdots & \ddots & \vdots \\ h_{n1}(t, \tau) & h_{n2}(t, \tau) & \dots & h_{nm}(t, \tau) \end{pmatrix} \in \mathbb{C}^{n \times m}, \quad (2.12)$$

where  $h_{ij}(t, \tau)$  denotes the time-variant CIR between the  $j$ -th transmit antenna and the  $i$ -th receive antenna defined according to (2.6). The channel matrix includes the effect of the transmit and receive filters and the antenna patterns of the respectively utilized antennas.

For the MIMO system the received signal vector  $\mathbf{y}(t) = [y_1(t), y_2(t), \dots, y_n(t)]^T \in \mathbb{C}^{n \times 1}$  is obtained by

$$\mathbf{y}(t) = \int_{\tau} \mathbf{H}(t, \tau) \mathbf{x}(t - \tau) d\tau, \quad (2.13)$$

with  $\mathbf{x}(t) = [x_1(t), x_2(t), \dots, x_m(t)]^T \in \mathbb{C}^{m \times 1}$ .

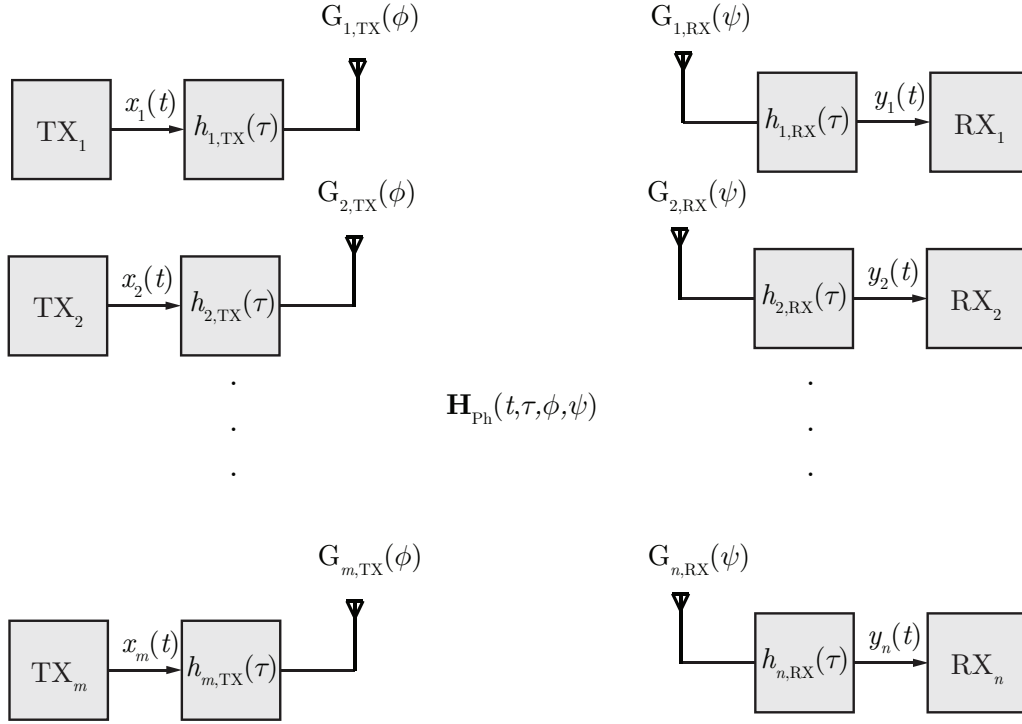


Figure 2.4: Example of a MIMO communication system with  $m$  transmit antennas and  $n$  receive antennas. Different transmit filters  $h_{j,\text{TX}}(\tau)$  and receive filters  $h_{i,\text{RX}}(\tau)$  are utilized.

## 2.3 Stochastic Description of the Wireless Channel

An alternative system theoretic description of communication channels are stochastic channel models, where the linear time-variant channel impulse response is treated as a random process [2]. Considering the time-variant CTF, the auto correlation function (ACF) [2, 28, 29, 31]

$$R_g(t, t', f, f') = \mathcal{E} \{g(t, f)g(t', f')^*\} \quad (2.14)$$

provides a fully statistical description, if  $g(t, f)$  is a 2D complex Gaussian random process with zero mean.

### 2.3.1 Wide-Sense-Stationary Uncorrelated-Scattering (WSSUS)

#### Wide-Sense-Stationary

If the ACF does not depend on the times  $t$  and  $t'$  separately, but on the time

difference  $\Delta t = t - t'$ , it is called wide-sense-stationary (WSS) [2], i.e.,

$$R_g(t, t', f, f') = R_g(t - t', f, f') = R_g(\Delta t, f, f'). \quad (2.15)$$

In other words, if the channel is WSS the statistic of the channel does not change over time. The WSS assumption also implies that the MPCs with different Doppler shifts are uncorrelated [2].

### Uncorrelated-Scattering

If the ACF does not depend on the absolute frequency but on the difference  $\Delta f = f - f'$ , it is called uncorrelated-scattering (US). In this case the ACF can be written by

$$R_g(t, t', f, f') = R_g(t, t', f - f') = R_g(t, t', \Delta f). \quad (2.16)$$

For US channels, MPCs with different delays are uncorrelated.

### Wide-Sense-Stationary Uncorrelated-Scattering

If both assumptions apply, i.e., WSS and US, the process is called wide-sense-stationary uncorrelated-scattering (WSSUS) and the ACF depends only on two variables

$$R_g(t, t', f, f') = R_g(t - t', f - f') = R_g(\Delta t, \Delta f). \quad (2.17)$$

Using the two dimensional Fourier transform we obtain the two dimensional scattering function  $C(\tau, \omega) \geq 0$  [29] by

$$C(\tau, \omega) = \int_{-\infty}^{\infty} \int_{-\infty}^{\infty} R_g(\Delta t, \Delta f) e^{-j2\pi(\omega\Delta t - \tau\Delta f)} d\Delta t d\Delta f, \quad (2.18)$$

which describes how the mean energy is distributed in the delay-Doppler domain. This description allows for an easier physical interpretation of the dispersion effect of the wireless communication channel.

### 2.3.2 Non-WSSUS

For practical communication channels, e.g., vehicular communication channels, the WSSUS assumption is only satisfied for a limited region in time and frequency. In this case the channel is characterized as a non-WSSUS channel. It can be described by the local scattering function (LSF) [29, 31, 36–39]

$$C(t, f; \tau, \omega) = \int_{-\infty}^{\infty} \int_{-\infty}^{\infty} R_g(t, f; \Delta t, \Delta f) e^{-j2\pi(\omega\Delta t - \tau\Delta f)} d\Delta t d\Delta f \quad (2.19)$$

with

$$R_g(t, f; \Delta t, \Delta f) = \mathcal{E} \{g(t, f + \Delta f)g^*(t - \Delta t, f)\}. \quad (2.20)$$

The LSF is associated with a locally defined stationarity region which quantifies the duration and bandwidth within which the communication channel can be approximated with good accuracy by a WSSUS channel [29]. The LSF describes the power of MPCs with delay  $\tau$  and Doppler shift  $\omega$  at time  $t$  and frequency  $f$  [37]. Due to the dependency on time and frequency the LSF can be used to describe non-stationarities of the wireless communication channel over time and frequency. We will use the assumption of local stationarity to emulate the wireless communication channel. The LSF will be utilized for characterizing and validating the emulated channel.

### 2.4 Channel Model Categorization

Channel models, that reflect the properties of the wireless propagation channel, are of utmost importance, for the design, test and validation of communication systems. Communication system designers need channel models that include the most important properties of the communication channel in order to select the best physical layer parameters such as, bandwidth, modulation and coding scheme, sub-carrier spacing, pilot placement, etc.. Choosing the wrong physical layer for given channel properties leads to reduced system performance. A particularly bad example is IEEE 802.11p. It was derived of the, for indoor environments designed, IEEE 802.11a, for wireless vehicular communication. Especially in NLOS conditions with high delay and Doppler spreads, IEEE 802.11p does not perform well due to its pilot structure [40]. It was shown in [41] that enhanced pilot patterns, specifically a postamble, allow for a better performance.

The test and validation of wireless communication systems in the field is cost intensive and difficult to reproduce. An example is the test of vehicular communication systems at road intersection or in highway scenarios. Due to a fluent change of traffic, the exact positions of the cars in the scenario can often not be reproduced. Another example is the optimization of base station positions for a certain area. Using a trial and error approach is costly and time intensive.

Numerical channel models allow to perform tests in a reproducible fashion in a laboratory environment or via numerical link level simulation. There exist many channel models, where a specific model usually serves one specific purpose [28]. They can be grouped into the following categories [2, 31, 35, 40, 42–46].

- **Deterministic channel models:** Deterministic channel models solve the Maxwell equations for a specific environment to obtain the CIR [2]. The model requires a detailed description of each object in the environment, which includes shape, position and electromagnetic (dielectric and conductivity) properties. The most accurate solution to the Maxwell equations are obtained by

solving their integral or differential form numerically. For the integral form the method of moments is utilized, while for the differential form the finite element method or the finite difference time domain method is used [2]. Approximated solutions to the Maxwell equation are obtained by ray launching or ray tracing (RT) methods [47–52], which apply the fundamental principles of reflection, diffraction and scattering. In ray launching [53] different rays are sent out from the TX into different directions. The ray launching algorithm follows the rays until they hit the RX or they become too weak to become significant [2]. In ray tracing the image method is utilized to determine the rays transmitted from the TX that reach the RX position. The higher the order of reflections, the higher the computational complexity. The CIR is obtained by a (large) sum of received rays. If the model considers moving objects, the non-stationary effects are inherently modeled. These methods can be highly accurate but require high computational complexity.

Ray launching and ray tracing methods are extremely useful methods if an accurate site specific description is available. Adapting to more general locations, however, is difficult. Ray tracing for vehicular environments was used by Maurer et. al [47, 48, 50] and for tunnel scenarios by Gan et al. [52].

- **Stochastic channel models:** Stochastic channel models are designed such, that the CIR fulfills given statistical properties in terms of first and second order moments [31, 54–56]. Molisch et al. [2, 43] distinguish between narrowband and wideband stochastic channel models. Narrowband stochastic channel models focus on the characterization of the fading statistics together with the Doppler spectrum. The channel is considered to be frequency flat for the utilized bandwidth. Wideband stochastic models such as the tap delay line (TDL) model are based on the WSSUS assumption (see also Section 2.3) [30] and capture statistical properties like the power delay profile and the Doppler spectral density. The taps are modeled, e.g., with Rayleigh or Rician fading with a Doppler spectral density that follows, e.g., a Clarke’s model [57]. Due to their simple approach TDL models have been adapted by different standardization bodies. The most well known standardized models are the COST 207 [58] model for the global system for mobile communications (GSM) and the ITU-R [59] model for the universal mobile telecommunications systems (UMTS).
- **Geometry-based stochastic channel models:** Geometry-based stochastic channel models (GSCMs) [33, 60] are a combination of deterministic and stochastic channel models. They allow for a good trade-off between complexity and accuracy. In a GSCM scatterers (diffuse or discrete) are placed randomly according to a certain distribution in a geometric environment of e.g. a high-

way or a road intersection. The CIR is obtained by (simplified) ray tracing methods. The higher the number of scatterers, the higher the computational complexity and the accuracy of the model. Different GSCMs have been proposed in [33, 60–69]. The GSCM has a number of benefits [60]: It can model non-WSSUS channels, it can model MIMO channel properties, it is possible to easily change the antenna influence by simply including a different antenna pattern, the environment can be easily changed and it is much faster than ray tracing, since only simplified single (or double) reflections need to be calculated.

An extensive overview of different (standardized) channel models can be found in literature, see e.g. [28, 35, 43]. In this thesis we consider geometry-based channel models.

### 3 Wireless Channel Emulation

Channel emulators are used to reproduce the effect of wireless communication channels in order to test wireless communication systems in a laboratory environment. The huge benefit is the reproducibility and repeatability of test results. At the present time most channel emulators are implemented in the digital domain with a powerful base band processing unit that convolves the down-converted and digitized radio frequency (RF) input signal with the sampled time-variant CIR (discussed in Section 3.2.1). A schematic representation is shown in Fig. 3.1. The analog RF input

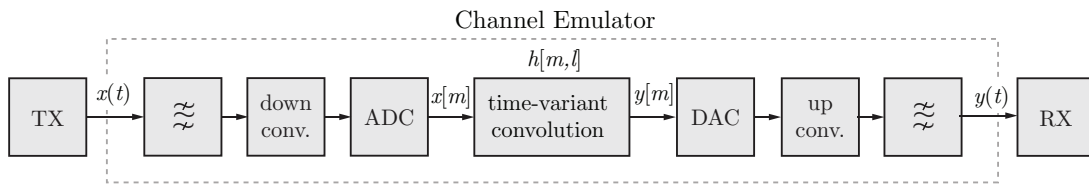


Figure 3.1: Schematic representation of a channel emulator implemented in the digital domain to test communication systems. The transmitted signal is convolved with the emulated time-variant channel impulse response.

signal  $x(t)$  is filtered and down-converted to base band and sampled by the analog-to-digital converter (ADC) to obtain the sampled input signal  $x[m]$ . The input signal is convolved with the (time-variant) CIR  $h[m, l]$  that is calculated according to the underlying utilized channel model. The convolution is typically implemented on a digital signal processor (DSP) or field programmable gate array (FPGA). Subsequently, the digital output signal  $y[m]$  is converted by the digital-to-analog converter (DAC) to the analog domain and up-converted to RF to obtain the analog output signal  $y(t)$ .

For specific applications the delay introduced by digital signal processing, which includes the ADC and DAC, RF up- and down-conversion, input- and output-filter, convolution, etc., is a critical performance factor. For radar target channel emulation, e.g., the signal processing delay limits the minimum distance of the emulated radar target. Hence, for small distances extremely fast ADCs and DACs or even analog emulation techniques, like simple delay chains, have to be used.

In this thesis we will focus on real-time channel emulation using a digital implementation targeting applications, where the processing delay of the emulator is of minor importance. Firstly, a review of state of the art channel emulator solutions is shown and their inability of emulating realistic communication channels with real valued path delays and Doppler shifts, where the path delays and Doppler shifts are updated in real-time is discussed. Our channel emulator will focus on geometry-based channel emulation that can circumvent this problem. We show how geometry-based channel emulation can be realized in real-time using a SDR platform based on the work of Kaltenberger et. al. [28]. Finally, we will validate the implemented channel emulator by channel sounding measurements with the RUSK Lund channel sounder.

## 3.1 State of the Art Channel Emulation

There are different approaches to channel emulation. Some channel emulators implement only simple path-loss models (e.g. Friis law), others use more advanced models like a TDL approach with stationary statistics. The most important parameters of a channel emulator is its frequency range, number of antennas, bandwidth and which channel models it can emulate. Channel emulators can be classified into commercially available channel emulators and SDR channel emulator solutions.

### 3.1.1 Commercially Available Channel Emulators

Commercially available channel emulator solutions are typically very expensive and produced for testing communication systems against a variety of standardized channel models. As of 2019, there are emulator solutions e.g. of Keysight [70], Spirent [71] and Anritsu [72] available, which we will discuss shortly.

#### 3.1.1.1 Keysight

The company PropSim was acquired by Anite in 2013, which itself was acquired by Keysight in 2015. Keysight offers a variety of channel emulator solutions. The latest model, the PropSim F64, allows to emulate  $64 \times 64$  bi-directional MIMO channels with bandwidths from 5 to 400 MHz. Carrier aggregation of up to 1.2 GHz is possible. The emulator supports MIMO over-the-air (OTA) testing and massive MIMO beam forming. Frequency ranges of sub-6 GHz and mmWave, probably with frequency extensions, are supported. Unfortunately, the number of supported paths per channel is not provided. A previous model, the Keysight F32, supports 48 paths per emulated channel with a maximum delay of 3 ms. Furthermore, the emulator supports channel models like the 3rd Generation Partnership Project (3GPP) TR138.901 [73],

TR36.873 [73], spatial channel model extended, IMT-Advanced [74], Winner [64], and TGn/ac/ax.

### 3.1.1.2 Spirent

The latest emulator solution of Spirent is the Vertex® which supports frequencies from 30 MHz to 6 GHz. Up to 32 communication channels with a bandwidth of 200 MHz are supported. The Vertex allows emulating SISO and MIMO channels and can be used for MIMO OTA, MIMO beam forming and massive MIMO testing. Similar to Keysight, a detailed manual is not available at this moment. A previous model, the VR5, supports 24 paths per channel with a maximum delay of 4 ms and a resolution in the delay domain of 0.1 ns.

### 3.1.1.3 Anritsu

The company Azimuth was acquired by Anritsu in 2017. Anritsu offers the Azimuth ACE-RNX channel emulator which allows to emulate 24 taps per channel with a bandwidth of 100 MHz. Different standard models like 3GPP/3GPP2 LTE/3G/2G are supported. The emulator allows for 8x4 bi-directional MIMO emulation.

## 3.1.2 Software Defined Radio Based Channel Emulators

Besides commercially available channel emulation solutions also SDR based channel emulators [62, 75–84] have been developed. While the channel emulator solution developed by National Instruments (NI) [75] utilizes a vector signal transceiver to emulate a  $2 \times 2$  MIMO channel that is based on a TDL model, Vlastaras et al. [76] implement a TDL with two active taps and equal power for stress testing IEEE 802.11p modems. Ghiaasi et al. [77] use a TDL in connection with a clustering algorithm [85, 86] to reduce the number of propagation paths that have to be simultaneously emulated. In [77] the maximum number of simultaneously active delay taps is ten. Blazek et al. [81] extend the emulator of [77] by utilizing a sum-of-sinusoid model in connection with a discrete-time Hilbert transform to obtain bathtub, respectively half-bathtub Doppler spectra [87] for the delay taps. In [82] the work of [77] was extended using a sparse fit to extract the most important channel coefficients for a TDL model of a road intersection scenario. The emulated channel is used for modem tests. The authors of [62] present a non-stationary wireless MIMO channel model. However, the authors only consider fractional path delays and stationarity region lengths of 9 to 20 ms where the velocity is assumed to be constant. The maximum number of emulated paths is thirty-two. The channel emulator shown by MKG systems [78] allows for a maximum number of twelve delay taps. The authors of [83, 84]

use a TDL for OTA testing. The emulator in [88] utilizes a TDL and assumes for simplicity constant delay of the taps for the generation of small scale fading effects.

### 3.1.3 Shortcomings of current Channel Emulator Solutions

Due to the underlying TDL model, the emulators described above share the main drawback that path delays can only be set in integer multiples of the sampling rate. However, real world, non-stationary communication scenarios are characterized by continuously changing real valued path delays and Doppler shifts. The testing of real-time control algorithms requires updating the position and speed of the TX and RX according to the laws of kinematics, and correspondingly, the wireless propagation characteristics in *real-time* with continuous variations in delay and Doppler. With this approach, real-time wireless data communication between the controller and the sensors, as well as between the controller and the actuators reflects the properties of a realistic environment and enables repeatable tests. Use cases are, e.g., (a) testing of connected autonomous vehicles, and (b) industrial production environments with mobile robots.

## 3.2 System Model

For channel emulation we consider a SISO communication system with omnidirectional antennas at TX and RX. As described in Section 2.2.1 the non-stationary, time-variant CTF [29, 32–34]

$$\begin{aligned}
 g(t, f) &= g_{\text{RX}}(f)g_{\text{Ph}}(t, f)g_{\text{TX}}(f) \\
 g(t, f) &= g_{\text{RX}}(f) \sum_{p=0}^{P-1} \eta'_p(t) e^{-j2\pi\tau_p(t)f} g_{\text{TX}}(f).
 \end{aligned} \tag{3.1}$$

is described by the superposition of  $P$  individual propagation paths with time-variant path delay  $\tau_p(t)$ . Each path is characterized by the complex time-variant weighting coefficient  $\eta'_p(t) = a_p(t)e^{j2\pi\phi_p}$  with amplitude  $a_p(t)$  and initial phase  $\phi_p$ . The initial phase is determined by the distance between transmitter and receiver. The different MPCs originate from LOS, static discrete (e.g. road signs), mobile discrete (other vehicles) and diffuse (vegetation, walls of houses) scatterers.

The non-stationary fading process (see Section 2.3.2) can be approximated as WSSUS for the stationary time  $T_{\text{stat}}$  and stationarity bandwidth  $B_{\text{stat}}$  [39, 89]. We assume that the path amplitudes are constant within such a stationarity region, i.e., without loss of generality,  $\eta'_p(t) \approx \eta'_p$  for  $t_0 \leq t_1 < t_0 + T_{\text{stat}}$ . Furthermore, the relative velocity between transmitter and receiver is assumed constant during this

interval (in Section 3.3 we will analyze the error if a linear acceleration is assumed within the stationarity region). Thus, the time-variant path delay is described by a linear model

$$\tau_p(t) = \tau_p(0) - \frac{v_p}{c_0}t, \quad (3.2)$$

where  $\tau_p(0)$  denotes the initial path delay,  $v_p$  denotes the relative velocity between transmitter and receiver per propagation path, which is determined by the geometry of the scenario (see e.g. [33, 60, 90, 91] for more information), and  $c_0$  denotes the speed of light. Defining the Doppler shift as

$$\omega_p = f_c \frac{v_p}{c_0}, \quad (3.3)$$

where  $f_c$  denotes the carrier frequency of the system, an equivalent notation of (3.2) can be found as

$$\tau_p(t) = \tau_p(0) - \frac{\omega_p}{f_c}t. \quad (3.4)$$

Inserting (3.4) in (3.1) we can rewrite (3.1) as

$$\begin{aligned} g(t, f) &= g_{\text{TX}}(f) \sum_{p=0}^{P-1} \eta'_p(t) e^{-j2\pi(f'+f_c)(\tau_p(0) - \frac{\omega_p}{f_c}t)} g_{\text{RX}}(f) \\ &= g_{\text{TX}}(f) \sum_{p=0}^{P-1} \eta'_p(t) e^{-j2\pi f' \tau_p(0)} e^{j2\pi f' \frac{\omega_p}{f_c}t} e^{-j2\pi f_c \tau_p(0)} e^{j2\pi \omega_p t} g_{\text{RX}}(f), \end{aligned} \quad (3.5)$$

where we consider the frequency  $f = f' + f_c$  as composition of the carrier frequency  $f_c$  and the frequency offset  $f' \in [-B/2, B/2]$  (see also [33, Sec. II-A]). Assuming that the system bandwidth is much smaller than the carrier frequency, i.e.,  $f' \ll f_c$ , which is true for most communication systems [29, Ch. 1], we obtain the approximate time-variant CTF as

$$g_{\text{Ph}}(t, f) = \sum_{p=0}^{P-1} \eta_p e^{j2\pi \omega_p t} e^{-j2\pi \tau_p(0) f'}, \quad (3.6)$$

where we neglected the term  $e^{j2\pi f' \frac{\omega_p}{f_c}t}$  and defined  $\eta_p = \eta'_p e^{-j2\pi \tau_p(0) f_c}$ .

### 3.2.1 Non-Stationary Fading Process as Concatenation of Stationarity Regions

Due to the band limiting filters at transmitter and receiver the actually non-band-limited physical CTF  $g_{\text{Ph}}(t, f)$  can also be considered as band-limited to the specified bandwidth  $B'$ . For an ideal filter  $g_{\text{Ph}}(t, f) = 0$  for  $|f| > B'$ , which allows to sample

and implement a digital representation of the CTF. Realistic filters, however, are not ideal, that means, the filter transfer function has a finite slope from passband to stopband. Hence, to allow for realistic input/output filters we oversample  $g_{\text{Ph}}(t, f)$  by a factor  $f_{\text{OSF}}$ , i.e.,  $B' = f_{\text{OSF}}B$ . We sample with  $T_C = 1/B'$  in time and  $F_s = B'/N$  in frequency, where  $N$  is the number of frequency bins. Considering the band-limiting filters  $g_{\text{TX}}(f)$  and  $g_{\text{RX}}(f)$  at the transmitter and receiver side, respectively, and using (3.6) we obtain the sampled non-stationary CTF as the concatenation of stationarity regions of length  $T_{\text{stat}}$ . Defining  $M = \lceil T_{\text{stat}}/T_C \rceil$  as the length of the stationarity region in samples, we obtain the concatenated CTF according to

$$\begin{aligned} g[m, q] &= g_{\text{TX}}(qF_s)g_{\text{RX}}(qF_s)g_{\text{Ph}}(((s-1)M + m')T_C, qF_s) \\ &= g_{\text{TX}}[q]g_{\text{RX}}[q] \sum_{p=0}^{P-1} \eta_{p,s} e^{j2\pi\nu_{p,s}m'} e^{-j2\pi\theta_{p,s}q}, \end{aligned} \quad (3.7)$$

where  $\eta_{p,s}$ ,  $\nu_{p,s} = \omega_{p,s}T_C$  and  $\theta_{p,s} = \tau_{p,s}(0)/(NT_C)$  denote the path weight, the normalized Doppler shift, and the normalized path delay of stationarity region  $s$  respectively. It holds that  $|\nu_{p,s}| < \frac{1}{2}$  and  $0 \leq \theta_{p,s} < 1$ . Discrete time is denoted by  $m = (s-1)M + m'$  with  $m' \in \{0, \dots, M-1\}$  and discrete frequency by  $q \in \{0, \dots, N-1\}$ .

The velocities, and correspondingly the Doppler shifts, are assumed to be constant during a stationarity region. A schematic representation of the stationarity assumption is shown in Fig. 3.2. It leads to a linear change of delay within a stationarity region as modelled in (3.4) and shown in Fig. 3.3.

To allow for a continuous phase transition between stationarity regions, we incorporate the final delay of path  $p$  in region  $s$  into the starting phase of the next stationarity region  $s+1$ . The delay at the end of the stationarity region is obtained by

$$\tau_{p,s}[M-1] = \tau_{p,s}[0] - \frac{\omega_{p,s}}{f_c}(M-1)T_C, \quad (3.8)$$

leading to a starting phase incorporated in  $\eta_{p,s+1} = \eta_p e^{-j2\pi\tau_{p,s}[M-1]f_c}$ . Correspondingly, the normalized path delay is defined as  $\theta_{p,s+1} = \tau_{p,s}[M-1]/NT_C$ .

To emulate the effects of a wireless propagation channel, the emulator convolves the input signal  $x[m]$  with the time-variant CIR  $h[m, l]$ , obtaining the output signal

$$y[m] = \sum_{l=0}^{L-1} h[m-l, l]x[m-l], \quad (3.9)$$

with  $l$  denoting the index in the delay domain and  $L$  the number of delay taps. Due to the bandlimiting effect of the input filter, the support of  $h[m, l]$  is actually

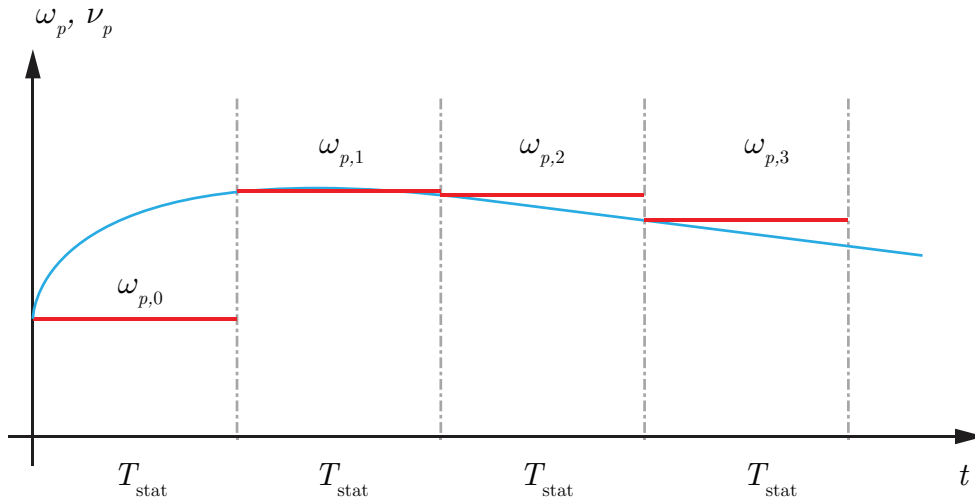


Figure 3.2: Piecewise constant Doppler shift approximation of the instantaneous Doppler shift  $\omega_p$  for different stationarity regions.

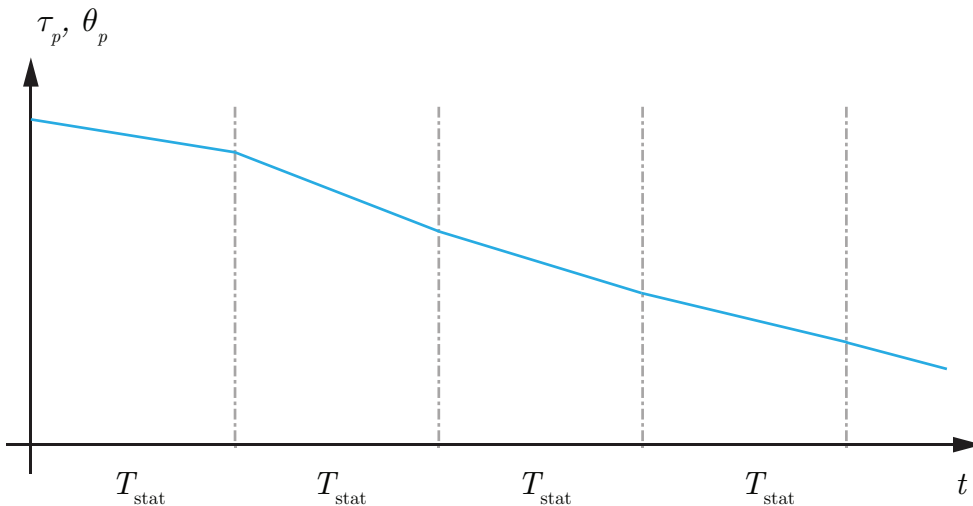


Figure 3.3: Linear change of delay within stationarity regions.

infinite [92]. However, the contributions for large  $l$  will be very small, so they can be neglected. For a causal implementation of the CIR we allow for pre- and post-cursor samples, i.e.  $L = L' + L_{\text{pre}} + L_{\text{post}}$ , with  $L' = \lceil \tau_{\text{max}}/T_C \rceil$  and  $\tau_{\text{max}}$  the maximum path delay of the CIR. The values of  $L_{\text{pre}}$  and  $L_{\text{post}}$  depend on the required dynamic range of the system.

The CIR is obtained from the inverse discrete Fourier transform (IDFT) of the

time-variant CTF  $g[m, q]$ . For a better dynamic range of the CIR we implement a windowing function  $f_{\text{win}}[q]$  (see Section 3.6.2) that reduces the side lobes of the sinc-Kernel due to the finite bandwidth  $B'$ ,

$$h[m, l] = \frac{1}{N} \sum_{q=0}^{N-1} f_{\text{win}}[q] g[m, q] e^{j2\pi l q / N}. \quad (3.10)$$

### 3.2.2 Channel Impulse Response Data Rate

For the time-variant convolution in (3.9), a new CIR has to be available every  $T_C = 1/B$ . The number of delay taps is proportional to  $\tau_{\text{max}}$  of the wireless propagation channel

$$L' = B\tau_{\text{max}}. \quad (3.11)$$

Hence, the resulting data rate of the CIR  $D_{\text{CIR}}$  increases quadratic with  $B$

$$D_{\text{CIR}} = 2BL'N_{\text{bit}} = 2B^2\tau_{\text{max}}N_{\text{bit}}, \quad (3.12)$$

where 2 originates from the real and imaginary part of the CIR and  $N_{\text{bit}}$  is the number of bits to represent the real and imaginary part, respectively. Table 3.1 shows an example of the data rate of a CIR with  $\tau_{\text{max}} = 1.6 \mu\text{s}$  for different bandwidths using 16 bits to represent real and imaginary part, respectively.

Table 3.1: Data rate of CIR versus communication system bandwidth.

Bandwidth $B$ [MHz]	1	10	100
Data Rate $D_{\text{CIR}}$ [GBit/s]	0.0512	5.12	512

The CIR is generated according to the considered channel model. Simplistic channel models allow a direct implementation in hardware, using, e.g., an FPGA or a DSP. More sophisticated models, like the GSCM, however, have higher computational complexity. An implementation of the model in hardware is either technically or economically infeasible or the channel model has to be implemented with a lower amount of detail. An alternative approach is to implement the channel model in software, e.g., in C, Matlab or Python, using a powerful processor to calculate the CIR in real-time and to stream it to a device that implements the convolution with the transmitted signal.

However, from the discussion above, it is obvious that, streaming the CIR between devices can quickly become a bottleneck and other ways for transmitting the CIR have to be investigated. Kaltenberger et al. [28, 92, 93] introduced a novel channel emulation method utilizing a low-complexity, reduced-rank subspace model for

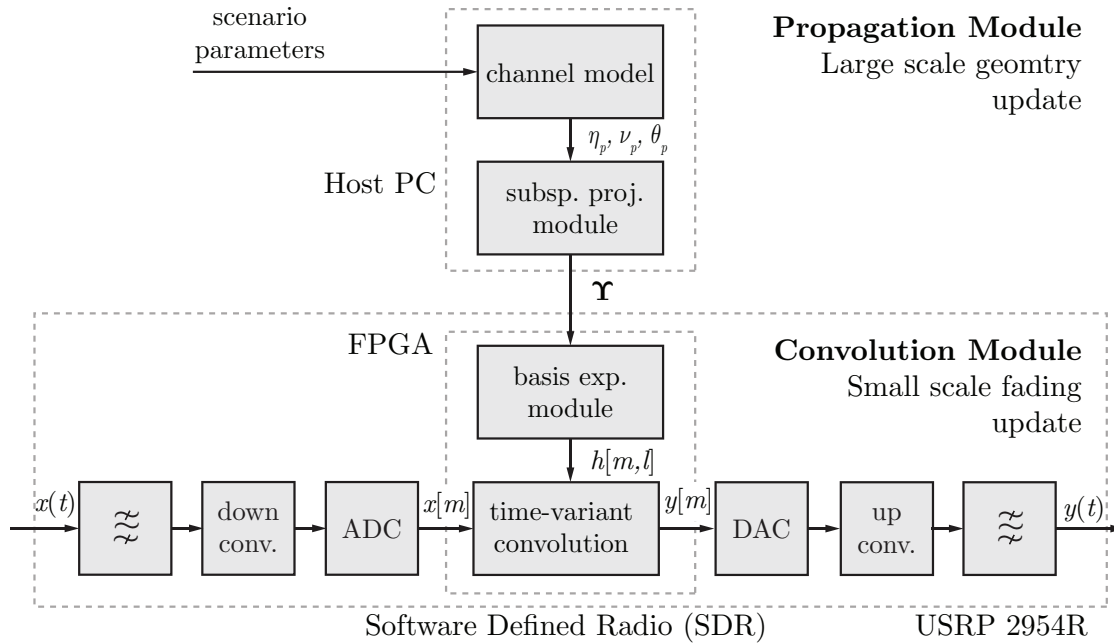


Figure 3.4: Geometry-based channel emulator structure

geometry-based channel emulation allowing for real-valued path delays and Doppler shifts. In the next Section we will show how to utilize this technique to obtain a real-time geometry-based channel emulator.

### 3.2.3 Geometry-Based Channel Emulation Architecture

Calculating (3.7) is of high computational complexity, since for each time instant and for each frequency index  $q$  a sum of  $P$  complex exponentials (CEs) has to be calculated. In this section we present a geometry-based channel emulator architecture, shown in Fig. 3.4, that enables a real-time implementation. The geometry-based channel emulator consists of a propagation module that is implemented on a general purpose multi-core personal computer (PC) and a convolution module that is implemented on an SDR equipped with an FPGA.

The propagation module is parametrized by the channel model, which periodically updates the geometry and calculates the propagation path parameters  $\eta_{p,s}$ ,  $\nu_{p,s}$  and  $\theta_{p,s}$  for each stationarity region  $s$ . To reduce the computational complexity of the sum of complex exponentials (SoCE) in (3.7), we exploit (i) the bandlimited properties of the fading process, and (ii) the limited accuracy of the ADC and DAC at the input and output. We approximate the SoCE in (3.7) by a reduced rank basis-

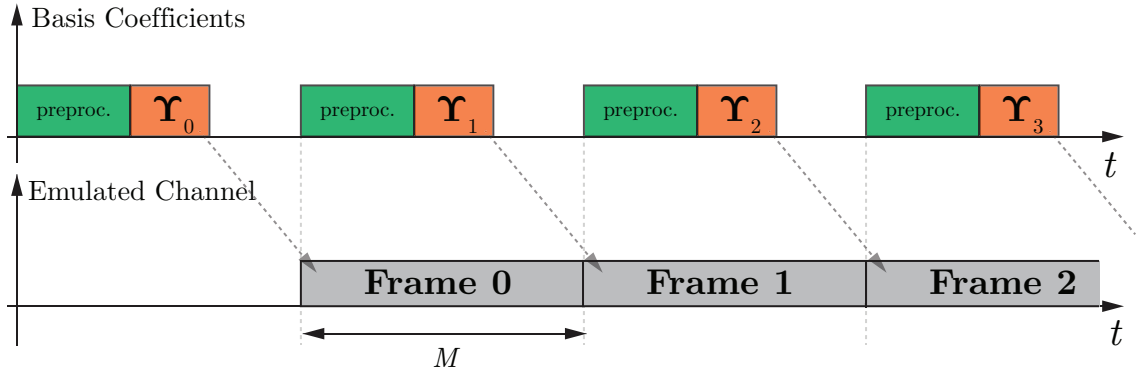


Figure 3.5: Frame structure of periodic transmission of basis coefficients for stationarity regions  $s$

expansion model (BEM) [23, 28, 92, 93]. The BEM uses DPS sequences [94] and the propagation parameters to calculate the basis coefficient matrix  $\Upsilon_s$  using a subspace projection. The basis coefficient matrix describes the evolution of the channel in the time and the frequency domain in a compressed form. A schematic representation of the transmission protocol of the basis coefficients  $\Upsilon_s$  from the PC to the SDR unit is shown in Fig. 3.5.

The SDR consists of a RF frontend in connection with an FPGA. In the RF frontend, the input signal is filtered and converted from passband to baseband by mixing with a local oscillator (LO). It is sampled by the ADC to obtain the digital baseband signal  $x[m]$ . In the basis-expansion module on the FPGA, we utilize  $\Upsilon_s$  and stored DPS sequences to obtain the time-variant CIR  $h[m, l]$ . In the time-variant convolution module, the input signal  $x[m]$  is convolved with  $h[m, l]$ , to obtain the output signal  $y[m]$ . Subsequently,  $y[m]$  is converted to an analog signal, by the DAC and shifted to the passband by mixing with the LO. The geometry-based channel emulator structure has two major advantages:

- The reconstruction complexity to obtain the time-variant CIR is *independent* of the number of propagation paths, which makes the model very suitable for an implementation on an FPGA.
- The streaming bandwidth between the general purpose PC and the SDR can be *significantly reduced*, since we transmit compressed CIRs in form of the basis coefficients  $\Upsilon_s$  instead of full CIRs.

We will explain the approximation steps of the model in the next subsections in more detail. The approximation error is analyzed in Section 3.3. For the discussion below we consider a single stationarity region  $s$ , without loss of generality.

### 3.2.4 Basis Expansion Model

Our reduced-rank BEM is based on two assumptions. Firstly, we assume that the channel is reconstructed block-wise for limited time-frequency snapshots, defined by the Cartesian index set

$$\mathcal{I} = I^t \times I^f = [0, \dots, M - 1] \times [0, \dots, N - 1]. \quad (3.13)$$

The size of the index set is smaller than, or equal to, the size of the local stationarity region. Secondly, we assume that  $\nu_p$  and  $\theta_p$  are limited to a band-limiting region that is defined by the Cartesian product

$$\mathcal{W} = W^t \times W^f = [-\nu_{D_{\max}}, \nu_{D_{\max}}] \times [0, \theta_{P_{\max}}]. \quad (3.14)$$

Here,  $\nu_{D_{\max}} = T_C f_c v_{\max} / c_0$  where  $v_{\max}$  denotes the maximum relative velocity between transmitter and receiver, and  $\theta_{P_{\max}} = \tau_{\max} / (NT_C)$  where  $\tau_{\max}$  is the maximum path delay of the channel. The maximum velocity and delay are determined by the considered scenario.

The index-limiting region  $\mathcal{I}$  in (3.13) and the band-limiting region  $\mathcal{W}$  in (3.14) are represented as Cartesian products. Hence, the subspace of the time-variant CTF for the duration of a stationarity region can be represented by two-dimensional DPS sequences [23, 32, 92, 94, 95]. DPS sequences are band-limited to a support  $W$  and simultaneously most energy concentrated in an interval  $I$ , which makes them ideally suited for reconstructing the wireless time-variant channel within a band- and index-limited region.

The two-dimensional reconstruction shown by Kaltenberger et al. [92, 95] has the disadvantage, that either the two-dimensional DPS sequences have to be stored on the FPGA, which requires a lot of memory, or the two-dimensional DPS sequences have to be calculated at run-time which is computationally expensive. Hence, for an implementation on the FPGA, we approximate (3.7) by a separate one-dimensional reconstruction approach shown in (3.15) (see next page), with the two-dimensional basis coefficients

$$\psi_{i,k} = \sum_{p=0}^{P-1} \eta_p \gamma_{i,p} \epsilon_{k,p}. \quad (3.16)$$

The DPS sequences  $u_j[l; W, I]$  are the solution to the eigenvalue problem [94, 96]

$$\sum_{l=0}^{M-1} C[l - m; W, I] u_j[l; W, I] = \lambda_j(W, I) u_j[m; W, I] \quad (3.17)$$

with  $m \in I$ ,

$$C[k; W, I] = \int_W e^{j2\pi k\nu} d\nu = \frac{1}{j2\pi k} (e^{j2\pi k\nu_2} - e^{j2\pi k\nu_1}), \quad (3.18)$$

$$\begin{aligned}
 g[m', q] &\approx \hat{g}[m', q] = \sum_{p=0}^{P-1} \eta_p \sum_{k=0}^{D^f-1} u_k[q; W^f, I^f] \epsilon_{k,p} \sum_{i=0}^{D^t-1} u_i[m'; W^t, I^t] \gamma_{i,p} \\
 &= \sum_{k=0}^{D^f-1} u_k[q; W^f, I^f] \sum_{i=0}^{D^t-1} u_i[m'; W^t, I^t] \underbrace{\sum_{p=0}^{P-1} \eta_p \gamma_{i,p} \epsilon_{k,p}}_{\psi_{i,k}} \\
 &= \sum_{i=0}^{D^t-1} \sum_{k=0}^{D^f-1} u_i[m'; W^t, I^t] u_k[q; W^f, I^f] \psi_{i,k} \tag{3.15}
 \end{aligned}$$

and  $W = [\nu_1, \nu_2]$ .

The variables  $\gamma_{i,p}$  and  $\epsilon_{k,p}$  denote the basis coefficients of path  $p$  in the time domain and the frequency domain, respectively. The dimensions  $D^t$  and  $D^f$  represent the number of utilized DPS sequences in the time and the frequency domain, respectively and determine the accuracy of the model. The time-variant transfer function can be efficiently compressed by a few subspace dimensions [94,97]. That is because the eigenvalues  $\lambda_j(W, I)$  of the vectorized DPS sequences  $\mathbf{u}_j(W, I)$  are clustered near 1 for  $D' \leq \lceil (\nu_2 - \nu_1)|I| \rceil$  and decay exponentially to 0 for  $D' > \lceil (\nu_2 - \nu_1)|I| \rceil$ , with  $|I|$  denoting the size of the set  $I$ . Specifically, the eigenvalues  $\lambda_i(W^t, I^t)$  of the vectorized DPS sequences  $\mathbf{u}_i(W^t, I^t)$  are clustered near 1 for  $D^{t'} \leq \lceil 2\nu_{\text{Dmax}}M \rceil$  and decay exponentially to 0 for  $D^{t'} > \lceil 2\nu_{\text{Dmax}}M \rceil$ . The same holds true for the eigenvalues  $\lambda_i(W^f, I^f)$ .

The computational complexity for the evaluation of the reduced-rank BEM in (3.15) is *independent* of the number of propagation paths. This makes it suitable for an implementation on the FPGA. The separate one-dimensional structure in the time and the frequency domain allows an efficient implementation on the FPGA with a reconstruction accuracy that is equivalent to the two-dimensional approach.

### 3.2.5 Approximate Basis Projection

The basis coefficients  $\gamma_{i,p}$  and  $\epsilon_{i,p}$  have to be calculated for each path by the projection of the CEs onto the DPS sequences. The projection of a single CE  $\mathbf{e}_p(\nu_p) = [e^{2\pi j\nu_p 0}, \dots, e^{2\pi j\nu_p(M-1)}]^T$  with normalized Doppler shift  $\nu_p$  onto the basis functions  $\mathbf{u}_d(W, I) = [u_d[0; W, I], u_d[1; W, I], \dots, u_d[M-1; W, I]]^T$  with band-limiting regions  $W$  and index set  $I$ ,

$$\gamma_d(\nu_p; W, I) = \sum_{m'=0}^{M-1} u_d[m'; W, I] e^{j2\pi\nu_p m'} \tag{3.19}$$

does not lead to a reduction in computational complexity, because each CE has to be evaluated for the projection and the numerical calculation complexity persists.

In [28, 92] it is shown that for the projection of a CE onto DPS sequences discrete prolate spheroidal wave functions (DPSWFs) can be utilized. There exists a close relation between DPSWFs and DPS sequences. The amplitude spectrum of a DPS sequence  $u_d[m'; W, I]$  index limited to a set  $I = [0, \dots, M - 1]$  and band-limited to  $W = [W_0 - W_{\max}, W_0 + W_{\max}]$ , with  $W_{\max}$  being the symmetric support and  $W_0 = \frac{\nu_2 - \nu_1}{2}$  the center point, is a scaled version of the associated wave function (cf. [94, equation (26)] [28, 92])

$$U_d(\nu; W, I) = \beta_d \sum_{m'=0}^{M-1} u_d[m'; W, I] e^{-j\pi(M-1-2m')\nu}, \quad (3.20)$$

where  $\beta_d = 1$  if  $d$  is even and  $\beta_d = j$  if  $d$  is odd. Comparing (3.19) with (3.20), one can see that the basis coefficients in (3.19) can be calculated by [28, 92]

$$\gamma_d(\nu_p; W, I) = \frac{1}{\beta_d} e^{j\pi(M-1)\nu_p} U_d(\nu_p; W, I). \quad (3.21)$$

For  $\nu_p \in W$  approximate DPSWFs can be defined according to [28, 92]

$$\tilde{U}_d(\nu_p; W, I) = \pm e^{2\pi j(M-1+m_p)W_0} \sqrt{\frac{\lambda_d M}{2W_{\max}}} u_d[m_p](W, I), \quad (3.22)$$

with  $\lambda_d(W, I)$  the corresponding eigenvalues and

$$m_p = \left\lfloor 1 + \left( \frac{\nu_p - W_0}{W_{\max}} \right) \frac{M}{2} \right\rfloor. \quad (3.23)$$

The sign in (3.22) is taken such that the normalization

$$\tilde{U}_d(W_0; W, I) \geq 0, \quad \left. \frac{d\tilde{U}_d(\nu_p; W, I)}{d\nu_p} \right|_{\nu_p=W_0} \geq 0 \quad (3.24)$$

$$d = 0, \dots, D - 1$$

holds. With (3.22)-(3.24) it can be shown that (3.21) can be approximately calculated by [28, 92]

$$\tilde{\gamma}_d(\nu_p; W, I) = \frac{1}{\beta_d} e^{j\pi(M-1)\nu_p} \tilde{U}_d(\nu_p; W, I). \quad (3.25)$$

We implement (3.25) using a table lookup with a table consisting of DPS sequences that can be pre-calculated and stored. We obtain the table index by inserting  $\nu_p$  and  $\theta_p$  into (3.23) and using the support  $W^t$  and  $W^f$  respectively.

Hence, the basis coefficients  $\gamma_{i,p}$  and  $\epsilon_{i,p}$  of each path can be approximately calculated by scaled and shifted approximate DPS wave functions with a complexity of  $\mathcal{O}(1)$ . Equation (3.25) allows for a strong computational complexity reduction compared to (3.19). This enables a real-time calculation of the approximate two dimensional basis coefficients  $\tilde{\psi}_{i,k}$  similar to (3.16).

The two-dimensional basis coefficients  $\tilde{\psi}_{i,k}$  represent an efficiently compressed version of the time-variant CTF in the time and the frequency domain for one stationarity region. They are utilized to reconstruct the CIR on the FPGA as shown in the next Section.

### 3.2.6 Time-Variant Channel Impulse Response

First we define the vector

$$\tilde{\mathbf{g}}[m'] = [\tilde{g}[m', 0], \dots, \tilde{g}[m', N - 1]]^T \in \mathbb{C}^{N \times 1}, \quad (3.26)$$

collecting all samples of the frequency response at time index  $m'$ , where  $\tilde{g}[m', q]$  is obtained from (3.15) using  $\tilde{\psi}_{i,k}$  instead of  $\psi_{i,k}$ . The time-variant CIR vector

$$\tilde{\mathbf{h}}[m'] = [\tilde{h}[m', 0], \dots, \tilde{h}[m', L - 1]]^T \in \mathbb{C}^{L \times 1} \quad (3.27)$$

is obtained by

$$\tilde{\mathbf{h}}[m'] = \mathbf{D}^H \mathbf{P} \mathbf{F} \tilde{\mathbf{g}}[m'], \quad (3.28)$$

where

$$\mathbf{F} = \text{diag}(\mathbf{f}_{\text{win}}) \in \mathbb{C}^{N \times N} \quad (3.29)$$

with  $\mathbf{f}_{\text{win}} = [f_{\text{win}}[0], f_{\text{win}}[1], \dots, f_{\text{win}}[N - 1]]^T \in \mathbb{C}^{N \times 1}$  being the windowing function. The permutation matrix  $\mathbf{P} \in \mathbb{R}^{N \times N}$  rearranges the elements of a vector  $\mathbf{x} = [x[0], x[1], \dots, x[N - 1]]^T \in \mathbb{C}^{N \times 1}$  according to

$$\mathbf{x}' = \mathbf{P} \mathbf{x} = [x[N/2], \dots, x[N - 1], x[0], \dots, x[N/2 - 1]]^T \quad (3.30)$$

to fit with the subsequent IDFT. Matrix  $\mathbf{D} \in \mathbb{C}^{N \times L}$  is a  $N \times L$  submatrix of the Fourier matrix  $[\mathbf{W}]_{i,j} = \frac{1}{\sqrt{N}} e^{-j2\pi ij/N} \in \mathbb{C}^{N \times N}$  and  $\forall i, j \in \{0, \dots, N - 1\}$ .

Defining

$$\mathbf{f}^t[m'] = [u_0[m'; W^t, I^t], \dots, u_{D^t-1}[m'; W^t, I^t]]^T \in \mathbb{R}^{D^t \times 1} \quad (3.31)$$

and the matrix of generalized basis coefficients

$$\tilde{\Psi} = \begin{pmatrix} \tilde{\psi}_{0,0} & \dots & \tilde{\psi}_{0,D^f-1} \\ \vdots & \ddots & \vdots \\ \tilde{\psi}_{D^t-1,0} & \dots & \tilde{\psi}_{D^t-1,D^f-1} \end{pmatrix} \in \mathbb{C}^{D^t \times D^f} \quad (3.32)$$

we can rewrite the subspace model in (3.15) in matrix-vector notation as

$$\tilde{\mathbf{g}}[m'] = \mathbf{V}\tilde{\Psi}^T\mathbf{f}^t[m'], \quad (3.33)$$

where  $\mathbf{V} = [\mathbf{u}_0(W^f, I^f), \mathbf{u}_1(W^f, I^f), \dots, \mathbf{u}_{D^f-1}(W^f, I^f)] \in \mathbb{C}^{N \times D^f}$  is the basis vector matrix in the frequency domain and  $\mathbf{u}_k(W^f, I^f) = [u_k[0; W^f, I^f], \dots, u_k[N-1; W^f, I^f]]^T$ . Inserting (3.33) in (3.28) we obtain

$$\tilde{\mathbf{h}}[m'] = \underbrace{\mathbf{D}^H\mathbf{P}\mathbf{F}\mathbf{V}}_{\mathbf{V}'}\tilde{\Psi}^T\mathbf{f}^t[m']. \quad (3.34)$$

Since the matrices  $\mathbf{D}$ ,  $\mathbf{P}$ ,  $\mathbf{F}$  and  $\mathbf{V}$  are constant they can be pre-calculated as  $\mathbf{V}' = \mathbf{D}^H\mathbf{P}\mathbf{F}\mathbf{V}$  with  $\mathbf{V}' \in \mathbb{C}^{L \times D^f}$  and stored.

The basis expansion coefficients  $\tilde{\Psi}$  do not change within one stationarity region. Thus we can pre-calculate the multiplication with the matrix  $\mathbf{V}'$

$$\Upsilon = \mathbf{V}'\tilde{\Psi}^T, \quad \Upsilon \in \mathbb{C}^{L \times D^t} \quad (3.35)$$

and reformulate (3.34) as

$$\tilde{\mathbf{h}}[m'] = \Upsilon\mathbf{f}^t[m']. \quad (3.36)$$

The basis vectors  $\mathbf{f}^t[m']$  are stored on the FPGA memory and are used for the reconstruction of the CIR.

### 3.3 Error Analysis

In this Section we analyze the error of the geometry-based channel emulator that is based on the reduced-rank BEM. Without loss of generality, we model the error within one stationarity region  $s$ . The error has to be smaller than the numerical precision, determined by the fixed-point precision of the analog/digital converter. It is defined by

$$E_{\text{th}} = 2^{-(N_b-1)}, \quad (3.37)$$

where  $N_b$  is the number of bits of the analog-to-digital converter. We analyze the following error sources:

- Basis expansion model bias
- Approximate basis projection error
- Error due to piecewise constant Doppler assumption
- Narrowband approximation error

### 3.3.1 Basis Expansion Model Bias

The reduced-rank BEM in (3.15) leads to an approximation bias that depends on the number of DPS sequences  $D^t$  and  $D^f$  that are utilized in the time and the frequency domain, respectively. Let's define the vectorized CTF  $\hat{\mathbf{g}}$  similar to (3.26).

$$\hat{\mathbf{g}} = [\hat{g}[0, 0], \hat{g}[0, 1], \dots, \hat{g}[M-1, N-1]]^T \in \mathbb{C}^{MN \times 1}. \quad (3.38)$$

For an uniform distribution of  $\nu_p$  and  $\theta_p$  on  $W^t$  and  $W^f$ , respectively, it can be shown [23, 92, 95] that

$$\text{bias}^2(D^t) = \frac{1}{2\nu_{D\max}M} \sum_{i=D^t}^{M-1} \lambda_i(W^t, I^t), \quad \text{and} \quad (3.39)$$

$$\text{bias}^2(D^f) = \frac{1}{\theta_{P\max}N} \sum_{k=D^f}^{N-1} \lambda_k(W^f, I^f), \quad (3.40)$$

where  $\lambda_i(W^t, I^t)$  and  $\lambda_k(W^f, I^f)$  are the sorted eigenvalues of the one dimensional DPS sequences in time and frequency direction respectively. In [23, 28, 92] the calculation of the optimum number of dimensions for the two-dimensional fading process described by (3.13) and (3.14) is shown.

### 3.3.2 Approximate Basis Projection Bias

The accuracy of the approximate projection (3.25) increases with reduced bandwidth  $W_{\max}$  and increased number of samples  $M$  [92]. This fact is utilized by defining a resolution factor  $r$  and using DPS sequences that are oversampled for the calculation in (3.25). Specifically, for positive integers  $r$  we define DPS sequences with

$$I_r = [0, \dots, rM-1], \quad (3.41)$$

and

$$W_r = [W_0 - \frac{W_{\max}}{r}, W_0 + \frac{W_{\max}}{r}]. \quad (3.42)$$

We use  $U_d(\frac{\nu_p}{r}; W_r, I_r)$  and  $u_d(\frac{\nu_p}{r}, W_r, I_r)$  for calculating the approximated coefficients.

The square bias of the approximate subspace projection is defined as [92]

$$\text{bias}_{\tilde{\mathbf{g}}^{D,r}}^2 = \mathbb{E} \left\{ \frac{1}{MN} \|\mathbf{g} - \tilde{\mathbf{g}}^{D,r}\|^2 \right\}, \quad (3.43)$$

with  $\tilde{\mathbf{g}}^{D,r}$  (cf. [23, 92]) being the approximate DPS subspace representation. No analytical results are available for the square bias, however, for the minimum square bias achievable it was numerically conjectured in [92] that

$$\text{bias}_{\min,r}^2 = \min_D \text{bias}_{\tilde{\mathbf{g}}^{D,r}}^2 \approx \left( \frac{2W_{\max}}{r} \right)^2, \quad (3.44)$$

with  $2W_{\max}$  representing the maximum two sided support. We use this as a guideline to calculate the resolution factors in time direction  $r^t$  and in frequency direction  $r^f$  separately. The resolution factors have to be chosen such that the bias is smaller than  $E_{\text{th}}^2$ . We refer the reader to [23, 92, 93] for additional information on the resolution factor. For the parameters in Table 3.2 and  $E_{\text{th}}^2$  from Table 3.3 we obtain  $r^t = 4$  and  $r^f = 4096$ .

### 3.3.3 Error Analysis of the Piecewise Constant Doppler Assumption

We investigate the error of the CTF due to the piecewise constant velocity (and Doppler shift) assumption within one stationarity region. For the analysis we consider the comparison with a scenario with constant acceleration  $a$ , which causes a linear changing velocity (Doppler shift). We model the error of a single propagation path with zero path delay. The linear changing velocity is modelled by

$$v_p[m'; a] = v_0 + am'T_C, \quad (3.45)$$

with the relative velocity  $v_0$  between TX and RX. Thus,

$$\begin{aligned} \nu_p[m'; \Delta\omega_p(a, f_c)] &= \frac{v_p[m'; a]}{c_0} f_c T_C \\ &= \frac{(v_0 + am'T_C)}{c_0} f_c T_C \\ &= \underbrace{\frac{v_0}{c_0} f_c T_C}_{\nu_p} + \underbrace{\frac{a}{c_0} f_c T_C^2 m'}_{\Delta\omega_p(a, f_c)}, \end{aligned} \quad (3.46)$$

where  $\Delta\omega_p(a, f_c)$  denotes the Doppler shift change of propagation path  $p$ . With a slight misuse of notion we obtain for the CTF

$$g[m'; \Delta\omega_p] = e^{j2\pi(\nu_p + \Delta\omega_p T_C^2 m')m'} = e^{j2\pi\nu_p m'} e^{j2\pi\Delta\omega_p T_C^2 m'^2}. \quad (3.47)$$

The mean square error (MSE) is calculated by

$$\begin{aligned} e_{\text{FD}}^2(\Delta\omega_p) &= \frac{1}{M} \sum_{m'=0}^{M-1} |g[m'; 0] - g[m'; \Delta\omega_p]|^2 \\ &= \frac{1}{M} \sum_{m'=0}^{M-1} |e^{j2\pi\nu_p m'} (1 - e^{j2\pi\Delta\omega_p T_C^2 m'^2})|^2 \\ &= \frac{1}{M} \sum_{m'=0}^{M-1} |(1 - e^{j2\pi\Delta\omega_p T_C^2 m'^2})|^2. \end{aligned} \quad (3.48)$$

The implementation of the approximated geometry-based channel emulator requires  $e_{\text{FD}}^2(\Delta\omega_p) < E_{\text{th}}^2$ . An example evaluation of the error with the parameters of Table 3.2 is shown in Fig. 3.6.

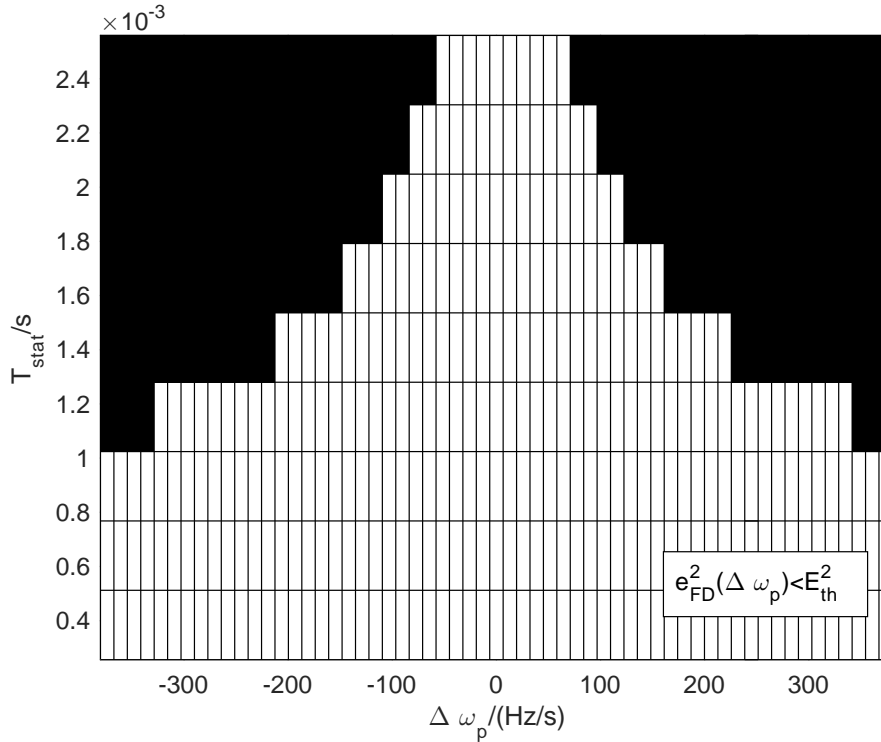


Figure 3.6: Indicator function  $e_{\text{FD}}^2(\Delta\omega_p) < E_{\text{th}}^2$  for piecewise constant Doppler shift vs. Doppler shift change and stationarity region length  $T_{\text{stat}}$ . The white region shows the area where the condition is satisfied.

We consider a maximum acceleration of  $\pm 20 \text{ m/s}^2$ , which leads to  $\Delta\omega_p \in \{-380.3 \text{ Hz/s}, \dots, 380.3 \text{ Hz/s}\}$ . We evaluate the stationarity region lengths  $T_{\text{stat}} \in \{256 \mu\text{s}, 512 \mu\text{s}, \dots, 2.56 \text{ ms}\}$ . We consider  $E_{\text{th}}^2 = -60 \text{ dB}$  for the error threshold (cf. Table 3.3).

The white region in Fig. 3.6 represents the area where  $e_{\text{FD}}^2(\Delta\omega_p) < E_{\text{th}}^2$ . We observe that there is a trade-off between  $\Delta\omega_p$  and  $T_{\text{stat}}$ . Considering a fixed error threshold a large  $\Delta\omega_p$  requires small  $T_{\text{stat}}$ , and vice versa. Please note that  $\Delta\omega_p$  depends on the carrier frequency  $f_c$  and on the acceleration  $a$  (cf. (3.46)). Hence, considering  $\Delta\omega_p$  fixed, to meet a fixed error threshold, an increase of the center frequency requires the reduction of the maximum acceleration. The maximum length of the stationarity region is ultimately limited by the complexity and storage of the used FPGA and the required accuracy of the channel model. We choose  $T_{\text{stat}} = 256 \mu\text{s}$  such that  $e_{\text{FD}}^2(\Delta\nu_P(a)) < E_{\text{th}}^2$  for the example implementation with  $E_{\text{th}}^2$  defined in Table 3.3.

The parameters of Table 3.2 are utilized for numerical evaluation and to calculate the DPS sequences as described in Section 3.2.4 (cf. (3.13) and (3.14)). We select the velocity  $v_{\max} = 400$  km/h (111 m/s) in Table 3.2 such that a large variety of scenarios can be emulated, i.e., also highway scenarios with high relative velocities. All scenarios with a velocity smaller than  $v_{\max}$  can be emulated by this setup.

Table 3.2: Channel parameters

Parameter	Value
$f_c$	5.7 GHz
$\tau_{\max}$	1.6 $\mu$ s
$v_{\max}$	400 km/h (111.1 m/s)
$B$	10 MHz
$f_{\text{OSF}}$	2
$T_C$	50 ns
$\omega_{\text{pmax}}$	2.11 kHz
$T_{\text{stat}}$	256 $\mu$ s
$a$	$-20 \dots 20$ m/s <sup>2</sup>
$N$	128
$M$	5120

Table 3.3: Emulation Parameters

Parameter	Value
$L_{\text{pre}}, L_{\text{post}}$	4
$E_{\text{th}}^2$	-60 dB
$D^{\text{t}}$	6
$D^{\text{f}}$	47
$r_t$	4
$r_f$	4096

### 3.3.4 Narrow Band Approximation Error

In this Section we investigate the error caused by neglecting  $e^{j2\pi\frac{\omega_p}{f_c}tf'}$  in the CTF in (3.5). We sample (3.5) with  $T_C = 1/B'$  in time direction and  $F_s = B'/N$  in frequency direction and use the definition of  $\eta_p$  in (3.6). Using the definition of  $g[m, q]$  in (3.7),

considering one stationarity region and neglecting the band-limiting filter  $g_{\text{TX}}[q]$  and  $g_{\text{RX}}[q]$  we obtain

$$g'[m', q] = g[m', q] e^{j2\pi \frac{\omega_p}{f_c} \frac{m' T_C q}{N T_C}} \quad (3.49)$$

$$= g[m', q] e^{j2\pi \frac{\omega_p}{f_c} \frac{m' q}{N}}. \quad (3.50)$$

We define the normalized error per time and frequency index

$$\begin{aligned} e_{\text{NB}}^2(\omega_p; m', q) &= |g[m', q] - g'[m', q]|^2 / |g[m', q]|^2 \\ &= \left| g[m', q] \left( 1 - e^{j2\pi \frac{\omega_p}{f_c} \frac{m' q}{N}} \right) \right|^2 / |g[m', q]|^2 \\ &= \left| \left( 1 - e^{j2\pi \frac{\omega_p}{f_c} \frac{m' q}{N}} \right) \right|^2. \end{aligned} \quad (3.51)$$

An exemplary representation of the error  $e_{\text{NB}}^2(\omega_p; m', q)$  using the parameters of Table 3.2 is shown in Fig. 3.7. We observe that the error grows with time and frequency index and increasing Doppler shift. For Doppler shifts small compared to the carrier frequency and small stationarity regions the error can essentially be neglected. For the emulation of larger Doppler shifts, the error may leads to a small phase discontinuity at the stationarity region boundaries.

For the design of the geometry-based channel emulator we choose the parameters such that

$$e_{\text{FD}}^2(\Delta\omega_p) + e_{\text{NB}}^2 + \text{bias}^2(D^t) + \text{bias}^2(D^f) < E_{\text{th}}^2. \quad (3.52)$$

## 3.4 Data Rate and Complexity Analysis

### 3.4.1 Data Rate Analysis for PC-SDR Link

The compression of the CIR in terms of basis expansion coefficients leads to an effective bandwidth reduction for the communication link between PC and SDR. Streaming the full CIR  $h[m, l]$  at each time instant  $m$  requires

$$R_{\text{full}} = \frac{2LN_{\text{bit1}}}{T_C} \text{ bits/s}, \quad (3.53)$$

while streaming the compressed CIR using  $\Upsilon_s$  requires

$$R_{\text{comp}} = \frac{2LD^t N_{\text{bit2}}}{T_{\text{stat}}} \text{ bits/s}. \quad (3.54)$$

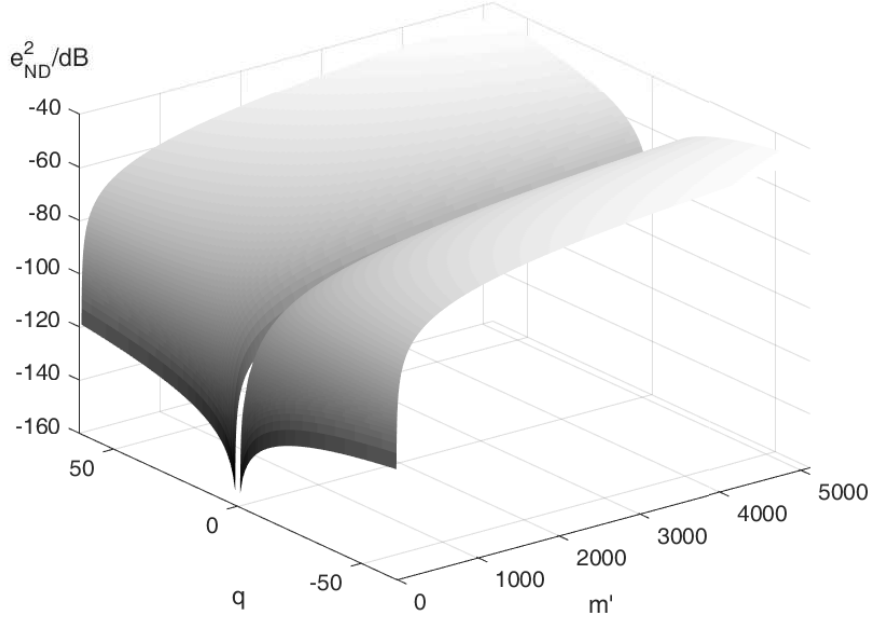


Figure 3.7: Exemplary narrowband approximation error vs. time and frequency index for  $\omega_{p\max} = 2.11$  kHz,  $T_{\text{stat}} = 256$   $\mu$ s,  $f_c = 5.7$  GHz and  $T_C = 50$  ns (cf. Table 3.2).

$N_{\text{bit1}}$  and  $N_{\text{bit2}}$  correspond to the used fixed-point precision for streaming  $h[m, l]$  and  $[\mathbf{Y}_s]_{k,l}$  to the SDR unit, respectively. Comparing the two data rates we obtain the data rate reduction factor

$$r_{\text{red}} = \frac{R_{\text{full}}}{R_{\text{comp}}} = \frac{T_{\text{stat}} N_{\text{bit1}}}{D^t T_C N_{\text{bit2}}}. \quad (3.55)$$

Since  $T_C \ll T_{\text{stat}}$  we have  $r_{\text{red}} \gg 1$ , i.e. we obtain a significant data reduction. The overall bandwidth reduction depends on  $T_{\text{stat}}$  since  $D^t$  is ultimately determined by the time-bandwidth product  $\lceil 2\omega_{p\max} T_{\text{stat}} \rceil$  and the required accuracy (see (3.39)). For a typical scenario with the parameters shown in Table 3.2 and Table 3.3, we obtain  $D^t = 6$ . With  $N_{\text{bit1}} = 16$  and  $N_{\text{bit2}} = 32$   $r_{\text{red}} \approx 427$ , i.e., we obtain a bandwidth reduction by a factor of 427 for the PC-SDR link.

### 3.4.2 Complexity Reduction Analysis

Calculating the SoCE in (3.7) requires  $\mathcal{O}(PMN)$  operations per stationarity region. The utilization of the BEM with the approximate subspace projection enables an efficient implementation of the geometry-based channel emulator with reduced

computational complexity. The calculation of the basis coefficients on the host computer requires only a table look-up and a scaling of  $P$  propagation graphs, i.e., it can be calculated in  $\mathcal{O}(P)$  operations. The computational complexity on the FPGA is constant and *independent* from the number of propagation paths and requires  $\mathcal{O}(D^t LM)$  operations. Since  $D^t \ll M$  and  $L \ll N$  the computational complexity of the approximate BEM is significantly smaller than the SoCE. With the parameters of Table 3.2 with  $L = 40$  and  $P = 500$  the complexity reduction amounts to

$$C_{\text{red}} = \frac{PNM}{P + D^t LM} \approx 267. \quad (3.56)$$

## 3.5 Hardware Implementation Aspects

### 3.5.1 Software Defined Radio

A SDR is a radio system that consists of hardware and software. A RF frontend in connection with a digital DSP or FPGA, whose functionality can be programmed in software, allows for a highly flexible application of SDRs in different fields. A typical example is the rapid prototyping of test systems, such as, the implementation of TX and RX of a communication system, channel sounders to measure the effects of the wireless communication channel on the transmitted signal as well as massive MIMO test systems. For the implementation of code and for programming the FPGA the NI software Labview Communications 2.0 was utilized.

In this thesis the NI universal software radio peripheral (USRP) 2954R [98] has been used as SDR. It is equipped with a Xilinx Kintex 7 K7410T as FPGA, has a frequency range of 10 MHz to 6 GHz and supports a bandwidth of up to 160 MHz. The up-and down-conversion from RF to baseband and vice versa is performed by UBX-160 daughter boards.

### 3.5.2 Channel Impulse Response Reconstruction on FPGA

To implement the reconstruction of the CIR shown in (3.36) on an FPGA, different approaches are possible. The matrix-vector multiplication can be implemented in a parallel fashion, where  $\tilde{\mathbf{h}}[m']$  is calculated at each sample point  $m'$  instantaneously. To do so, each row of  $\Upsilon$  is multiplied with  $\mathbf{f}^t[m']$  and summed up in parallel. Hence,  $D_t L$  multiplications and additions have to be implemented in parallel.

If the resources on the FPGA are limited, an alternative solution, that uses less resources, is to serialize the multiplication of (3.36). In this case only a part of the multiplication is implemented in parallel, but executed with higher frequency. If  $\frac{L}{a}$  row multiplications are implemented in parallel, where  $a$  is divider of  $L$ , the

multiplication has to be executed  $a$  times faster compared to the full parallel implementation to obtain one sample of  $\hat{\mathbf{h}}[m']$ . Obviously, there is a limit on parallel-serial implementation in terms of maximum specified execution frequency of the FPGA.

### 3.5.3 Local Oscillator Leakage

The USRP 2954R uses direct up/down-conversion to transform from/to baseband to/from RF baseband. Due to I/Q impairments in the conversion stage, LO leakage occurs, which results in an additional component in the intended signal. In the signal that is down-converted from RF to baseband, LO leakage leads to an additional component at 0 Hz (DC component). In the signal that is up-converted from baseband to RF, LO leakage leads to an additional component at the LO center frequency. Two techniques can be applied to omit LO leakage in the emulated signal:

- The first option is to apply I/Q impairment correction. This can be done digitally on the FPGA of the USRP, where the amplitude and the phase of the I and Q part can be changed separately.
- A second possibility is to artificially introduce digital heterodyne down/up-conversion and to filter the introduced LO leakage term. For digital heterodyne down-conversion, the RF signal is converted to an intermediate frequency which is within the bandwidth of the USRP. A band-limiting filter eliminates all LO leakage components outside the intended bandwidth of operation.

In this thesis both techniques were utilized. To correct the I/Q impairments, the emulator was firstly used in a feedthrough mode, where the transmit signal is simply fed through the SDR without an emulated CIR. The LO leakage was measured with a vector network analyzer (VNA) and the I/Q impairments were digitally corrected in such a way that the LO leakage was minimized. This can be done manually or automatically. In this thesis a manual approach was chosen. For digital heterodyne reception we choose an intermediate frequency (IF) frequency of 40 MHz.

## 3.6 Measurement and Validation Setup

In this Section we describe the measurement procedure and the metrics that we use for the validation of our geometry-based channel emulator. The measurement setup is shown in Fig. 3.8. The RUSK Lund channel sounder provides the *emulated* CIR measurements. The TX and RX of the channel sounder are connected via appropriate attenuators to the channel emulator.

We analyze the accuracy of our channel emulator by comparing the *time-variant* statistics of the emulated CIR with the simulated CIR [23, 24]. For this comparison we use the time-variant power delay profile (PDP) and the time-variant Doppler spectral density (DSD), which are obtained as marginals of the LSF [36, 37, 39, 99–101] (see Section 3.6.3). Please note that there is no synchronization between the measurement start of the channel sounder and the emulation start. The synchronization is performed manually in post processing.

#### 3.6.1 Numerical Simulation

We implement a floating point simulation of (3.7) in MATLAB. On the host computer the channel model is updated periodically for each stationarity region  $s$  to provide  $\eta_{p,s}$ ,  $\theta_{p,s}$  and  $\nu_{p,s}$ . We obtain the simulated CIR using (3.10). For a fair comparison we limit the simulated CIR to the first  $L$  taps.

#### 3.6.2 Emulation Parameters

For emulation, we use the channel parameters shown in Table 3.2 and the emulation parameters shown in Table 3.3. The update rate of the coefficients is  $1/T_{\text{stat}} \approx 3.907$  kHz. We set  $L_{\text{pre}} = L_{\text{post}} = 4$ . We use a Hann window as windowing function  $f_{\text{win}}$  (cf. (3.10)). We implement the model for an error of  $E_{\text{th}} \leq -60$  dB. Using (3.39) and (3.40) we obtain  $D^t = 6$  and  $D^f = 47$ . For an approximate subspace projection error smaller than  $E_{\text{th}}$  we set the resolution factor in time-direction  $r^t = 4$  and in the frequency direction to  $r^f = 4096$ . The overall system delay  $\tau_{\text{sys}} \approx 5.22$   $\mu\text{s}$  was measured and includes the delay introduced by the ADC and DAC, fractional decimation and first-input first-output (FIFO) register.

#### 3.6.3 Measurement Description

The RUSK channel sounder periodically samples the time-variant frequency response  $g(t, f)$  of a channel to obtain the discrete time-variant frequency response  $g[\chi, \xi] = g(\chi t_s, \xi f_s)$ . The discrete time index  $\chi \in \{0, \dots, X - 1\}$  is sampled with  $t_s$ , with  $X$  being the total number of snapshots. The discrete frequency index is denoted by  $\xi \in \{0, \dots, \Xi - 1\}$  with  $\Xi$  the number of frequency bins. The frequency resolution is defined by  $f_s = B_M/\Xi$ .

For the measurement, the length of the sounding sequence is set to  $T = 12.8$   $\mu\text{s}$ , which corresponds to the maximum measurable excess delay. The snapshot repetition rate is set to  $t_s = 102.4$   $\mu\text{s}$ , which results in a maximum resolvable Doppler shift  $\nu_{\text{smax}} = 1/(2t_s) = 4.883$  kHz. We record  $X = 10^5$  snapshots for the measurement,

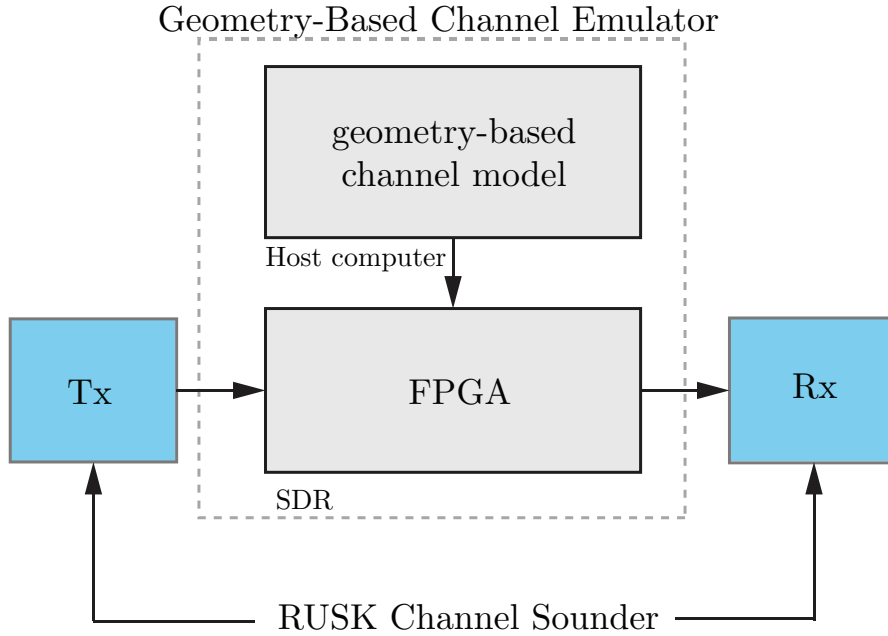


Figure 3.8: Measurement setup for the validation.

which is equal to a measurement time of  $T_{\text{meas}} = 10.24$  s. To be able to manually synchronize the channel sounder measurement with the geometry-based channel emulator, we emulate 8 s, although the emulation time is in general unlimited. We set the measurement bandwidth of the channel sounder to  $B_M = 100$  MHz. The bandwidth is separated in  $\Xi = 1281$  frequency bins which results in  $f_s = B_M/\Xi = 78.06$  kHz.

### 3.6.3.1 Local Scattering Function

To analyze the accuracy of the geometry-based channel emulator we compare the statistics of the CIRs using the LSF [36, 37, 39, 99–101]. The LSF assumes that the fading process is locally stationary within a region of  $M'$  samples in time and  $N'$  samples in frequency. We estimate the LSF for consecutive stationary regions in time indexed by  $s'$ . We use a multi-taper based estimator in order to obtain multiple independent spectral estimates from the same measurement [99, 102]. Since we emulate a small bandwidth, we assume only one stationarity region in frequency.

The estimate of the LSF is defined by [24, 39, 89, 101, 103]

$$\hat{\mathcal{C}}[s'; n, p] = \frac{1}{JK} \sum_{w=0}^{JK-1} |\mathcal{H}^{(G_w)}[s'; n, p]|^2. \quad (3.57)$$

We denote by  $n \in \{0, \dots, N' - 1\}$  the delay index and by  $p \in \{-M'/2, \dots, M'/2 - 1\}$  the Doppler index, respectively. The index of each stationarity region in time is denoted by  $s' \in \{0, \dots, \lfloor X/M' - 1 \rfloor\}$  and corresponds to the center of the stationarity regions. The windowed frequency response

$$\begin{aligned} \mathcal{H}^{(G_w)}[s'; n, p] &= \sum_{m''=-M'/2}^{M'/2-1} \sum_{q'=-N'/2}^{N'/2-1} g[m'' - s', q'] \\ &\cdot G_w[m'', q'] e^{-j2\pi(pm'' - nq')}, \end{aligned} \quad (3.58)$$

where the tapers  $G_w[m'', q'] = u_i[m''; W^{t'}, I^{t'}] u_j[q'; W^{f'}, I^{f'}]$  are two-dimensional DPS sequences [39, 94]. Here  $w = (i - 1)I + j$ ,  $i \in \{1, \dots, I\}$ ,  $j \in \{1, \dots, J\}$ , and  $W^{t'} = [-I/M', I/M']$ ,  $I^{t'} = M'$  and  $W^{f'} = [-J/N', J/N']$  and  $I^{f'} = N'$ . The number of tapers in the time and frequency domain is set to  $I = 3$  and  $J = 3$ , respectively [39, 101].

The delay and Doppler shift resolutions are given by  $\tau_s = 1/(N'f_s)$  and  $\omega_s = 1/(M't_s)$ . Please note that for an accurate implementation of the geometry-based channel emulator the stationarity region length has to be chosen to be small enough to meet the required error threshold (cf. Section 3.3). For the computation of the LSF, however, we choose the stationarity region to be larger, to obtain a higher Doppler resolution. We set  $M' = 400$ , which corresponds to a stationarity region length of  $T'_{\text{stat}} \approx 41$  ms in the time domain or equivalently  $\omega_s \approx 24.4$  Hz. Furthermore, we set  $N' = 128$ , corresponding to an evaluation bandwidth of  $B_{\text{eval}} \approx 10$  MHz in frequency domain or equivalently  $\tau_s \approx 100$  ns.

The PDP and DSD are calculated as marginals of the LSF over the Doppler or delay domain, respectively [39, 89, 103], i.e.,

$$\hat{\mathcal{P}}_\tau[s'; n] = E_p \left\{ \hat{\mathcal{C}}[s'; n, p] \right\} = \frac{1}{M'} \sum_{p=-M'/2}^{M'/2-1} \hat{\mathcal{C}}[s'; n, p], \quad (3.59)$$

$$\hat{\mathcal{P}}_\nu[s'; p] = E_n \left\{ \hat{\mathcal{C}}[s'; n, p] \right\} = \frac{1}{N'} \sum_{n=0}^{N'-1} \hat{\mathcal{C}}[s'; n, p]. \quad (3.60)$$

We calculate the simulated CIR with the snapshot rate of the channel sounder as described above. We obtain the CTF of the simulated CIR by means of a Fourier transform. We use (3.57) to calculate the LSF and (3.59) and (3.60) to calculate the PDP and DSD, respectively.

### 3.6.3.2 Emulation Error

We define the mean error between the normalized PDPs of simulation and emulation by

$$e_{\tau}[s'] = \frac{1}{N'} \sum_{n=0}^{N'-1} \|\hat{\mathcal{P}}_{\tau}^{\text{SIM},N}[s';n] - \hat{\mathcal{P}}_{\tau}^{\text{EM},N}[s';n]\|, \quad (3.61)$$

and the error between the normalized DSDs by

$$e_{\nu}[s'] = \frac{1}{M'} \sum_{p=-M'/2}^{M'/2-1} \|\hat{\mathcal{P}}_{\nu}^{\text{SIM},N}[s';p] - \hat{\mathcal{P}}_{\nu}^{\text{EM},N}[s';p]\|. \quad (3.62)$$

The normalized PDP  $\hat{\mathcal{P}}_{\tau}^{\text{SIM},N}[s';n]$  is obtained by  $\hat{\mathcal{P}}_{\tau}^{\text{SIM},N}[s';n] = \hat{\mathcal{P}}_{\tau}^{\text{SIM}}[s';n] / \max_{s',n}(\hat{\mathcal{P}}_{\tau}^{\text{SIM}}[s';n])$ . We apply the same normalization to the other PDP and to the DSDs. For the calculation of the error we manually synchronize the simulation and the emulation.

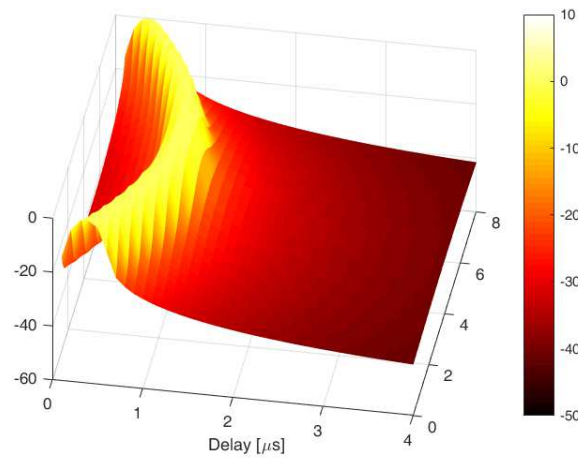
## 3.7 Measurement Results

We validate our geometry-based channel emulator with two different scenarios: (a) the emulation of a single path with continuously changing path delay, and (b) a GSCM of a road intersection. We compare the measured CIR of the geometry-based channel emulator with its numerical simulation by means of the time-variant PDP and DSD, see (3.61) and (3.62). Finally, the backward compatibility of the geometry-based channel emulator is shown by the emulation of European Telecommunications Standards Institute (ETSI) channel models.

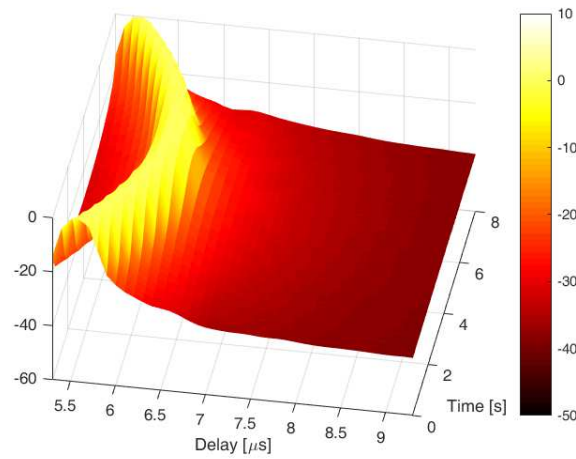
### 3.7.1 One-Path Channel Model

First, we validate the fundamental capability of our geometry-based channel emulator to emulate continuously changing path delays. We emulate a single propagation path with a Doppler shift that changes from  $-2$  kHz to  $2$  kHz. This leads to a continuously changing path delay that increases and decreases, according to the current Doppler shift. In Fig. 3.9, we show from top to bottom (a) the normalized PDP from the simulated CIR, (b) the normalized PDP from the emulated CIR, and (c) the error between the normalized PDPs. We show the same plots for the DSDs in Fig. 3.10.

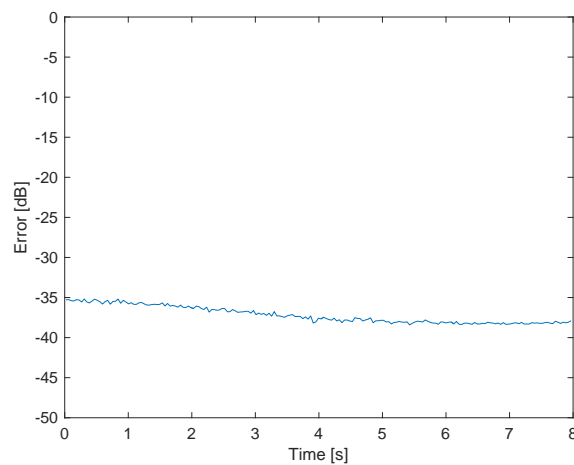
The results show a mean error of  $\approx -40$  dB between the DSDs and  $\approx -35$  dB between the PDPs. We obtain an error above the intended error threshold of  $-60$  dB due to additive measurement noise during the measurement, shown, e.g., in the



(a) Numerical simulation

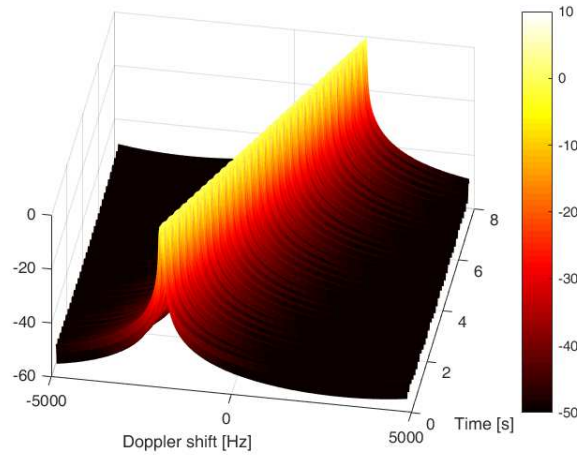


(b) Measured geometry-based channel emulator

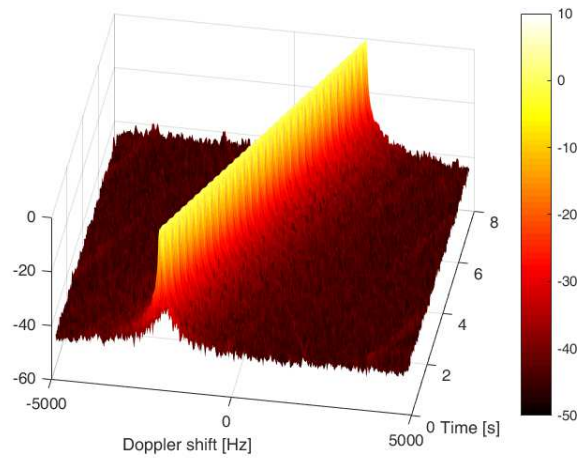


(c) PDP Error  $e_{\tau} [s']$

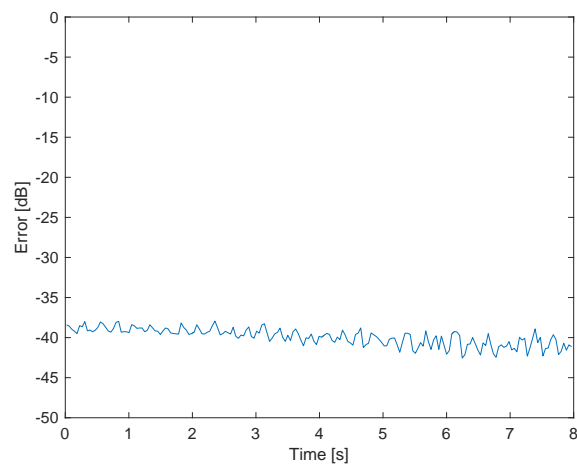
Figure 3.9: Comparison of the normalized PDPs for one propagation path with changing Doppler shift from  $-2$  kHz to  $2$  kHz.



(a) Numerical simulation



(b) Measured geometry-based channel emulator



(c) DSD Error  $e_\nu$  [s']

Figure 3.10: Comparison of the normalized DSDs for one propagation path with changing Doppler shift from  $-2$  kHz to  $2$  kHz.

DSD of the geometry-based channel emulator measurement in Fig. 3.10(b). With  $M' = 400$  and  $N' = 128$  we obtain a  $10 \log_{10}(400/128) \approx 5$  dB smaller mean error of the DSDs compared to the mean error of the PDPs, which is reflected in the measurement results. The small change of the mean error over time is due to imperfect synchronization in post processing.

#### 3.7.2 Geometry-Based Stochastic Channel Model

We show the capability of our geometry-based channel emulator to emulate realistic propagation scenarios, by the emulation of a GSCM of a road intersection scenario in *real-time*. The selected intersection with the trajectories of the TX and the RX is shown in Fig. 3.11. Empirical channel measurement data of the intersection was obtained by channel measurements performed in the city of Lund, Sweden in 2009 [39, 104].

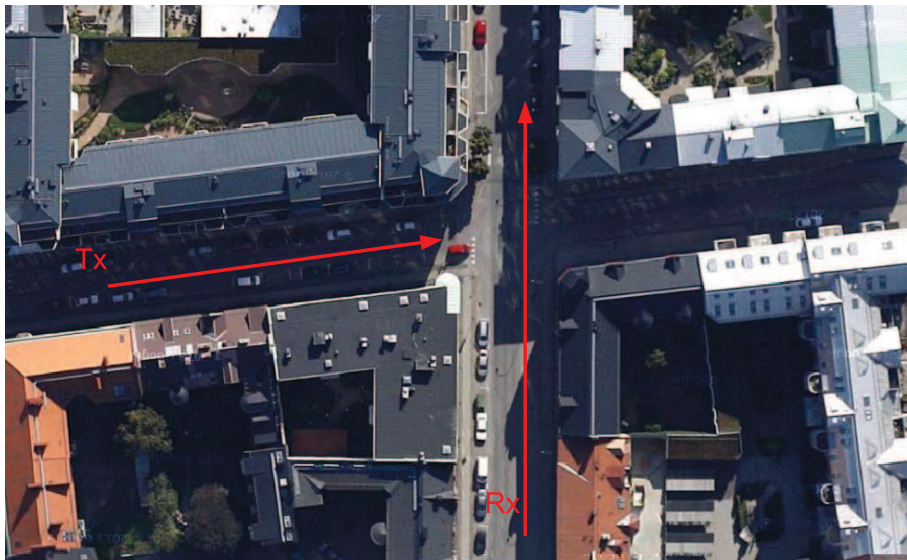


Figure 3.11: Top view of the investigated intersection (N55°42'38", E13°11'14") in the city of Lund with the trajectories of TX and RX respectively [3]

In [3] a GSCM for this intersection crossing scenario is developed. The model comprises up to 617 active propagation paths, each path having a time-variant Doppler shift, delay and attenuation. We determine the number of active paths by a visibility check between TX and RX. The GSCM includes randomly placed scatterers that are subject to a statistical distribution [60]. The geometry and one random realization of the point scatterer distribution are shown in Fig. 3.12. In [3] the delay-spread and path-loss versus distance is compared with the measurement

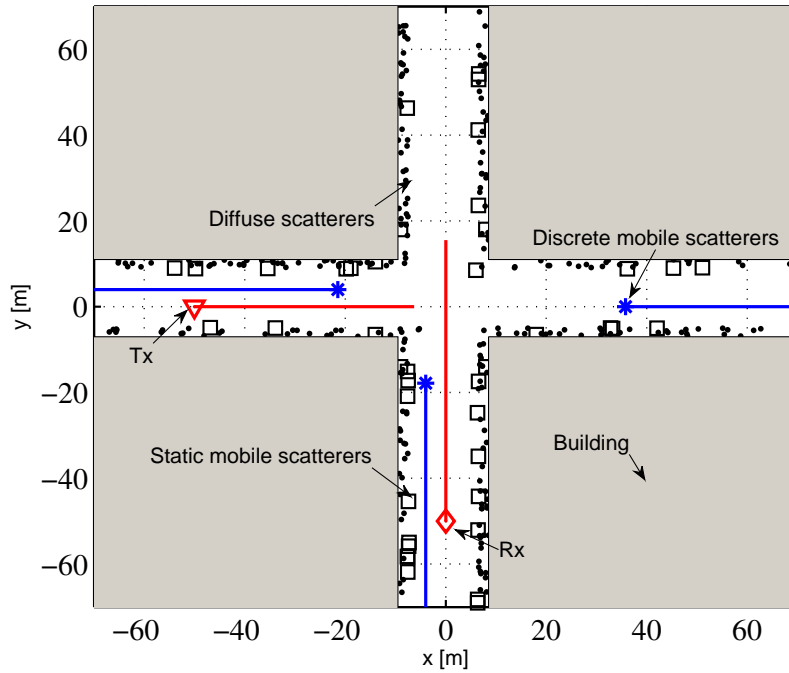


Figure 3.12: Scatterer distribution of the channel model for a road intersection [3]

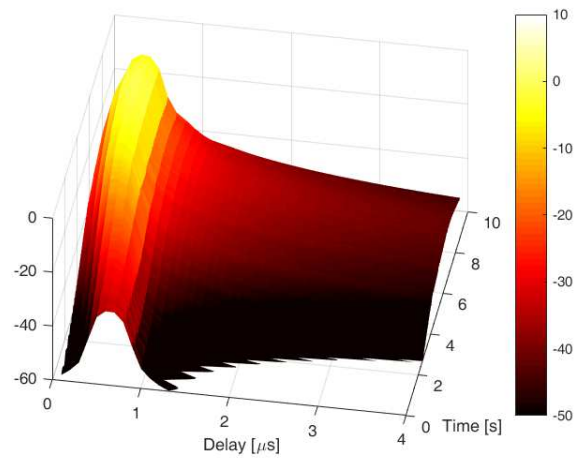
data and a good match is demonstrated. We added a diffraction model for the corners of the buildings to further improve the NLOS to LOS transition [105]<sup>1</sup>.

In Fig. 3.13, we show from top to bottom the normalized PDP of (a) the numerical geometry-based channel emulator simulation of the GSCM, (b) the measured CIR of the geometry-based channel emulator, and (c) the road intersection measurement. In Fig. 3.14, we show the same comparison for the DSD.

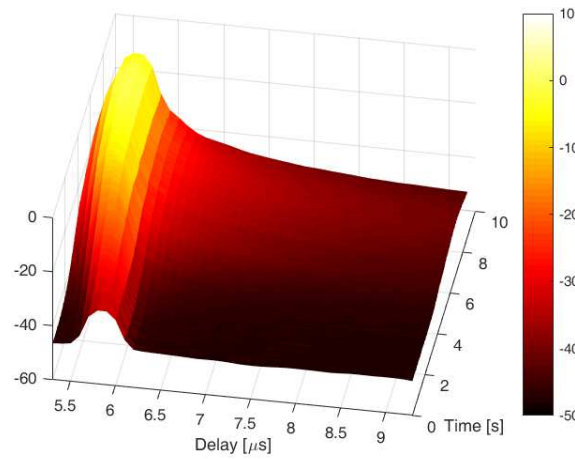
The mean error between the normalized PDPs and DSDs of emulation and numerical simulation are shown in Fig. 3.15. The mean error shows a good match between the numerical simulation and the measurement of the geometry-based channel emulator. The error above the intended threshold of  $-60$  dB is due to measurement noise (see Section 3.7.1).

We analyze the non-stationary fading process of the GSCM using statistical quantities, i.e., the time-variant root mean square (RMS) delay spread and the time-variant RMS Doppler spread. The RMS spreads are calculated according to [39].

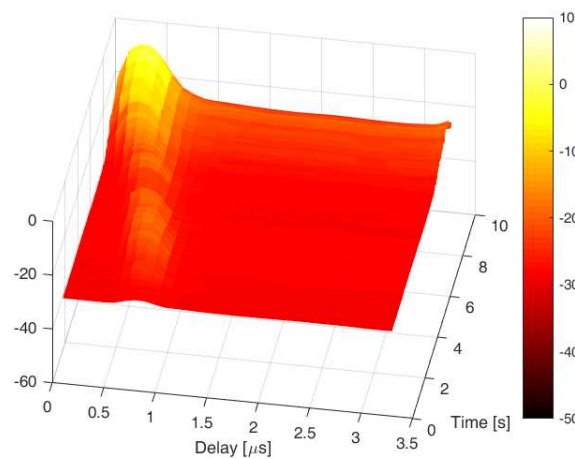
<sup>1</sup>It is based on the assumption that diffraction can take place at a street corner when LOS is unavailable. The attenuation of the diffraction path is calculated by the free space path loss expression and a fictitious distance, which is given by Berg's recursive expression [106]. The detailed calculation of the fictitious distance can be found in [105].



(a) Numerical GSCM simulation

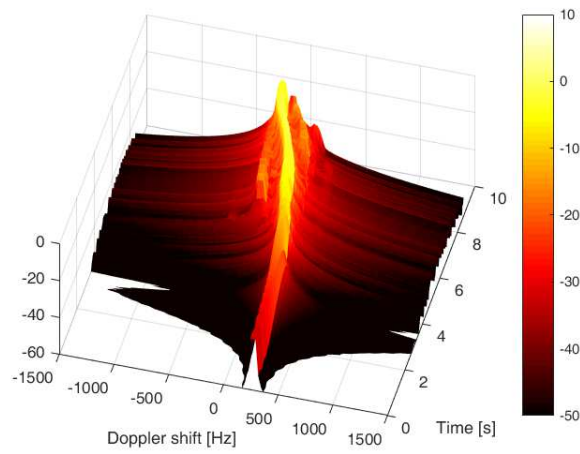


(b) GSCM emulated with geometry-based channel emulator

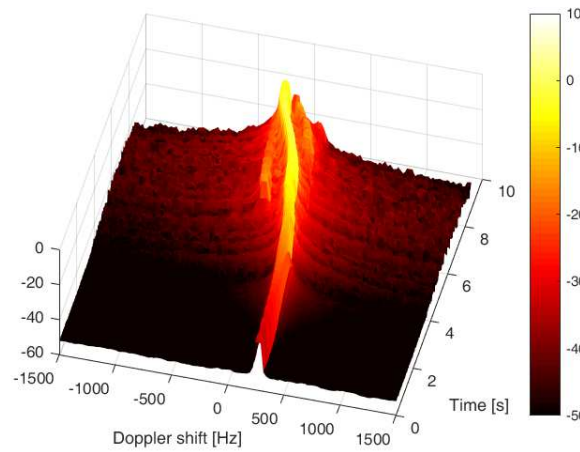


(c) Road intersection measurement

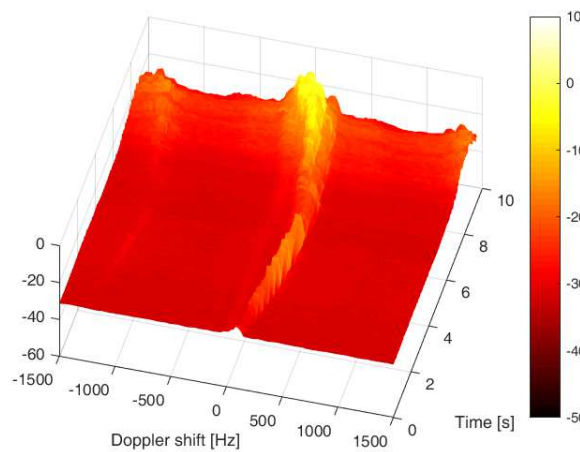
Figure 3.13: Comparison of the normalized PDPs for the road intersection scenario.



(a) Numerical GSCM simulation



(b) GSCM emulated with geometry-based channel emulator



(c) Road intersection measurement

Figure 3.14: Comparison of the normalized DSDs for the road intersection scenario.

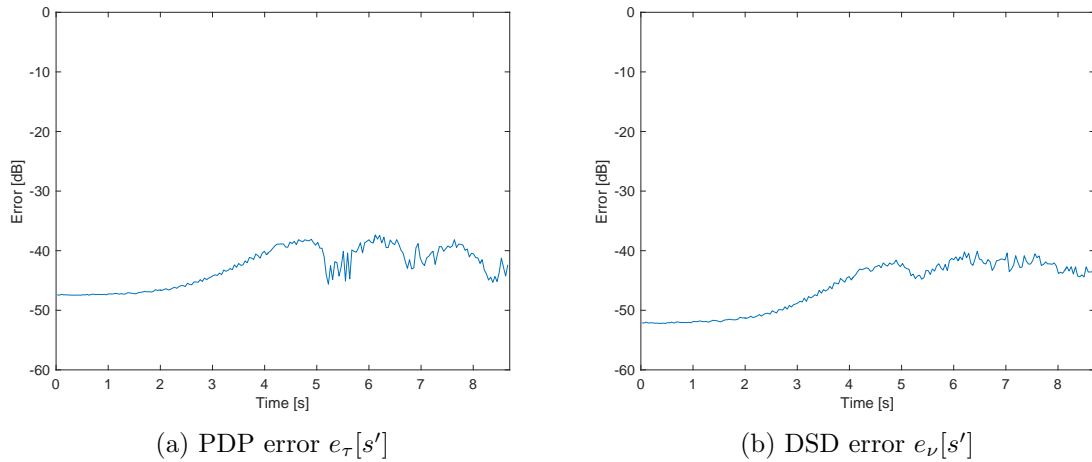


Figure 3.15: Comparison of PDP and DSD error for a road intersection scenario.

We apply a noise-power threshold to the emulated results to eliminate noise components that could be mistaken as MPCs. The noise-power threshold is chosen 5 dB above the noise floor. The sensitivity-threshold is chosen 30 dB from the highest peak (cf. [39, 107]). For the evaluation of the intersection measurements the high Doppler components are excluded.<sup>2</sup>

In Fig. 3.16, the gray region represents the 99 % quantiles of (a) the time-variant RMS delay spread and (b) the time-variant RMS Doppler spread, obtained from 100 random realizations of the GSCM scatterer placement. We plot the same second order statistics for the simulation of the GSCM (Simulation), the emulation of the GSCM (Emulation) and the road intersection measurement (Measurement). From Fig. 3.16 we observe that the RMS delay and RMS Doppler spread curves of numerical simulation and emulation match closely, in fact they lay on top of each other. For the GSCM a random realization of the scatterer placement is utilized. The road intersection measurement corresponds to another scatterer placement. Hence, the RMS delay and RMS Doppler spread of simulation and emulation differ from the RMS delay and the RMS Doppler spread of the measurement. However, the measured RMS delay and RMS Doppler spread are well within the gray region, showing that our GSCM parameterization can model the road intersection scenario. Further

<sup>2</sup>In our channel measurement data of the road intersection shown in Fig. 3.14(c), there are Doppler components visible at  $\pm 1500$  Hz starting from second nine onwards. We attribute the components to interference and did not include them in our GSCM model. The reason for this is, that the car during the measurement was traveling at max. 60 km/h (16.7 m/s). The visible Doppler components would be caused by a velocity of 79 m/s, which is not realistic, even if multiple reflections were considered. Hence, we are sure that these components are caused by interference.

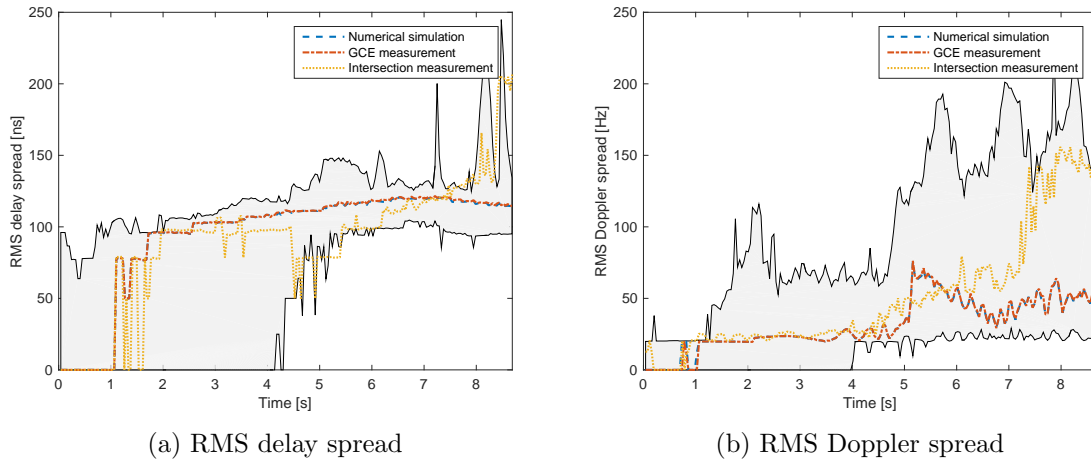
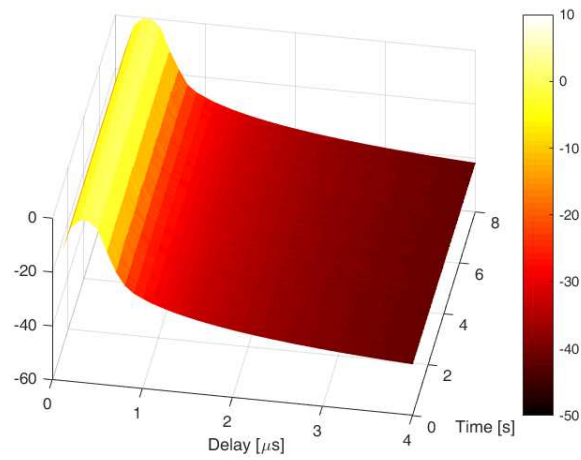


Figure 3.16: Comparison of the second order statistics of the road intersection scenario.

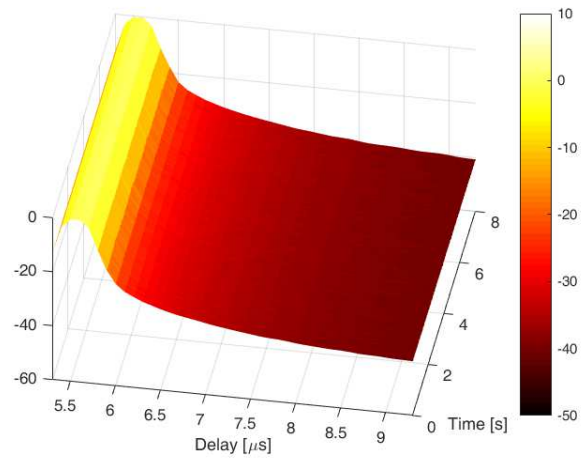
statistical evaluations of the measured RMS delay and RMS Doppler spreads in other scenarios can be found in [39]. Our geometry-based channel emulator measurement results demonstrate the capability to emulate a large number of propagation paths with continuously changing path delays and Doppler shifts that are determined by the environment geometry. Hence, we showed that the geometry-based channel emulator is able to emulate non-stationary wireless communication channels.

### 3.7.3 ETSI TDL Channel Models

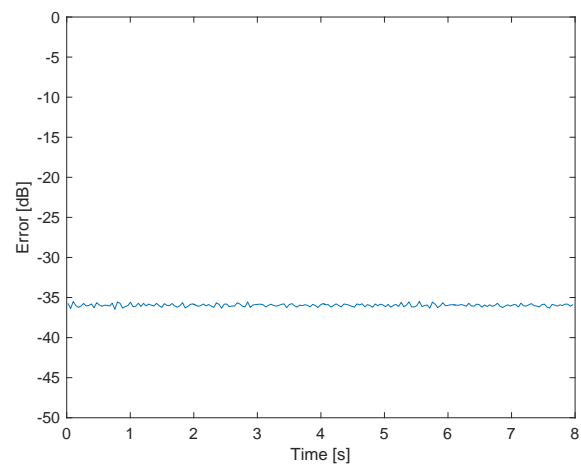
To demonstrate the backward compatibility of the geometry-based channel emulator to emulate TDL models, we emulate the ETSI channel models for testing vehicular communication systems [81, 87]. The models are TDL based and consider channel statistics that do not change over time. The DSD of the delay taps is modeled as a half-bathtub spectrum or as a full-bathtub spectrum, depending on the scenario considered. There exist five scenarios, each defining different path delays and Doppler spectra for the corresponding paths. We emulated and measured all scenarios. We only show the rural LOS scenario, the other scenarios are equivalent. We implement the positive (negative) half bathtub spectrum by summing 40 propagation paths for each delay tap and adjusting the impinging angle of the paths to the right (left) hemisphere corresponding to positive (negative) Doppler shifts. The impinging angles are randomly distributed on the respective hemisphere. The normalized PDPs and DSDs, and the error are shown in Fig. 3.17 and Fig. 3.18, respectively. Also here we see a close match between simulation and emulation.



(a) Numerical Simulation

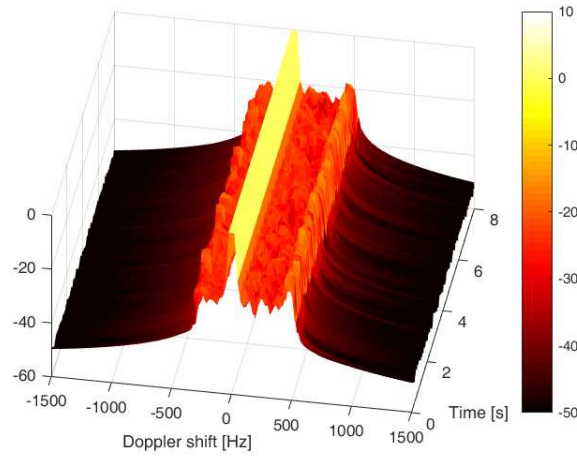


(b) Measured geometry-based channel emulator

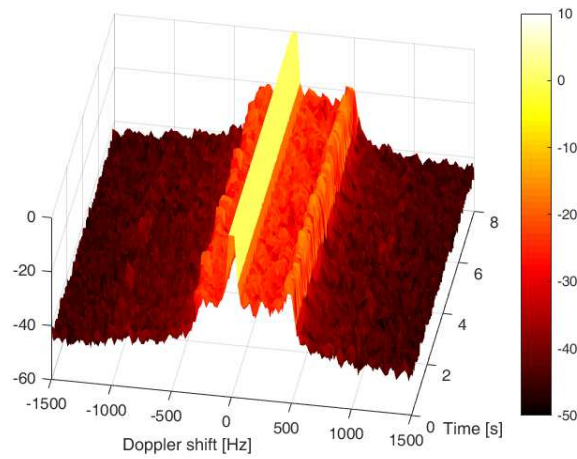


(c) PDP Error  $e_{\tau} [s']$

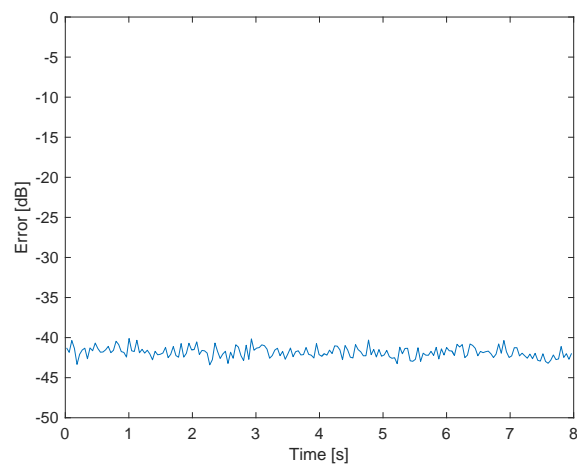
Figure 3.17: Comparison of the normalized PDPs of ETSI channel model rural LOS



(a) Numerical Simulation



(b) Measured geometry-based channel emulator



(c) DSD Error  $e_\nu[s']$

Figure 3.18: Comparison of the normalized DSDs of ETSI channel model rural LOS



## 4 Channel Emulation in Vehicle-in-the-Loop Tests

Connected autonomous vehicles exchange information using wireless vehicle-to-everything (V2X) communication to improve road safety and travelling convenience, reducing traffic congestion, minimizing fuel consumption and enhancing the overall driving experience [7, 15]. In fully automated driving systems real-time control algorithms integrated in the automated vehicle's control unit, will use this information to adapt the driving route and velocity to the current traffic situation. As already discussed in the previous sections, the performance of wireless communication systems is fundamentally determined by the properties of the underlying wireless communication channel. Vehicular communication channels exhibit time-variant multi-path propagation with non-stationary channel statistics, which makes wireless communication challenging. In safety relevant scenarios URLLC links are of paramount importance. For developing and validating URLLC links, the wireless communication system together with the real-time control algorithm has to be tested in a repeatable fashion in vehicular environments.

In this part of the thesis, we validate the vehicle-in-the-loop (ViL) test of V2X communication links by means of time-variant channel emulation [26]. ViL tests [108] have the benefit of being repeatable, while tests on the road are labor intensive and hard to repeat due to the influence of variables that cannot be controlled. A ViL test combines a real vehicle with a virtual environment, where all relevant stimuli for sensors are simulated. To reproduce the wireless communication effects, a wireless channel emulator is used. In most ViL tests only very simple channel models are utilized, such as basic path-loss (e.g., Friis law) or delay models and stationary statistics [109, 110]. A realistic validation of wireless communication systems in ViL tests requires the update of wireless propagation characteristics in *real-time* with continuous variations in delay and Doppler according to the change of the position and velocity of the TX and RX.

We perform the validation of wireless V2X communication in ViL tests by comparing the RSSI and PER of measurements on a proving ground with the RSSI and PER obtained from ViL tests. For the ViL tests, the wireless communication channel is emulated using the geometry-based channel emulator introduced in the previous section, that allows to emulate continuously changing path delays and Doppler shifts.

The channel emulator is parameterized by a GSCM, which is updated in real-time, dependent on the position and velocity of the vehicles to emulate. The position and velocity of the vehicles are updated in real-time by Virtual Test Drive<sup>®</sup> by VIRE Simulationstechnik GmbH.

### 4.1 Scenario Description

We selected driving routes and traffic scenarios, to measure and emulate the wireless channel statistics for a left turning vehicle, as illustrated in Figure 4.1.

The vehicle of interest is a Volkswagen (VW) E-Golf and henceforth denoted as *test vehicle*, which is confronted with different traffic situations such as (a) another vehicle (VW T5; length: 5292 mm, height: 2476 mm, width: 1959 mm) crossing before turning left, (b) another vehicle (VW T5) blocking the line of sight to the base station while a vehicle (VW Passat; length: 4767 mm, height: 1516 mm, width: 1832 mm) is approaching the intersection from the opposite direction, and (c) two vehicles (VW T5 and VW Passat) approaching the intersection where the VW T5 is blocking the line of sight to the VW Passat. In each scenario there is at least one incoming vehicle approaching from the opposite side of the intersection. Since both vehicles (the test vehicle and another vehicle) meet at the center of the intersection, the driver of the test vehicle has to decide to turn before or after the incoming vehicle. Thus, each of the scenarios bear different challenges for the driver of the test vehicle where additional information received via V2X communication proves beneficial.

The incoming vehicle follows an s-curve with trees blocking the line of sight to the test vehicle. We assume that the incoming vehicles are legacy vehicles with no means of wireless communication. To compensate for the blocked view, a traffic tower is placed at the end of the s-curve, observing the vehicles approaching the intersection. The position of the visually detected vehicles is transmitted using wireless vehicle-to-infrastructure (V2I) communication based on IEEE 802.11p [111] towards the test vehicle, allowing it to compensate for the lack of sight and communicate a turn decision recommendation for the driver. The TX modem is mounted on the traffic tower at a height of 4.2 m, the RX modem is mounted in the test vehicle. At TX the antenna ECO12-5800-WHT of MobileMark with 12 dBi gain was utilized, at the RX the antenna SMW-404 also of MobileMark with a gain of 5 dBi was used. Both antennas are omni-directional.

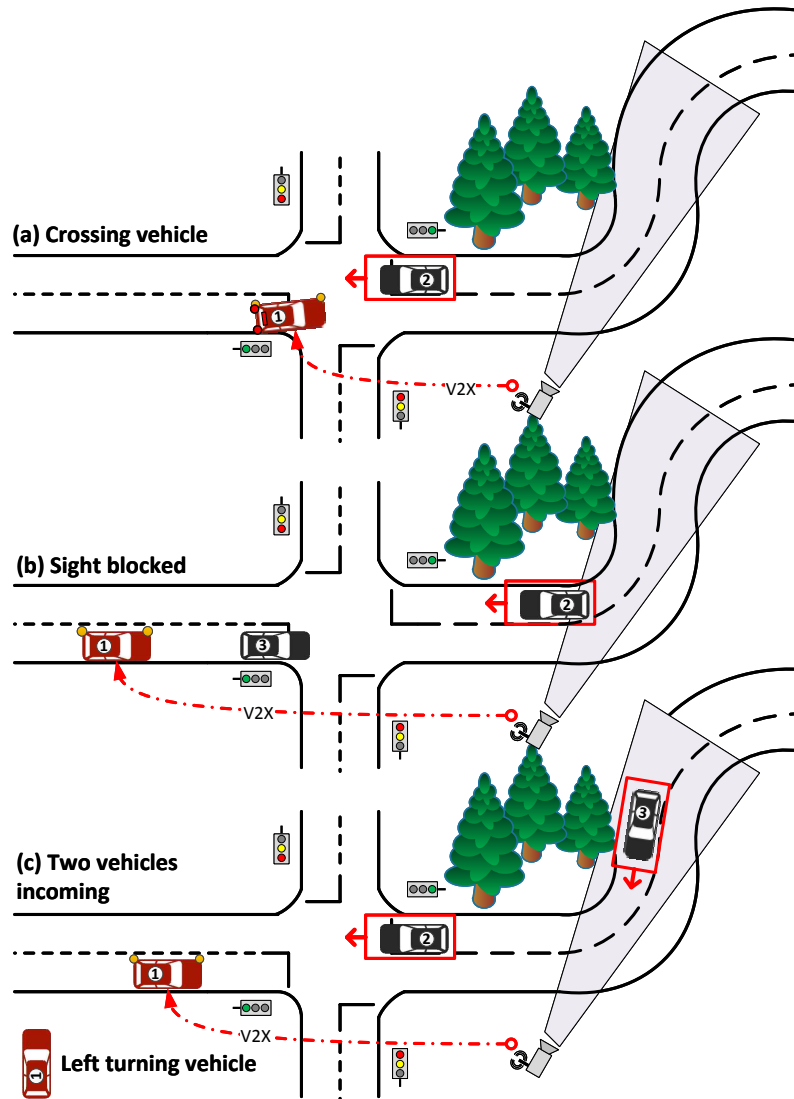


Figure 4.1: Illustration of the basic scenarios.

## 4.2 Vehicle-in-the-Loop Tests

### 4.2.1 Description of the ViL Test

For the ViL test, the system-under test (SUT) (in our case the test vehicle) is connected to a simulation environment where everything except the SUT is simulated. In our experiments, this includes, besides the visual representation, the physical properties of the environment, a virtual representation of the SUT and every moving object in the scene that modifies the measured variable(s). In order to reproduce the experiment on the test track as close as possible, the ViL tests are conducted at

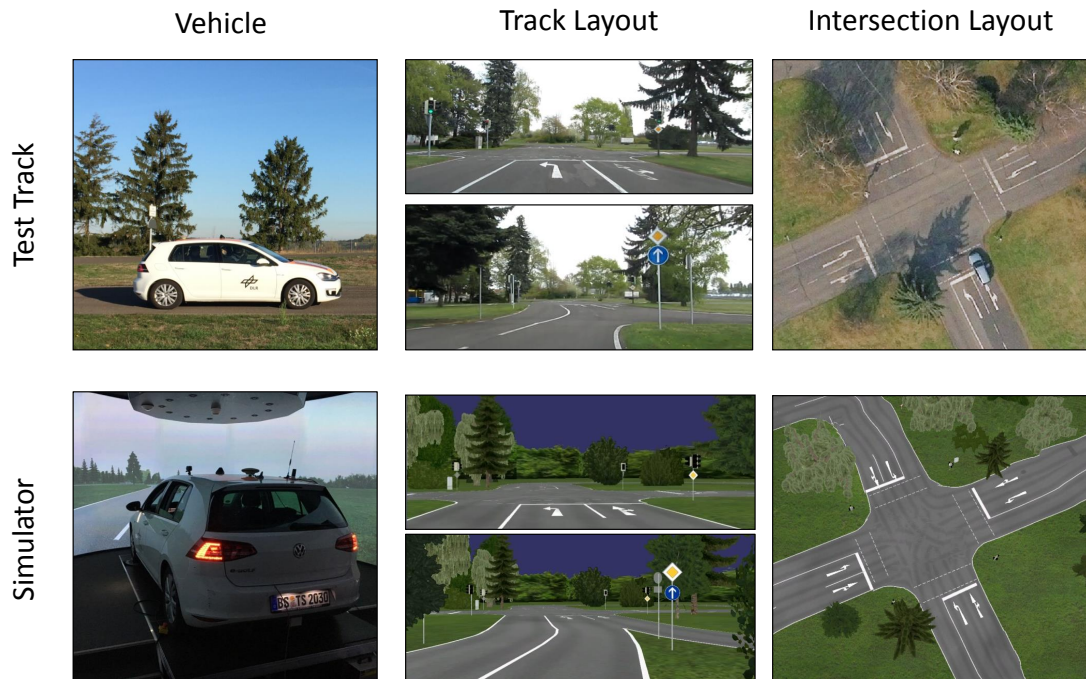


Figure 4.2: Test track recreated in simulation.

the Virtual Reality Laboratory (VRLab) at the German Aerospace Center (DLR). The VRLab is a 360° projection dome [112] with enough space to accommodate the complete test vehicle. The front tires of vehicle are positioned on a special designed force injection system that is able to simulate the forces a driver or an automation system would feel / measure on the real track. The experiment is conducted as a co-simulation, using Virtual Test Drive (VTD) <sup>®</sup> by VIRE Simulationstechnik GmbH as environment simulation and the DLR in-house framework Dominion [113]. A custom built highly accurate map of the test course is used for the simulator depicted in Figure 4.2. In the ViL test three different scenarios were reproduced (cf. Figure 4.1). The test driver drives the same route as on the actual test site.

#### 4.2.2 Wireless Channel Emulation

The wireless V2I communication channel is emulated using the real-time geometry-based wireless channel emulator [25] presented in the previous section. A schematic representation is shown in Figure 4.3. The propagation module is parameterized by the channel model, which periodically updates the geometry (position, velocity

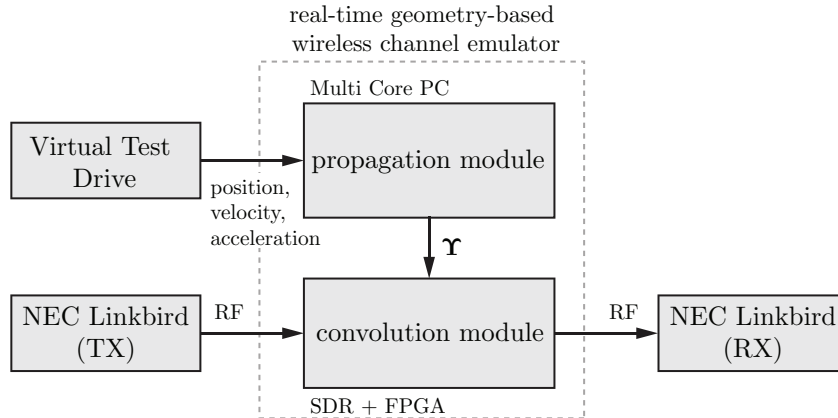


Figure 4.3: Schematics of wireless channel emulation in ViL.

and acceleration) and calculates the attenuation, delay and Doppler shift of each propagation path. The convolution module convolves the input signal with the time-variant channel impulse response to obtain the output signal. For the ViL tests a multi-core x64 machine with 16 cores is available, as SDR we use an NI USRP-2954R [98]. The SDR is connected to TX and RX via attenuators.

We parameterize the propagation module by a GSCM [60]. The model takes the traffic lights as static discrete, the vehicles as mobile discrete and the vegetation as diffuse scatterers into account. The vegetation is modeled by octagons of different sizes where the diffuse scatterers are placed randomly inside the octagons according to a certain distribution. For each test drive in each scenario a random scatterer realization of the vegetation is utilized. A schematic representation of the second traffic scenario (sight blocked) with different scatterers including the trajectories of all involved vehicles is depicted in Figure 4.4. The start position of the test vehicle (RX), is shown by a pink square, the position of the TX is shown by a pink circle. The path loss coefficients of the model are adapted from the road intersection scenario with buildings [3]. The attenuation of the vegetation is modeled according to [114, (2)]. For each position of the test vehicle the LOS condition is checked and in case of an obstructed LOS due to the vegetation the signal is attenuated according to the selected vegetation model.

The wireless propagation coefficients, i.e., path delay, Doppler shift and attenuation, are updated in real-time every  $256 \mu\text{s}$  [25] ensuring a phase continuous transition for the parameter update. The positions, velocity and acceleration of the vehicles are updated by Vires VTD every 16.6 ms. We linearly extrapolate the position and velocity until the GSCM receives a position/velocity/acceleration update.

### 4.3 Measurement and Validation

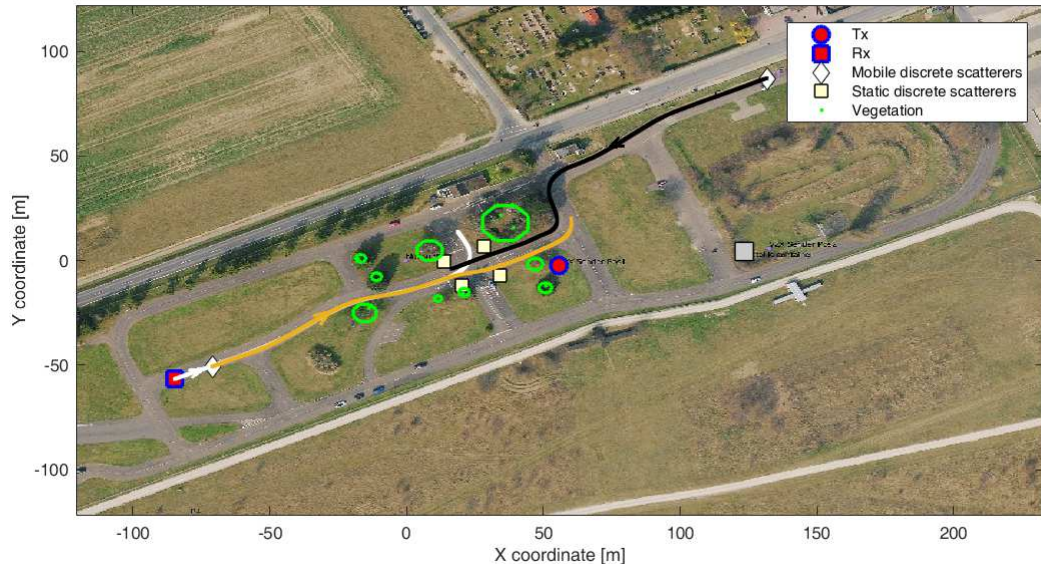


Figure 4.4: Trajectories of the vehicles for the “sight blocked” scenario and the geometry considered for real-time channel emulation with the GSCM. The white trajectory corresponds to the test vehicle, the yellow trajectory to the sight blocking VW T5 and the black trajectory to the crossing vehicle (VW Passat)

For TX and RX, common-off-the-shelf NEC Linkbird-MX 802.11p modems are used. The center frequency is set to 5.9 GHz (CH 180) and the frame repetition rate is set to 100 frames per second. We set the transmit power in both tests to 15 dBm. The data collection is split into two parts: In the first part, the measurement data on the proving ground/test site is collected at a non-public drivers testing course, north to the research airport in Braunschweig (Germany). In the second part, the ViL test is conducted using the 360° DLR driving simulator. The RSSI and PER are recorded at the RX using the NEC Linkbird-MX 802.11p modem. We calculate the PER over 100 transmitted frames. On the proving ground we additionally collect global positioning system (GPS) data for obtaining a nearest fit to the trajectory used in the ViL tests. We compare the results of the “sight blocked” scenario between the ViL tests and the measurements on the proving ground.

Figure 4.4 shows the trajectories of the different involved vehicles in the sight blocked scenario. The white trajectory corresponds to the test vehicle, the yellow trajectory to the sight blocking VW T5 and the black trajectory to the crossing vehi-

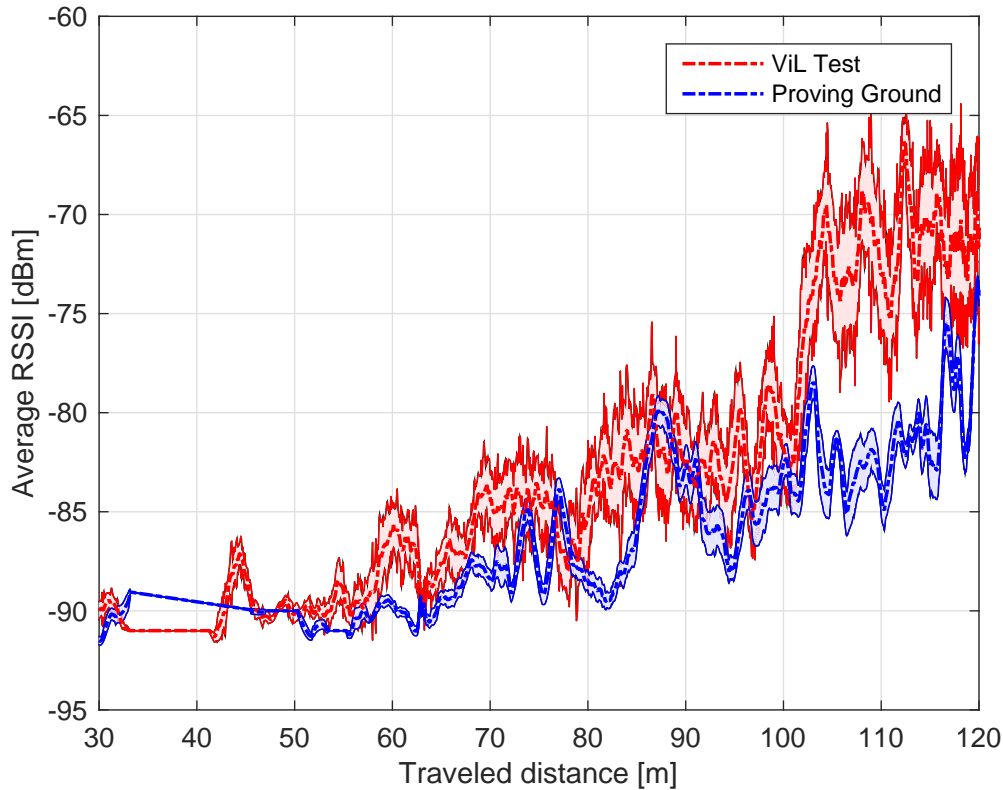


Figure 4.5: Average RSSI with (dashed line) 95 % confidence intervals (filled area) of the ViL test and the measurement on the proving ground versus the travel distance for the “sight blocked” scenario

cle (VW Passat). For the measurement on the proving ground the same trajectories are driven using real vehicles. Please note, that due to the utilized measurement method on the proving ground in the “sight blocked” scenario, the measurement on the proving ground is stopped in the middle of the road intersection.

We compare the measurement on the proving ground with the ViL test using the recorded GPS- and xy-positions obtained by the simulation. We use a common zero coordinate to transform (sphere to Cartesian, which induces a neglectable error due to the rather small area) the GPS positions to Cartesian positions in  $\mathbb{R}^3$ . In order to provide a meaningful comparison of the RSSI and PER between the measurement on the proving ground and the ViL test, we pair those ViL test positions ( $V \subset \mathbb{R}^3$ ) and proving ground positions ( $G \subset \mathbb{R}^3$ ), which have the smallest error with respect to the Euclidean distance

$$M = \{(v, g) : v \in V, g = \underset{u \in G}{\operatorname{argmin}}\{\|v - u\|_2\}\}. \quad (4.1)$$

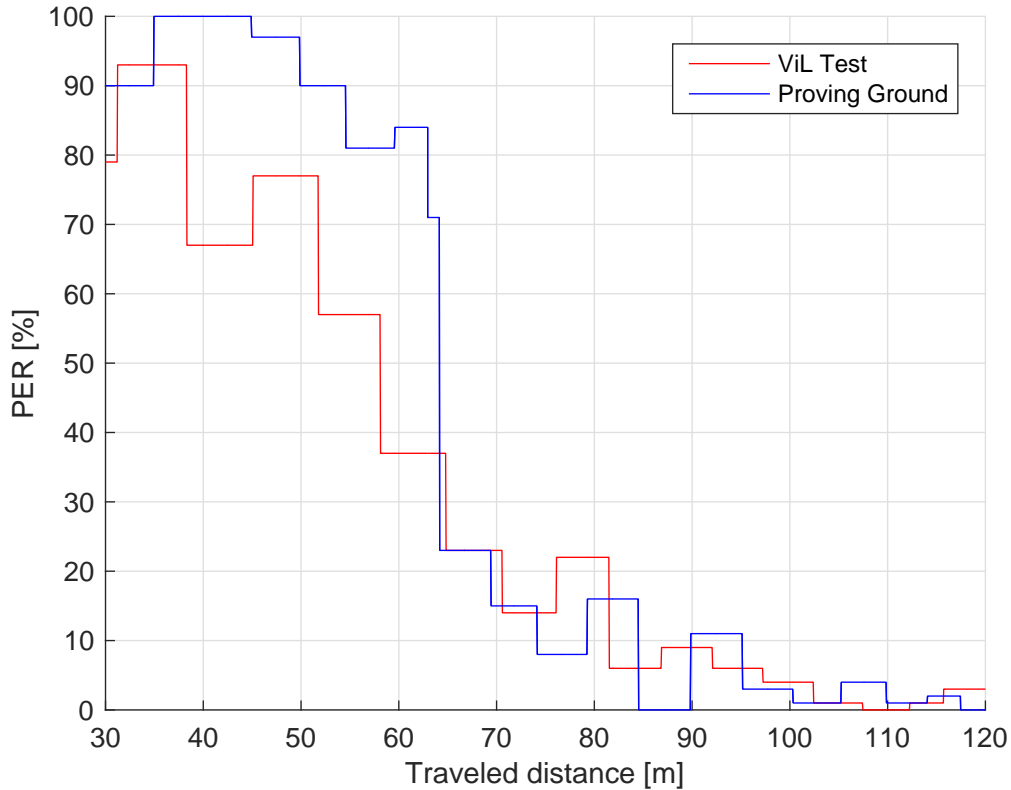


Figure 4.6: PER of the ViL test and the measurement on the proving versus the travel distance for the “sight blocked” scenario.

From the obtained data points we calculate the RSSI of the ViL test and the measurement on the proving ground as an average of 30 subsequent positions in space. With an average speed of 20 km/h and 10 ms between samples, the 30 subsequent positions result in an averaging distance of 1.67 m ( $\approx 33 \lambda$  for 5.9 GHz). We evaluate the RSSI and the PER versus the traveled distance of the RX. The traveled distance is calculated as the Euclidean distance between the current position of the test vehicle (in the ViL test or the measurement on the proving ground) and its start position. For the utilized transmit power (15 dBm) no signal was received within the first 30 m of the travel distance. Hence, we omitted this part in the following plots.

Figure 4.5 shows the average RSSI (dashed lines) versus the traveled distance for the ViL test and the measurement on the proving ground, respectively. We additionally plot the 95 % confidence intervals of the averaged RSSI, which are calculated from 30 subsequent positions in space. As expected, the average RSSI increases with the traveled distance, since the RX moves closer to the TX. Comparing the average

RSSI of the ViL test and with corresponding measurement on the proving ground it can be observed that the GSCM is able to capture the changing path loss due to the changing distance over time. The, on average, higher received RSSI of the ViL test is due to the too small assumed path loss coefficients in the GSCM. Furthermore, it can be observed that the variance of the short term average RSSI of the ViL test is higher than the variance of the short term average RSSI of the measurement on the proving ground. This can be explained by the utilized large-scale fading model of the path loss coefficients, which assumes a too high variance of the large-scale fading coefficient. Lastly, due to the available computing hardware for the ViL test, the geometry of the proving ground has not been modelled to its full extent in the GSCM, which also influences the accuracy of the obtained results. Thus, for future measurements, calibrating the parameterization of the GSCM, i.e., path loss and large-scale coefficients and increasing the level of detail for the geometry used in the ViL test will lead to a further improved match between the results from proving ground and ViL test.

Figure 4.6 shows the PER versus the traveled distance for the ViL test and the measurement on the proving ground, respectively. The PER curves show similar behavior. From 40 m to approximately 60 m traveled distance the PER of the ViL test is smaller compared to the measurement on the proving ground. This can be explained by the higher RSSI in the ViL test. After around 70 m traveled distance the PER of the ViL test and the measurement on the proving ground match approximately. In this case the RSSI of both measurements is high enough such that the sensitivity of the modems does not have a significant influence on the PER.

## 4.4 Discussion

In this section we showed the validation of a V2X communication system test using a ViL setup. We introduced the scenario and the measurement setup in detail. In the ViL test the wireless communication channel is updated in real time using a GSCM that obtains the positions of the vehicles via Virtual Test Drive. The results show that the ViL test can reproduce the PER and RSSI values which were obtained by measurements on a proving ground with some systematic deviations. We conclude that for future tests the parameterization of the utilized GSCM for this scenario, especially the large-scale fading and the path loss coefficients, has to be calibrated by measurement data to obtain a closer match. To the best of our knowledge this is the first time a real-time updated GSCM was used for ViL communication system tests.



# Part II

## Adaptive Iterative Channel Estimation



Die approbierte gedruckte Originalversion dieser Dissertation ist an der TU Wien Bibliothek verfügbar.  
The approved original version of this doctoral thesis is available in print at TU Wien Bibliothek.

# 5 Adaptive Iterative Non-Stationary Channel Estimation for LTE Communications

## 5.1 Introduction

Many latency critical mobile applications such as autonomous driving, real-time online gaming and virtual reality require tactile speed with latency approaching the millisecond range [4,7,115]. Matching this services with cloud-computing requires the transmission of data from the end users to nodes in the core networks or data centers often tens of kilometers away or across continents [115], which is unacceptable for latency sensitive services. To tackle this problem mobile edge computing (MEC) [116] was introduced, which is a new network architecture concept that provides cloud-computing capabilities at the edge of the mobile network [115–117] in close proximity (tens to hundreds of meters) of mobile devices. Emerging applications will benefit from MEC by offloading their computation intensive task to MEC servers for cloud execution.

The latency of mobile services depends mainly on the propagation, computation and communication delay, which in turn depends on propagation distance, computation speeds and data rate. Advanced channel estimation techniques reduce latency, since, e.g., re-transmissions of data packets due to wrong detection can be avoided. For low latency communication in vehicular scenarios, channel estimation methods are required that can deal with high delay- and Doppler spreads in non-stationary propagation conditions where the delay and Doppler spread changes over time [2,39,40].

A robust reduced-rank iterative channel estimator that relies on a correlation matrix assuming a flat delay-Doppler scattering function, was presented in [32,118]. The support region of the scattering function is defined by the maximum delay-spread and the maximum Doppler-spread of the channel. The eigenvectors of the channels autocorrelation matrix can be approximated by a two dimensional subspace model using DPS sequences [94,96]. Such an approach is mismatched to the actual support of the scattering function.

To improve the performance an adaptive subspace selection algorithm that estimates the actual delay and Doppler support of the current channel realization is presented in [32] for the specific pilot pattern of the IEEE 802.11p [111] standard. This pilot pattern provides a contiguous pilot grid in time and frequency which is a crucial requirement for the subspace selection algorithm [119].

For our investigation we consider an LTE downlink pilot pattern and modulation format. This pilot pattern is not contiguous, which means the subspace selection algorithm presented in [119] cannot be directly utilized. We present an iterative reduced-rank channel estimator for the LTE downlink utilizing a subspace representation based on discrete prolate spheroidal sequences for a non-contiguous, equidistant pilot grid, and provide a performance evaluation based on numerical simulation results for doubly-selective channels [21]. The subspace is adapted to the time-varying delay and Doppler-spread for each received frame with a hypothesis test. We extend the iterative reduced rank channel estimation algorithm of [32, 97] to higher order modulation alphabets. With this setup we can achieve a two fold reduction in the number of required iterations to achieve a PER below  $10^{-1}$  for a relative velocity range of 0 to 400 km/h, and a delay spread of 0 to  $4.7 \mu\text{s}$  at a signal-to-noise ratio (SNR) of 13 dB. Since the estimator adapts to the statistics of the channel the number of iterations can be reduced, which allows for shorter processing delay.

For the hypothesis test, the optimum number of hypotheses is not known, which influences the channel estimation performance as well as the PER. We investigate the number of hypotheses by numerical simulations and find a method to choose the hypotheses with a good trade-off between mean-squared channel estimation error and the complexity of the hypothesis test [22].

## 5.2 System Model

We assume a modulation scheme based on a SISO LTE downlink as shown in Fig 5.1. An information bit stream  $\epsilon[m'']$  with discrete time  $m''$  is turbo encoded, interleaved and rate matched, resulting in the coded bit stream  $c[m']$ . Subsequently,  $c[m']$  is partitioned into vectors  $\mathbf{t} = (t_1, t_2, \dots, t_K)$  of length  $K$ , which are converted to complex data symbols  $b$  utilizing a symbol alphabet  $\mathcal{B}$  [120, Sec. 7.1], which is either 4-, 16- or 64-QAM. The data symbols are mapped to the orthogonal frequency division multiple access (OFDM) time-frequency grid of an LTE subframe. Each subframe has a duration of 1 ms in the time domain and, depending on the overall system bandwidth, consists of 6 up to 100 resource block pairs (RBPs)  $N_{\text{RBP}}$  in the frequency domain. The RBP is the minimum scheduling unit in LTE. For a normal cyclic prefix (CP) length a RBP entails 14 OFDM symbols in the time direction and

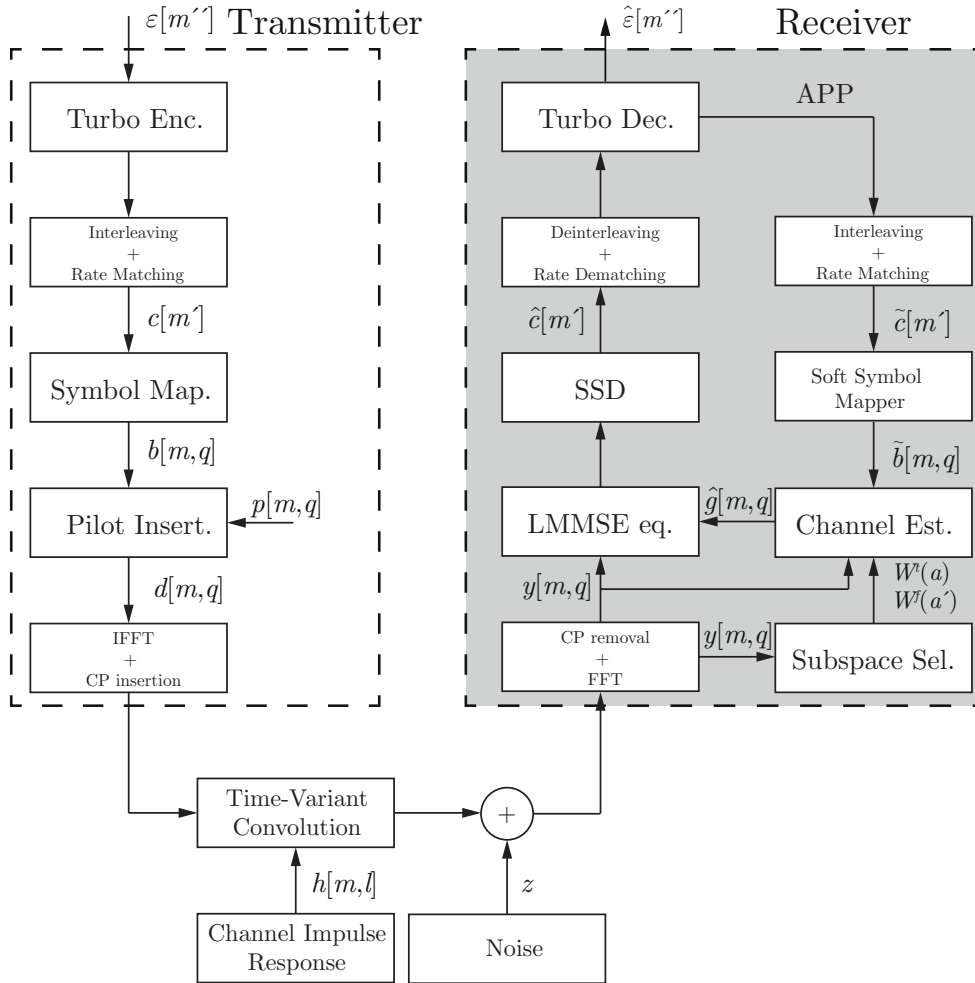


Figure 5.1: SISO LTE downlink system model

12 subcarriers in the frequency direction. The time-frequency grid for a subframe with normal CP length is shown in Fig. 5.2 on page 78.

Pilot symbols  $p[m, q]$  are inserted in the time-frequency grid to estimate the channels time-frequency response, where  $m \in \{0, \dots, M - 1\}$  denotes discrete time and  $q \in \{0, \dots, N - 1\}$  discrete frequency. The size of  $M$  and  $N$  depends on the number of considered subframes and the number of RBPs within one subframe. The pilot symbols are element of a 4-QAM symbol alphabet and assumed to be known to the receiver.

The multiplexing operation of data and pilot symbols can be described as

$$d[m, q] = b[m, q] + p[m, q], \quad (5.1)$$

where  $b[m, q]$  denotes the coded data symbols. The data symbol positions are defined

by the two dimensional index set  $\mathcal{S}$ , while the pilot symbol positions are defined by the two dimensional index set  $\mathcal{P}$ . The two index sets are complementary, i.e.,  $\mathcal{S} \cap \mathcal{P} = 0$ , or  $b[m, q] = 0 \forall (m, q) \notin \mathcal{S}$  and vice versa. After inverse fast Fourier transform (IFFT) and CP insertion the signal is transmitted over a time-variant frequency-selective channel  $h(t, \tau)$ . The discretized channel impulse response can be represented by

$$h[m''', l] := h(m'''T_C, lT_C). \quad (5.2)$$

Here,  $m'''$  denotes the discrete time index,  $l$  the discrete delay index,  $1/T_C = N' \cdot \Delta f$  the sampling rate,  $N'$  the FFT size and  $\Delta f = 15$  kHz the subcarrier spacing. We assume that the time-variant channel impulse response has a maximum support of  $0 \leq l \leq L' - 1$  with  $L' = \lceil \tau_{\max}/T_C \rceil$ , where  $\tau_{\max}$  denotes the maximum path delay of the communication channel. To avoid inter-symbol interference (ISI) the maximum path delay is restricted to be shorter than or equal to the CP length of the OFDM symbols. We assume that for the considered scenario the inter-carrier interference (ICI) has only a minor impact on the receiver performance [32]. In this case, after fast Fourier transform (FFT) and CP removal, the received signal  $y[m, q]$  can be modeled as

$$y[m, q] = g[m, q]d[m, q] + z[m, q], \quad (5.3)$$

where the channel coefficient  $g[m, q]$  is the FFT of  $h[m''', l]$  sampled at  $h[m(N' + L) + L + N'/2, l]$  and  $z[m, q] \sim \mathcal{CN}(0, \sigma_z^2)$  the symmetric complex additive white Gaussian noise with zero mean and covariance  $\sigma_z^2$ , respectively.

The received signal is input to a max-log soft sphere decoder (SSD) [121] that uses the estimated channel coefficients  $\hat{g}[m, q]$  to generate the log-likelihood ratios (LLRs) of the encoded data bits  $\hat{c}[m']$ . After rate-dematching and deinterleaving the LLRs are fed to the turbo decoder. The turbo decoder generates the a posteriori LLRs of the information bit stream. After hard decision this results in the received information bit stream  $\hat{e}[m'']$ . The a posteriori LLRs of the information bit stream bits are utilized as soft information feedback to improve the channel estimator performance.

### 5.3 Iterative Channel Estimation

To obtain the estimated channel coefficients  $\hat{g}[m, q]$  we use an iterative channel estimator. The LLRs obtained by the turbo decoder are utilized as a priori information to generate soft symbol feedback that is used to improve the estimator performance in each iteration step. Defining the received vector  $\mathbf{y} \in \mathbb{C}^{MN \times 1}$  by

$$\mathbf{y} = [y[0, 0], y[0, 1], \dots, y[0, N - 1], \dots, y[M - 1, 0], y[M - 1, 1], \dots, y[M - 1, N - 1]]^T \quad (5.4)$$

we can rewrite (5.3) in matrix-vector notation according to

$$\mathbf{y} = \mathbf{D}\mathbf{g} + \mathbf{z}. \quad (5.5)$$

The channel vector  $\mathbf{g} \in \mathbb{C}^{MN \times 1}$ , symbol vector  $\mathbf{d} \in \mathbb{C}^{MN \times 1}$  and noise vector  $\mathbf{z} \in \mathbb{C}^{MN \times 1}$  are similarly defined to (5.4) and  $\mathbf{D} = \text{diag}(\mathbf{d}) \in \mathbb{C}^{MN \times MN}$  is a diagonal matrix. To incorporate the soft symbol feedback we substitute  $\mathbf{D}$  in (5.5) by  $\tilde{\mathbf{D}} = \text{diag}(\tilde{\mathbf{d}})$ . The  $MN \times 1$  sized vector  $\tilde{\mathbf{d}}$  has elements

$$\tilde{d}[m, q] = \tilde{b}[m, q] + p[m, q], \quad (5.6)$$

and  $\tilde{b}[m, q]$  are the soft data symbols on the index set  $\mathcal{S}$  that are obtained from the rate-matched, interleaved LLRs of the turbo decoder.

### 5.3.1 Wiener Filter

To estimate the channel vector  $\mathbf{g}$  we use a linear minimum mean squared error (LMMSE) estimator. Following the derivation in [122, (36)-(39)] we obtain the well known Wiener-Filter

$$\hat{\mathbf{g}} = \mathbf{R}_g \tilde{\mathbf{D}}^H \left( \tilde{\mathbf{D}} \mathbf{R}_g \tilde{\mathbf{D}}^H + \mathbf{\Lambda} + \sigma_z^2 \mathbf{I}_{MN} \right)^{-1} \mathbf{y}, \quad (5.7)$$

that provides the channel estimate  $\hat{\mathbf{g}}$ . Here,  $(\cdot)^H$  is the conjugate transpose,  $\mathbf{R}_g = E\{\mathbf{g}\mathbf{g}^H\} \in \mathbb{C}^{MN \times MN}$  is the channel autocorrelation matrix (see also Section 5.3.3),  $\mathbf{I}_{MN}$  is the identity matrix, and  $\mathbf{\Lambda}$  is a diagonal matrix that incorporates the variances of the symbols  $\tilde{d}[m, q]$ . All matrices are of size  $MN \times MN$ . The elements of  $\mathbf{\Lambda}$  are calculated by

$$[\mathbf{\Lambda}]_{m+Mq, m+Mq} = [\mathbf{R}_g]_{m+Mq, m+Mq} \sigma_{\tilde{d}[m, q]}^2, \quad (5.8)$$

with  $\sigma_{\tilde{d}[m, q]}^2$  denoting the variance of  $\tilde{d}[m, q]$ . The entries on the diagonal of  $\mathbf{\Lambda}$  are zero for pilot positions  $(m, q) \in \mathcal{P}$  since  $\sigma_{p[m, q]} = 0$  for known pilot symbols. In the first iteration loop no LLR information is available and only the pilot symbols are used for channel estimation, i.e.,  $\tilde{d}[m, q] = 0$  and  $\sigma_{\tilde{d}[m, q]}^2 = 1 \forall (m, q) \in \mathcal{S}$ . From the second iteration on, we utilize the pilot symbols  $p[m, q]$  and the soft data symbols  $\tilde{b}[m, q]$  for channel estimation.

### 5.3.2 Soft Symbol Calculation

To calculate the soft data symbols  $\tilde{b}[m, q]$  and variances  $\sigma_{\tilde{b}[m, q]}^2$  on the data symbol positions  $(m, q) \in \mathcal{S}$  we partition the LLR stream  $\tilde{c}[m']$  into vectors  $\mathbf{c} = (c_1, c_2, \dots, c_K)$

of size  $K$  which contain the LLRs of the corresponding bit vector  $\mathbf{t} = (t_1, t_2, \dots, t_K)$ . Neglecting for sake of simplicity the mapping indices  $(m, q)$ , the soft data symbols and variances are calculated according to [123]

$$\tilde{b} = \bar{b} = \sum_{b_i \in \mathcal{B}} b_i \cdot P(b = b_i), \quad (5.9)$$

$$\sigma_b^2 = \left( \sum_{b_i \in \mathcal{B}} |b_i|^2 \cdot P(b = b_i) \right) - |\tilde{b}|^2, \quad (5.10)$$

where  $b_i$  is the  $i$ -th symbol within the utilized symbol alphabet  $\mathcal{B}$  (4-,16- or 64-QAM) and each  $b_i \in \mathcal{B}$  corresponds to  $K$  bits  $\mathbf{t}_i = (t_{i,1}, \dots, t_{i,K})$ , with  $K = \log_2(|\mathcal{B}|)$  and  $|\mathcal{B}|$  is the cardinality of the symbol alphabet  $\mathcal{B}$ .

If we assume that due to interleaving the data bits of  $\mathbf{t}$  are independent, the symbol probabilities  $P(b = b_i)$  are calculated according to [123]

$$P(b = b_i) = \prod_{k=1}^K \frac{1 + \tilde{t}_{i,k} u_k}{2}. \quad (5.11)$$

Here  $t_{i,k}$  is the  $k$ -th data bit of the symbol  $b_i$  and

$$\tilde{t}_{i,k} = \begin{cases} +1, & t_{i,k} = 0, \\ -1, & t_{i,k} = 1 \end{cases} \quad (5.12)$$

The variable  $u_k = \tanh(c_k/2)$  is obtained by the hyperbolic tangent of the LLR of the corresponding data bit  $t_k$ .

Taking the bit-symbol mapping of [124, Sec 7.1.2 - 7.1.4] into account we can simplify the calculation of the symbol statistics and obtain [21]

#### 4-QAM

$$\tilde{b} = \frac{u_1 + ju_2}{\sqrt{2}} \quad (5.13)$$

$$\sigma_b^2 = 1 - |\tilde{b}|^2 \quad (5.14)$$

#### 16-QAM

$$\tilde{b} = \frac{(2u_1 - u_1u_3) + j(2u_2 - u_2u_4)}{\sqrt{10}} \quad (5.15)$$

$$\sigma_b^2 = 1 - \frac{2}{5}(u_3 + u_4) - |\tilde{b}|^2 \quad (5.16)$$

## 64-QAM

$$\tilde{b} = \frac{u_1(4 - u_3(2 - u_5)) + ju_2(4 - u_4(2 - u_6))}{\sqrt{42}} \quad (5.17)$$

$$\begin{aligned} \sigma_{\tilde{b}}^2 &= 1 + \frac{2}{21}(u_6(2u_4 - 1) + u_5(2u_3 - 1)) \\ &\quad - \frac{8}{21}(u_3 + u_4) - |\tilde{b}|^2 \end{aligned} \quad (5.18)$$

These calculations are also performed in [125], however there is an sign error in the calculation of the variances of the 64-QAM alphabet.

## 5.3.3 Robust Reduced Rank Approximation

The channel autocorrelation matrix  $\mathbf{R}_{\mathbf{g}}$  is in general not known to the receiver. To circumvent this problem we approximate the autocorrelation matrix  $\mathbf{R}_{\mathbf{g}}$  in (5.7) by a robust autocorrelation matrix  $\tilde{\mathbf{R}}_{\mathbf{g}}$  that assumes a flat delay-Doppler scattering function within a two dimensional support region

$$\mathcal{W} = W^t \times W^f = [-\nu_D, \nu_D] \times [0, \theta_P]. \quad (5.19)$$

For the one sided normalized Doppler bandwidth  $\nu_D$  of the DSD support region  $W^t$  we assume  $0 \leq \nu_D < \nu_{D\max}$  with  $\nu_D = \omega_D T_S$ ,  $\omega_D$  the Doppler frequency and  $T_S$  the OFDM symbol duration. The Doppler frequency is obtained by  $\omega_D = f_c v / c_0$ , with  $v$  the relative velocity between transmitter and receiver,  $c_0$  the speed of light and  $f_c$  the carrier frequency of the system. Likewise, we assume for the normalized delay  $\theta_p$  of the PDP support region  $W^f$  that  $0 \leq \theta_p < \theta_{P\max}$  with  $\theta_p = \tau_p / (N' T_C)$  and  $\tau_p$  the path delay of path  $p$ . The parameters  $\nu_D$  and  $\theta_P$  to calculate  $\mathbf{R}_{\mathbf{g}}$  can be obtained by a hypothesis test that is presented in Section 5.4. If the number of hypotheses is finite all relevant matrices can be precalculated and stored, which significantly reduces the complexity.

For an autocorrelation matrix with flat delay-Doppler support the eigenvectors  $\mathbf{U}(\mathcal{W}, \mathcal{I})$  of

$$\tilde{\mathbf{R}}_{\mathbf{g}} = \mathbf{U}(\mathcal{W}, \mathcal{I}) \mathbf{\Sigma}(\mathcal{W}, \mathcal{I}) \mathbf{U}(\mathcal{W}, \mathcal{I})^H, \quad (5.20)$$

are also spanned by the two dimensional subspace of DPS sequences where  $\mathbf{\Sigma}(\mathcal{W}, \mathcal{I})$  is the diagonal matrix of eigenvalues and  $\mathcal{I} = I^t \times I^f = [0, \dots, M - 1] \times [-N/2, \dots, N/2 - 1]$  is the finite index set where the fading process is observed on. Specifically, we can factorize

$$\tilde{\mathbf{R}}_{\mathbf{g}} = \mathbf{R}(W^t, I^t) \otimes \mathbf{R}(W^f, I^f), \quad (5.21)$$

with  $\otimes$  denoting the Kronecker product. The eigenvectors  $\mathbf{U}(W, I)$  of the autocorrelation matrix  $\mathbf{R}(W, I)$  are generalized DPS sequences [97] allowing to calculate  $\mathbf{U}(\mathcal{W}, \mathcal{I})$  by

$$\mathbf{U} = \mathbf{U}(\mathcal{W}, \mathcal{I}) = \Pi(\mathbf{U}(W^t, I^t) \diamond \mathbf{U}(W^f, I^f)), \quad (5.22)$$

where the operator  $\diamond$  is the Tracy-Singh product of column-wise partitioned matrices [97]. The diagonal matrix  $\mathbf{\Sigma}$  is obtained by

$$\mathbf{\Sigma} = \mathbf{\Sigma}(\mathcal{W}, \mathcal{I}) = \Pi(\text{diag}(\boldsymbol{\sigma}(W^t, I^t) \otimes \boldsymbol{\sigma}(W^f, I^f))), \quad (5.23)$$

and  $\boldsymbol{\sigma}(W, I)$  are the eigenvalues of  $\mathbf{R}(W, I)$ . The permutation operator  $\Pi(\cdot)$  ensures that the columns of  $\mathbf{\Sigma}$  (and  $\mathbf{U}$ ) are sorted from biggest to smallest eigenvalue, i.e.,  $\lambda_0(\mathcal{W}, \mathcal{I}) \geq \lambda_1(\mathcal{W}, \mathcal{I}) \geq \dots \geq \lambda_{|\mathcal{I}|-1}(\mathcal{W}, \mathcal{I})$ . The eigenvalue matrix  $\mathbf{\Sigma}$  has only  $D$  dominant eigenvalues which allows us to approximate  $\tilde{\mathbf{R}}_{\mathbf{g}}$  by a robust reduced-rank matrix  $\check{\mathbf{R}}_{\mathbf{g}} \approx \tilde{\mathbf{R}}_{\mathbf{g}} = \mathbf{U}_D \mathbf{\Sigma}_D \mathbf{U}_D^H$  where  $\mathbf{U}_D$  and  $\mathbf{\Sigma}_D$  contain the first  $D$  columns of  $\mathbf{U}$  and  $\mathbf{\Sigma}$ , respectively. The dimension  $D$  is obtained by a bias-variance trade-off [97]

$$D = \underset{\mathcal{D} \in \{1, \dots, |\mathcal{I}|\}}{\text{argmin}} \left( \frac{1}{|\mathcal{W}||\mathcal{I}|} \sum_{i=\mathcal{D}}^{|\mathcal{I}|-1} \lambda_i(\mathcal{W}, \mathcal{I}) + \frac{\mathcal{D}}{|\mathcal{I}|} \sigma_z^2 \right). \quad (5.24)$$

Inserting  $\check{\mathbf{R}}_{\mathbf{g}}$  in (5.7) allows for further significant complexity reduction.

## 5.4 Adaptive Subspace Selection for a Non-Contiguous Equidistant Pilot Grid

Approximating the autocorrelation matrix  $\mathbf{R}_{\mathbf{g}}$  with a robust autocorrelation matrix  $\tilde{\mathbf{R}}_{\mathbf{g}}$  that assumes maximum Doppler support  $\nu_{D\max}$  and delay support  $\theta_{P\max}$  would obviously lead to a mismatch to the current channel realization. Direct estimation of the autocorrelation matrix from a single observation would lead to high estimation errors due to the short frame length and the low duty cycle of URLLC data traffic [32, 96]. Advanced estimators like in [126] do not consider the case when the number of observed realizations of a statistical process is smaller than the observation dimension. Therefore a hypothesis test is utilized. The hypothesis test is based on the subspace selection algorithm of Beheshti et al. [119] and was applied in [32, 96, 97] for frame based hypothesis testing on a contiguous, equidistant pilot grid. For the non-contiguous, equidistant pilot grid of the LTE downlink the hypothesis test has to be adapted. We use the observations at the pilot positions  $\mathcal{P}$  to estimate the support of the DSD  $W^t = [-\nu_D, \nu_D] \subset [-\nu_{D\max}, \nu_{D\max}]$  and the support of the PDP  $W^f = [0, \theta_p] \subset [0, \theta_{P\max}]$ .

The signal model for channel estimation at the pilot positions  $\mathcal{P}$  is given by

$$\mathbf{y}_p = \mathbf{D}_p \mathbf{g}_p + \mathbf{z}_p, \quad (5.25)$$

with  $\mathbf{D}_p = \text{diag}(\mathbf{d}_p)$ , where  $\mathbf{y}_p$ ,  $\mathbf{d}_p$ ,  $\mathbf{g}_p$  and  $\mathbf{z}_p$  contain the respective elements for  $(m, q) \in \mathcal{P}$  sorted in the same order as  $\mathbf{y}$  in (5.4). The correlated 2-D observations at the pilot positions  $\mathcal{P}$  are obtained according to

$$\mathbf{w}_p = \mathbf{D}_p^H \mathbf{y}_p = \mathbf{g}_p + \mathbf{D}_p^H \mathbf{z}_p = \mathbf{g}_p + \mathbf{z}'_p, \quad (5.26)$$

where  $\mathbf{z}'_p \sim \mathcal{CN}(0, \sigma_z^2 \mathbf{I}_{|\mathcal{P}|})$  has the same statistics as  $\mathbf{z}_p$ . The fading process observed on the pilot symbols  $\mathcal{P}$  can also be described by the eigenvectors  $\mathbf{U}_p$  of the autocorrelation matrix

$$\tilde{\mathbf{R}}_{\mathbf{g}_p} = \mathbf{U}_p \Sigma_p \mathbf{U}_p^H \quad (5.27)$$

with

$$\tilde{\mathbf{R}}_{\mathbf{g}_p} = E \{ \mathbf{g}_p \mathbf{g}_p^H \}. \quad (5.28)$$

For  $\tilde{\mathbf{R}}_{\mathbf{g}_p}$  we assume a flat delay-Doppler scattering function. We use the eigenvectors  $\mathbf{U}_p$  to perform the hypothesis test, which selects the support in the delay- and Dopplerdomain that fits for the current channel realization best. In the next Section we show how to obtain the eigenvectors of the autocorrelation  $\tilde{\mathbf{R}}_{\mathbf{g}_p}$  for the specific pilot grid of the LTE downlink and utilize them in the hypothesis test.

### 5.4.1 Non-Contiguous, Equidistant Pilot Pattern Partitioning

Since the condition number of  $\tilde{\mathbf{R}}_{\mathbf{g}_p}$  is high and the pilot pattern  $\mathcal{P}$  for the LTE downlink cannot directly be factorized in a Cartesian product (see Fig. 5.2), we cannot use the eigenvectors obtained by regular decomposition methods to setup the subspaces for the hypothesis test. Furthermore, we cannot use DPS sequences directly for the subspace setup of  $\mathbf{U}_p$  since they are originally defined on a contiguous pilot pattern. Our novel solution to this problem is as follows [21]: We partition  $\mathcal{P}$  into two two-dimensional index sets  $\mathcal{I}_c$  and  $\mathcal{I}_d$  as shown in Fig. 5.2. Each of these index sets can be defined as a Cartesian product of an index set in the time and the frequency domain according to

$$\mathcal{I}_c = I_c^t \times I_c^f \quad \text{and} \quad \mathcal{I}_d = I_d^t \times I_d^f. \quad (5.29)$$

The time index sets are defined by

$$I_c^t = \Delta_t k_t + 1 \quad \text{and} \quad I_d^t = I_c^t + \Delta x, \quad (5.30)$$

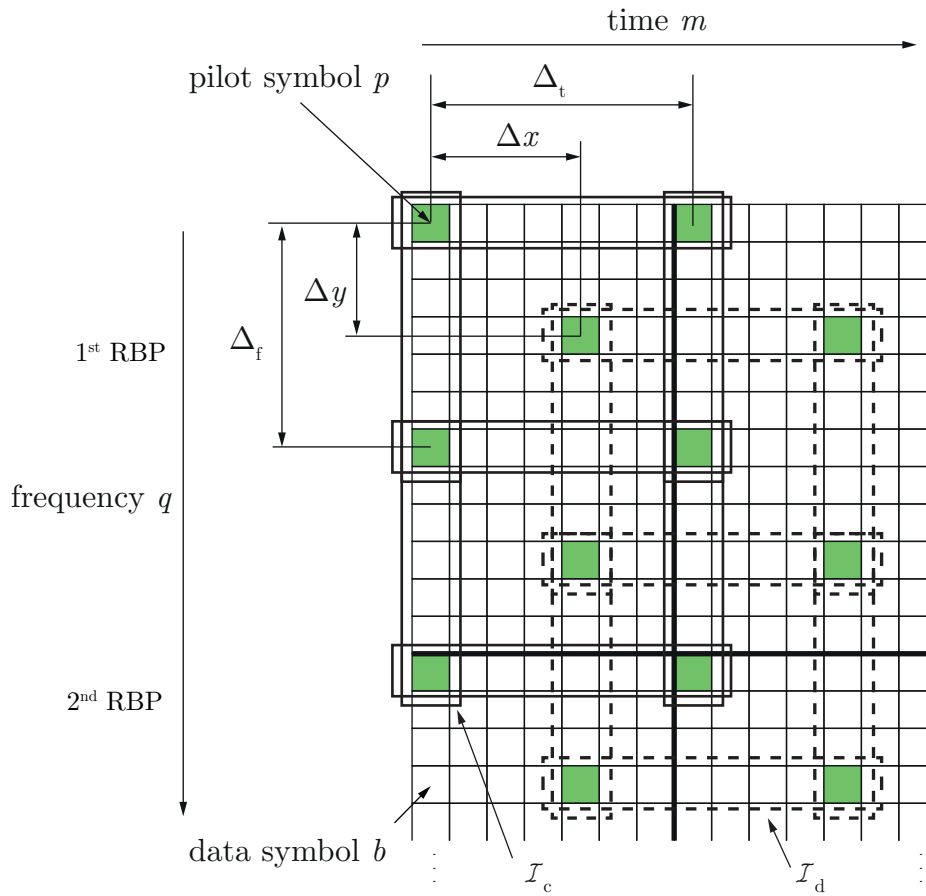


Figure 5.2: OFDM time-frequency grid of one LTE subframe with normal CP length and partitioned index sets  $\mathcal{I}_c$  and  $\mathcal{I}_d$

where  $\Delta_t = 7$  is the distance between the pilot symbols in time,  $k_t \in \{0, 1, \dots, 2N_{\text{SUBF}} - 1\}$ ,  $\Delta x = 4$  is the shift of  $\mathcal{I}_d^t$  against  $\mathcal{I}_c^t$  and  $N_{\text{SUBF}}$  is the number of considered subframes. The frequency index sets are defined by

$$I_c^f = \Delta_f k_f + 1 \quad \text{and} \quad I_d^f = I_c^f + \Delta y, \quad (5.31)$$

with  $\Delta_f = 6$  the distance between the pilot symbols in frequency direction,  $k_f \in \{0, 1, \dots, 2N_{\text{RBP}} - 1\}$ ,  $\Delta y = 3$  the shift of  $\mathcal{I}_d^f$  against  $\mathcal{I}_c^f$  and  $N_{\text{RBP}}$  the number of RBPs that depends on the bandwidth. Due to the definitions (5.30) and (5.31) the index sets  $\mathcal{I}_c^t(\mathcal{I}_d^t)$  and  $\mathcal{I}_c^f(\mathcal{I}_d^f)$  now contain equidistant elements in time and frequency direction, where  $\Delta_t$  and  $\Delta_f$  are the pilot distance in time and in frequency, respectively. We now define the two dimensional support region of the fading process  $\tilde{\mathbf{R}}_{\text{gp}}^{(\mathcal{I}_c)}$  on the index set  $\mathcal{I}_c$

$$\mathcal{W}_p = W_p^t \times W_p^f = [-\nu'_D, \nu'_D] \times [0, \theta'_P], \quad (5.32)$$

where we set  $\nu'_D = \Delta_t \nu_D$  and  $\theta'_P = \Delta_f \theta_P$ . Because of the equidistant structure of the index set the eigenvector matrices  $\mathbf{U}_p(W_p^t, I_c^t)$  and  $\mathbf{U}_p(W_p^f, I_c^f)$  can be obtained from generalized DPS sequences by using [97, Eq. (20)-(25)]. We then use (5.22) to obtain the eigenvector matrix of the index set

$$\mathbf{U}_p^{(\mathcal{I}_c)} = \Pi(\mathbf{U}_p(W_p^t, I_c^t) \diamond \mathbf{U}_p(W_p^f, I_c^f)). \quad (5.33)$$

Similarly, we obtain the diagonal eigenvalue matrix on the index set by

$$\Sigma_p^{(\mathcal{I}_c)} = \Pi(\text{diag}(\boldsymbol{\sigma}(W_p^t, I_c^t) \otimes \boldsymbol{\sigma}(W_p^f, I_c^f))). \quad (5.34)$$

Hence, the autocorrelation matrix can be calculated by

$$\tilde{\mathbf{R}}_{\mathbf{g}_p}^{(\mathcal{I}_c)} = \mathbf{U}_p^{(\mathcal{I}_c)} \Sigma_p^{(\mathcal{I}_c)} \mathbf{U}_p^{(\mathcal{I}_c)H}. \quad (5.35)$$

The dimension  $D_p^{(\mathcal{I}_c)}$  is obtained by (see (5.24))

$$D_p^{(\mathcal{I}_c)} = \underset{D_p^{(\mathcal{I}_c)} \in \{1, \dots, |\mathcal{I}_c|\}}{\text{argmin}} \left( \frac{1}{|\mathcal{W}_p| |\mathcal{I}_c|} \sum_{i=D_p}^{|\mathcal{I}_c|-1} \lambda_{p,i}(\mathcal{W}_p, \mathcal{I}_c) + \frac{D_p}{|\mathcal{I}_c|} \sigma_z^2 \right), \quad (5.36)$$

where  $\lambda_{p,i}(\mathcal{W}_p, \mathcal{I}_c)$  are the sorted eigenvalues of the fading process  $\tilde{\mathbf{R}}_{\mathbf{g}_p}^{(\mathcal{I}_c)}$  and  $|\mathcal{I}_c|$  is the cardinality of the index set  $\mathcal{I}_c$ . Obviously, the autocorrelation matrix of  $\mathcal{I}_d$  and  $\mathcal{I}_c$  are equal, since  $\mathcal{I}_d$  is only a shift of  $\mathcal{I}_c$  by  $(\Delta x, \Delta y)$ , i.e.,  $\mathbf{U}_p^{(\mathcal{I}_d)} = \mathbf{U}_p^{(\mathcal{I}_c)}$ . For brevity we will use  $\mathbf{U}_p = \mathbf{U}_p^{(\mathcal{I}_c)} = \mathbf{U}_p^{(\mathcal{I}_d)}$  for the next Sections.

### 5.4.2 Hypothesis Design

For the hypothesis test we define a finite set of  $A$  hypotheses for the DSD support [97]

$$W^t(a) = \left( -\frac{a}{A} \nu_{D\max}, \frac{a}{A} \nu_{D\max} \right), \quad (5.37)$$

with  $a \in \{1, \dots, A\}$ . Similarly, we define a finite set of  $A'$  hypotheses on the PDP support

$$W^f(a') = \left( 0, \frac{a'}{A'} \theta_{P\max} \right), \quad (5.38)$$

with  $a' \in \{1, \dots, A'\}$ . Each hypothesis represents a subspace spanned by the columns of  $\mathbf{U}(W^t(a), I^t)$  and  $\mathbf{U}(W^f(a'), I^f)$ . The subspaces correspond to the subspaces  $\mathbf{U}_p(W_p^t(a), I_c^t)$  and  $\mathbf{U}_p(W_p^f(a'), I_c^f)$  at the pilot symbols. These matrices can be pre-calculated and stored. The hypothesis test provides a hypothesis set combination  $(\hat{a}; \hat{a}') \in \{1, \dots, A; 1, \dots, A'\}$  for each frame that fits the normalized Doppler support  $\nu_D$  and normalized delay support  $\theta_P$  of the current channel realization best. This requires to test  $AA'$  different hypotheses. In the next Section we describe how the hypothesis test is performed and how the computational complexity can be reduced.

### 5.4.3 Hypothesis Test

To simplify the hypothesis test we utilize the same methodology as shown in [97, Eq. (43)-(48)] and test only  $A + A'$  hypothesis. We firstly assume that the PDP has maximum support  $W_p^f(A')$  and calculate the channel estimates on the pilot positions. We calculate the channel estimates for the index sets  $\mathcal{I}_c$  and  $\mathcal{I}_d$  for each of the  $A$  hypothesis for the DSD separately, according to

$$\hat{\mathbf{g}}_{p;a}^{(\mathcal{I}_c)} = \mathbf{U}_p(a, A') \mathbf{U}_p(a, A')^H \mathbf{w}_p^{(\mathcal{I}_c)}, \quad (5.39)$$

$$\hat{\mathbf{g}}_{p;a}^{(\mathcal{I}_d)} = \mathbf{U}_p(a, A') \mathbf{U}_p(a, A')^H \mathbf{w}_p^{(\mathcal{I}_d)}, \quad (5.40)$$

where  $\mathbf{w}^{(\mathcal{I}_c)}$  are the pilot symbols on the index set  $\mathcal{I}_c$  and where  $\mathbf{U}_p(a, A')$  is obtained according to (5.33). The data errors for hypothesis  $a$  can be expressed by [22, 97]

$$x_a^{(\mathcal{I}_c)} = \frac{1}{|\mathcal{I}_c|} \|\mathbf{w}_p^{(\mathcal{I}_c)} - \hat{\mathbf{g}}_{p;a}^{(\mathcal{I}_c)}\|^2, \quad (5.41)$$

$$x_a^{(\mathcal{I}_d)} = \frac{1}{|\mathcal{I}_d|} \|\mathbf{w}_p^{(\mathcal{I}_d)} - \hat{\mathbf{g}}_{p;a}^{(\mathcal{I}_d)}\|^2, \quad (5.42)$$

which are averaged, i.e.,

$$x_a = \frac{x_a^{(\mathcal{I}_c)} + x_a^{(\mathcal{I}_d)}}{2}. \quad (5.43)$$

The metric that we want to minimize is not the data error but the reconstruction error

$$z_a = \frac{1}{|\mathcal{I}_c|} \|\mathbf{g}_p - \hat{\mathbf{g}}_p(a)\|^2, \quad (5.44)$$

which cannot be directly observed at the receiver side since the the actual channel  $\mathbf{g}_p$  is not known to the receiver. Knowing  $x_a$ , we are interested to obtain a probabilistic upper bound on  $z_a$  as

$$z_a < \overline{z}_a(x_a, p_1, p_2) \quad (5.45)$$

that only depends on  $x_a$  and some constant  $p_1$  and  $p_2$ . This bounds enable us to select the best hypothesis  $W_p^t(\hat{a})$ , i.e.

$$\hat{a} = \operatorname{argmin}_{a \in \{1, \dots, A\}} \overline{z}_a(x_a, p_1, p_2) \quad (5.46)$$

which minimizes the reconstruction error. The detailed algorithm to calculate the bounds as well as how to choose  $p_1$  and  $p_2$  can be found in [97].

After we have obtained  $\hat{a}$  we proceed with the same procedure to test for the support of the PDP. For the support of the DSD we use  $W_p^t(\hat{a})$  and we test for  $a' \in \{1, \dots, A'\}$  with the matrix  $\mathbf{U}_p(\hat{a}, a')$ . Following (5.39)-(5.45) we obtain

$$\hat{a}' = \operatorname{argmin}_{a' \in \{1, \dots, A'\}} \overline{z}_{a'}(x_{a'}, p_1, p_2). \quad (5.47)$$

With the obtained hypotheses set  $(\hat{a}, \hat{a}')$  and with (5.20)-(5.23) we can calculate  $\tilde{\mathbf{R}}_{\mathbf{g}}$  for the Wiener filter in (5.7). Performing rank-reduction using (5.24) we can save substantial computational complexity.

In the next Section the performance of the hypothesis test is evaluated by numerical simulations.

## 5.5 Simulation Results

For the numerical simulations we employ a Rayleigh fading channel model with exponentially decaying PDP within the normalized delay support  $[0, \theta_{\text{P}}]$  and normalized RMS delay spread  $\theta_{\text{P}}/5$  [41, 97]. Time selective fading is calculated per channel tap according to a Clarke's model giving a normalized Doppler bandwidth  $\nu_{\text{D}}$ . For the system bandwidth we choose  $B = 1.4$  MHz which is equal to  $N_{\text{RBP}} = 6$  or  $N = 12N_{\text{RBP}} = 72$  data subcarriers. We simulate frames with  $N_{\text{SUBF}} = 1$  or 2 subframes and  $M = 14 \cdot N_{\text{SUBF}}$ . For the simulations we assume that the user occupies the whole available transmission bandwidth  $B$ . We set the carrier frequency to  $f_c = 2.6$  GHz and the FFT size to  $N' = 128$ . The OFDM symbol duration including CP is  $T_{\text{S}} \approx 71.4 \mu\text{s}$ . The maximum relative velocity between transmitter and receiver is  $v_{\text{max}} = 400$  km/h = 111.11 m/s and the maximum path delay is assumed with  $\tau_{\text{Pmax}} = 4.7 \mu\text{s}$ . For simplicity we assume that every OFDM symbol has the same CP length of  $4.7 \mu\text{s}$ . This results in a maximum normalized one sided Doppler bandwidth of  $\nu_{\text{Dmax}} = 0.0688$  and maximum normalized path delay  $\theta_{\text{Pmax}} = 0.0703$ .

To evaluate the performance of the time domain subspace selection algorithm, we generate a time-frequency selective fading process. We set the PDP support to  $\theta_{\text{P}} = \theta_{\text{Pmax}}$  and vary the Doppler bandwidth  $\nu_{\text{D}}$  within  $0 \leq \nu_{\text{D}} \leq \nu_{\text{Dmax}}$ . This relates to a velocity range  $v \in (0, 111.1) \text{ m/s} \approx (0, 400) \text{ km/h}$ . For the simulations we simulate 500 frames for each  $\nu_{\text{D}}$  value. Figure 5.3 depicts the channel estimation MSE on the pilot index set  $\mathcal{P}$  for different Doppler bandwidths  $\nu_{\text{D}}$  and fixed SNR  $\in \{0, 10\}$  dB. We show the MSE obtained by the adaptive subspace selection algorithm. Furthermore, we present the MSE if we use the subspace with maximum Doppler support and the MSE if we assume  $\nu_{\text{D}}$  and the corresponding subspace as perfectly known. The solid lines refer to the results obtained if the user is scheduled for only one subframe in time. The gain in MSE of the subspace selection compared to utilizing the subspace with maximum Doppler support is around 3 dB for low velocities and the performance of subspace selection follows closely the performance for known  $\nu_{\text{D}}$ . For higher SNRs we observe that the adaptive subspace selection algorithm quickly reaches the performance of using the subspace with fixed maximum support if we increase  $\nu_{\text{D}}$ . The reason is the too small number of observations in the time direction, which results in a too small granularity of the number of selectable

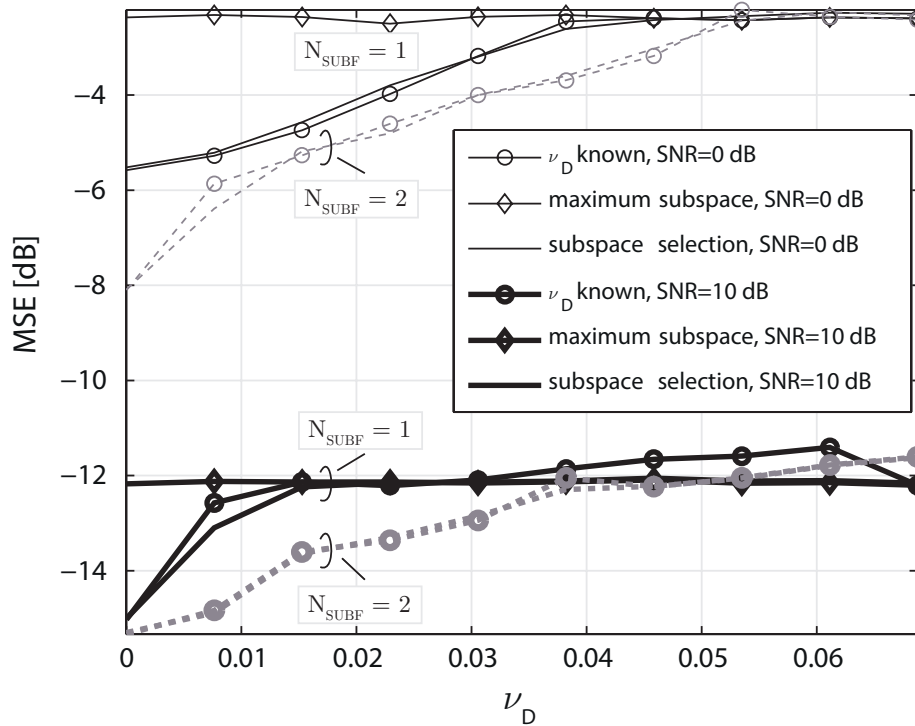


Figure 5.3: MSE vs. Doppler bandwidth  $\nu_D$  for  $\text{SNR} \in \{0, 10\}$  dB for adaptive subspace selection in the time domain with  $N_{\text{SUBF}} \in \{1, 2\}$

subspaces in time for the dimension selection in (5.24). The dotted lines in Fig. 5.3 show the simulation results if the user is scheduled for two consecutive subframes in time. Clearly, the adaptive subspace selection algorithm is able to gain over a wider range of the Doppler bandwidth compared to utilizing the subspace with maximum support, if more subframes can be observed.

The results in Fig. 5.4 present the MSE performance on the pilot positions  $\mathcal{P}$  of the adaptive subspace selection algorithm in the frequency domain. We set the DSD support to  $\nu_D = \nu_{D_{\text{max}}}$  and vary the PDP support range within  $0 \leq \theta_P \leq \theta_{P_{\text{max}}}$ . This relates to a maximum excess delay of  $\tau_P \in (0, 4.7) \mu\text{s}$ . We assume that the user occupies the whole system bandwidth which means all pilot symbols are available for the subspace selection algorithm. The figure presents the MSE that is obtained with adaptive subspace selection, the MSE if the subspace with maximum delay support is used and the MSE if  $\theta_P$  is perfectly known. For small normalized delays  $\theta_P$  the selection algorithm is able to gain up to 7 dB compared to utilizing the subspace with fixed maximum delay support.

Finally, Fig. 5.5 shows the PER versus the number of iterations for a fixed  $\text{SNR} = 13$  dB. We utilize a 16-QAM symbol alphabet and a coding rate of  $R = 0.479$ . We

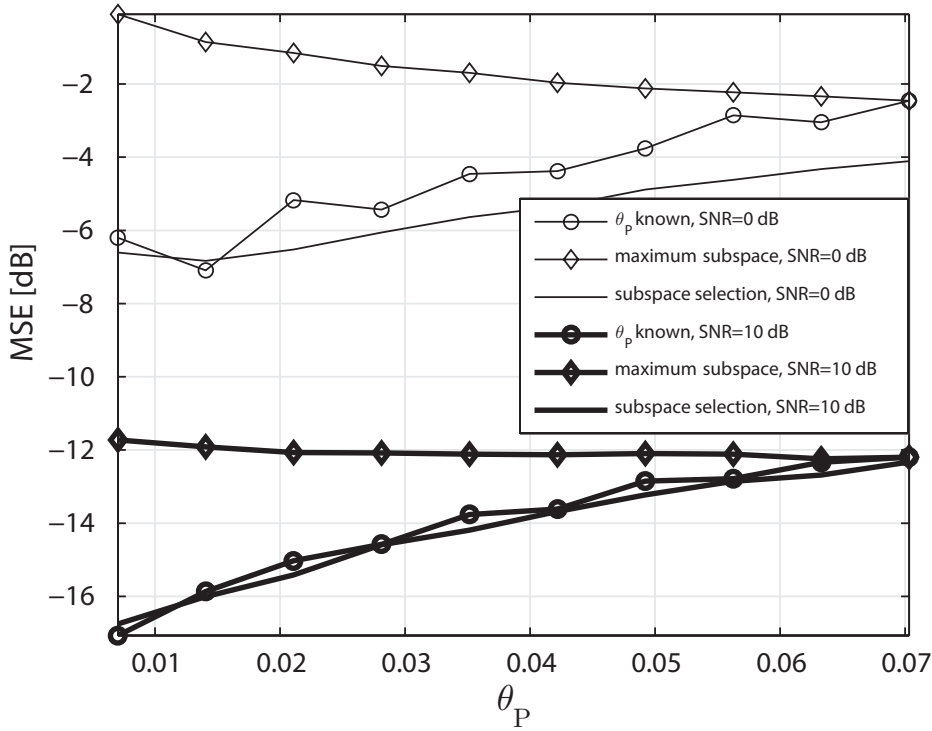


Figure 5.4: MSE vs. normalized PDP support  $\theta_P$  for  $\text{SNR} \in \{0, 10\}$  dB for adaptive subspace selection in the frequency domain

compare the PER obtained by adaptive subspace selection with the PER obtained for the fixed maximum subspace for relative velocities  $v \in \{50, 200, 400\}$  km/h. For the simulations we assume that the user is scheduled for two consecutive subframes and uses the whole system bandwidth  $B$ . We simulate 1000 frames. The results show that with the adaptive subspace selection algorithm the number of iterations required to achieve a certain PER can be reduced. For a velocity of  $\{50, 200, 400\}$  km/h we need  $\{-, 2, 2\}$  iterations to obtain a PER lower than  $10^{-1}$ . The symbol ‘-’ means that the target PER cannot be achieved for the corresponding velocity. For a fixed subspace  $\{-, 4, 3\}$  iterations are required.

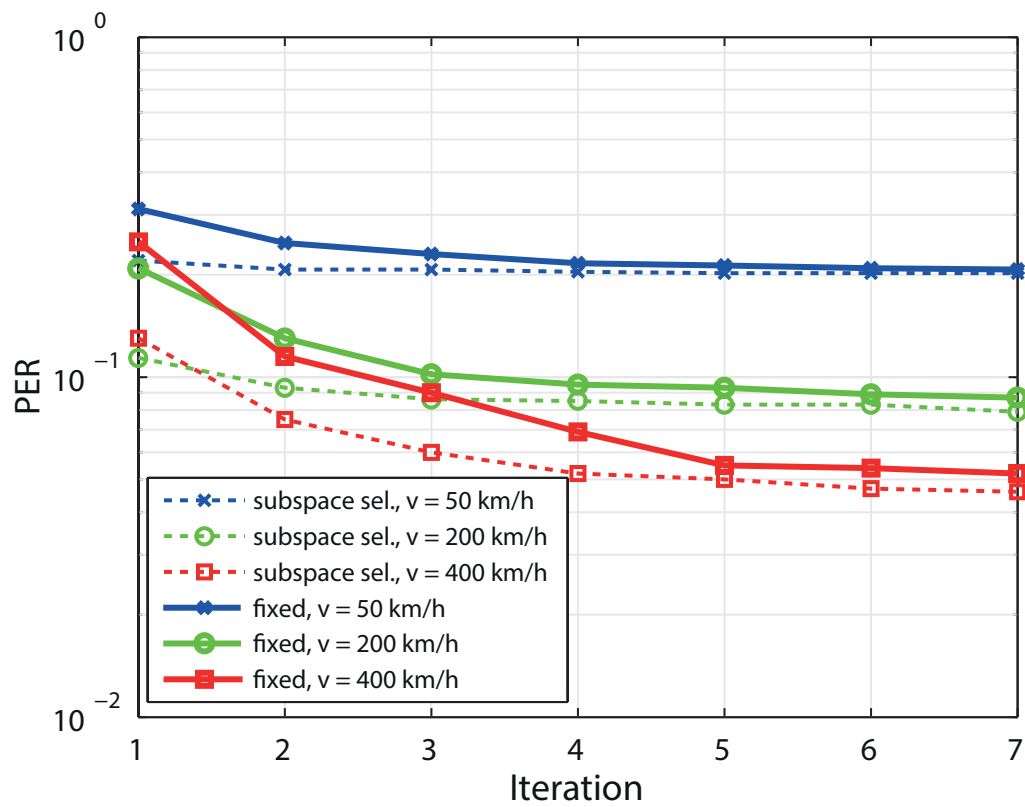


Figure 5.5: PER vs. number of iterations for SNR = 13 dB and relative velocities  $v \in \{50, 200, 400\}$  km/h;  $R = 0.479$ , 16-QAM symbol alphabet

## 5.6 Determining the Optimum Number of Hypotheses

The optimum number of hypotheses for the hypothesis test described in the previous section is not known. In this section we determine the optimum number of hypotheses numerically [22]. For the optimization we consider a frequency flat channel, i.e., a single subcarrier of the OFDM grid. Furthermore, we show a hypothesis design that allows for a good trade-off between performance and computational complexity. In the next section we re-introduce the system model for a single subcarrier.

### 5.6.1 System Model for a Frequency Flat Channel

We consider the transmission of a symbol sequence  $d[m]$  of length  $M$  over a time-variant frequency-flat fading channel  $h[m]$ . The received signal sequence  $y[m]$  can be modeled by

$$y[m] = d[m]h[m] + z[m], \quad (5.48)$$

with  $m \in \{0, \dots, M-1\}$  where  $z[m] \sim \mathcal{CN}(0, \sigma_z^2)$  is the symmetric complex additive white Gaussian noise with zero mean and variance  $\sigma_z^2$ , respectively. The symbol sequence  $d[m]$  consists of  $M - N_p$  data symbols  $b[m]$  interleaved with  $N_p$  pilot symbols  $p[m]$

$$d[m] = b[m] + p[m]. \quad (5.49)$$

The data and pilot symbols are drawn from a QPSK symbol alphabet and  $b[m] = 0$  for  $m \in \mathcal{P}$ . We assume that the pilot placement is defined by the index set

$$\mathcal{P} = \{\Delta_t k_t : k_t \in \{0, 1, \dots, N_p - 1\}\}, \quad (5.50)$$

where  $\Delta_t$  represents the pilot symbol distance. Defining the length  $M$  received column vector  $\mathbf{y} = [y[0], y[1], \dots, y[M-1]]^T \in \mathbb{C}^{M \times 1}$  we can rewrite (5.48) in matrix-vector form according to

$$\mathbf{y} = \mathbf{D}\mathbf{h} + \mathbf{z}. \quad (5.51)$$

The length  $M$  vectors  $\mathbf{d} \in \mathbb{C}^{M \times 1}$ ,  $\mathbf{h} \in \mathbb{C}^{M \times 1}$ , and  $\mathbf{z} \in \mathbb{C}^{M \times 1}$  are defined similarly to  $\mathbf{y}$  and contain the transmitted symbols, the channel coefficients and the noise samples, respectively. The matrix  $\mathbf{D} = \text{diag}(\mathbf{d})$  is a diagonal matrix of size  $M \times M$  with the elements of  $\mathbf{d}$  on its diagonal.

To estimate the unknown channel vector  $\mathbf{h}$  we use an LMMSE estimator

$$\hat{\mathbf{h}}_{\text{LMMSE}} = \mathbf{R}_{\mathbf{h}, \mathbf{h}_p} \mathbf{D}_p^H (\mathbf{D}_p \mathbf{R}_{\mathbf{h}_p} \mathbf{D}_p^H + \sigma_z^2 \mathbf{I}_{N_p})^{-1} \mathbf{y}_p \quad (5.52)$$

that provides the channel estimate  $\hat{\mathbf{h}}_{\text{LMMSE}}$ . Here  $\mathbf{I}_{N_p}$  represents the identity matrix of size  $N_p \times N_p$  and  $(\cdot)^H$  denotes the conjugate transpose. The vectors  $\mathbf{y}_p \in \mathbb{C}^{N_p \times 1}$ ,

$\mathbf{h}_p \in \mathbb{C}^{N_p \times 1}$ , and  $\mathbf{z}_p \in \mathbb{C}^{N_p \times 1}$  contain the noisy observations, the channel, and the noise samples, respectively, at pilot positions only. The elements of the vectors are given by  $y_p[k] = y[\Delta_t k_t]$ ,  $h_p[k] = h[\Delta_t k_t]$ , and  $z_p[k] = z[\Delta_t k_t]$  for  $k_t = 0, \dots, N_p - 1$ , respectively. The matrix  $\mathbf{D}_p = \text{diag}(\mathbf{d}_p)$  is of size  $N_p \times N_p$  and  $\mathbf{d}_p \in \mathbb{C}^{N_p \times 1}$  is the vector of pilot symbols. Furthermore,  $\mathbf{R}_{\mathbf{h}_p} = \mathbb{E} \{ \mathbf{h}_p \mathbf{h}_p^H \}$  is the autocorrelation matrix of the channel at pilot positions and  $\mathbf{R}_{\mathbf{h}, \mathbf{h}_p} = \mathbb{E} \{ \mathbf{h} \mathbf{h}_p^H \}$  is the cross correlation matrix between the channel at all positions and the channel at pilot positions. They can be obtained as sub-matrices of the channel autocorrelation matrix  $\mathbf{R}_{\mathbf{h}} = \mathbb{E} \{ \mathbf{h} \mathbf{h}^H \}$  by extracting  $\Delta_t$ -spaced rows and/or columns. See [127] for further details.

For the hypothesis test we use the same methodology as explained in Section 5.4. We define the observations on pilot symbols for the frequency flat channel like in (5.25). We consider only a one dimensional test, i.e., a hypothesis test to find the support of the DSD. The obtained hypothesis  $\hat{a}$  is used to obtain the estimated channel  $\hat{\mathbf{h}}_{\text{LMMSE}}^{\hat{a}}$ . A more detailed description is shown in Appendix A and in [22].

## 5.6.2 Numerical Optimization of the Number of Hypotheses

The optimum number of hypotheses  $A_{\text{opt}}$  is not known. We present a framework to determine  $A_{\text{opt}}$  by numerical optimization. As optimization criterion we use the mean square channel estimation error (MSE). For the optimization process we vary the number of hypotheses  $A_i \in \{1, \dots, A_{\text{max}}\}$  and determine the number of hypotheses  $A_{\text{opt}}$  that provides the minimum overall MSE. The variable  $A_{\text{max}}$  denotes the maximum number of hypotheses to be tested against and will be defined in Section 5.6.4.

For each  $A_i \in \{1, \dots, A_{\text{max}}\}$  we define  $A_i$  hypotheses according to Eq. (A.4) and simulate  $F$  frames of length  $M$ . For every frame  $f \in \{1, \dots, F\}$  the normalized one-sided Doppler support  $\nu_D^f$  of the current channel realization is drawn randomly from the uniform distribution  $\mathcal{U}[0, \nu_{D\text{max}}]$ , i.e.,  $\nu_D^f \sim \mathcal{U}[0, \nu_{D\text{max}}]$ . The hypothesis test provides a hypothesis  $\hat{a}_{A_i}^f \in \{1, \dots, A_i\}$  that is used to calculate  $\tilde{\mathbf{R}}_{\mathbf{h}}^{\hat{a}_{A_i}^f}$  of the current channel realization. With (A.10) we obtain  $\hat{\mathbf{h}}_{\text{LMMSE}}^{\hat{a}_{A_i}^f}$ . The MSE of one frame  $f$  is calculated by

$$\text{MSE}_{A_i}^f = \frac{1}{M} \left\| \mathbf{h}^f - \hat{\mathbf{h}}_{\text{LMMSE}}^{\hat{a}_{A_i}^f} \right\|^2, \quad (5.53)$$

where  $\mathbf{h}^f$  denotes the current channel realization for frame  $f$ .

For the evaluation of the overall MSE performance we calculate the average MSE over all frames  $F$  for each hypothesis size  $A_i$  by

$$\overline{\text{MSE}}_{A_i} = \frac{1}{F} \sum_{f=1}^F \text{MSE}_{A_i}^f. \quad (5.54)$$

The optimum number of hypotheses  $A_{\text{opt}}$  is the number of hypotheses that minimizes  $\overline{\text{MSE}}_{A_i}$ , i.e.,

$$A_{\text{opt}} = \underset{A_i \in \{1, \dots, A_{\text{max}}\}}{\text{argmin}} \overline{\text{MSE}}_{A_i}. \quad (5.55)$$

To assess the performance of the adaptive subspace selection algorithm for different Doppler bandwidths we introduce a second evaluation method. The frames are grouped into  $B$  equidistant bins. Each bin  $b \in \{1, \dots, B\}$  corresponds to a Doppler support  $W_t(b) = (-\frac{b}{B}\nu_{\text{Dmax}}, \frac{b}{B}\nu_{\text{Dmax}})$ . For a channel realization  $f$  to belong to the bin  $b$  the Doppler support  $\nu_{\text{D}}^f$  must fulfill  $\frac{(b-1)}{B}\nu_{\text{Dmax}} < \nu_{\text{D}}^f \leq \frac{b}{B}\nu_{\text{Dmax}}$ . The average MSE of a bin  $b$  is then calculated by

$$\overline{\text{MSE}}_b = \frac{1}{F_b} \sum_{f=1}^{F_b} \text{MSE}_b^f, \quad (5.56)$$

where  $F_b$  is the number of frames belonging to bin  $b$  and  $\text{MSE}_b^f$  is the MSE of the  $f$ -th frame that belongs to bin  $b$ .

### 5.6.3 Specifically Chosen Hypotheses Setup

Besides optimizing the number of hypotheses, we also tested the performance of specifically chosen hypotheses setups. Both hypotheses setups depend on the eigenvalue distribution of the autocorrelation process  $\tilde{\mathbf{R}}_{\text{hp}}$ . For the setup we divide  $\nu_{\text{Dmax}}$  into  $A_{\text{th}} = 400$  hypotheses and calculate for each hypothesis the dimension  $D_{a_{\text{th}}}^{(\mathcal{P})}$ ,  $a_{\text{th}} \in \{1, \dots, A_{\text{th}}\}$  according to (A.3). Depending on the eigenvalue distribution of the current hypothesis, different hypotheses may have the same dimension, i.e.,  $D_i^{(\mathcal{P})} = D_j^{(\mathcal{P})}$ ,  $i \neq j$ ,  $i, j \in \{1, \dots, A_{\text{th}}\}$ . Hypotheses with the same dimensions are grouped. For the hypotheses set of 'Dim. max' we take the hypothesis with maximum support within a group of the same dimension. For the hypothesis setup 'Dim. mid' the Doppler support of the hypotheses is set to the middle of the support of the hypotheses of 'Dim. max'. A graphical representation of this setup is shown in Fig. 5.6.

### 5.6.4 Simulation Results

For the simulations we consider Monte Carlo (MC) simulations with  $F = 10000$  frames for each hypothesis size  $A_i$ . The time-variant flat-fading channel is assumed to have a DSD with flat support. The maximum relative velocity between transmitter and receiver is  $v_{\text{max}} = 200$  km/h.

For the carrier frequency and the symbol duration we assume parameters similar to the LTE downlink. We set the carrier frequency  $f_c = 2.6$  GHz and the symbol

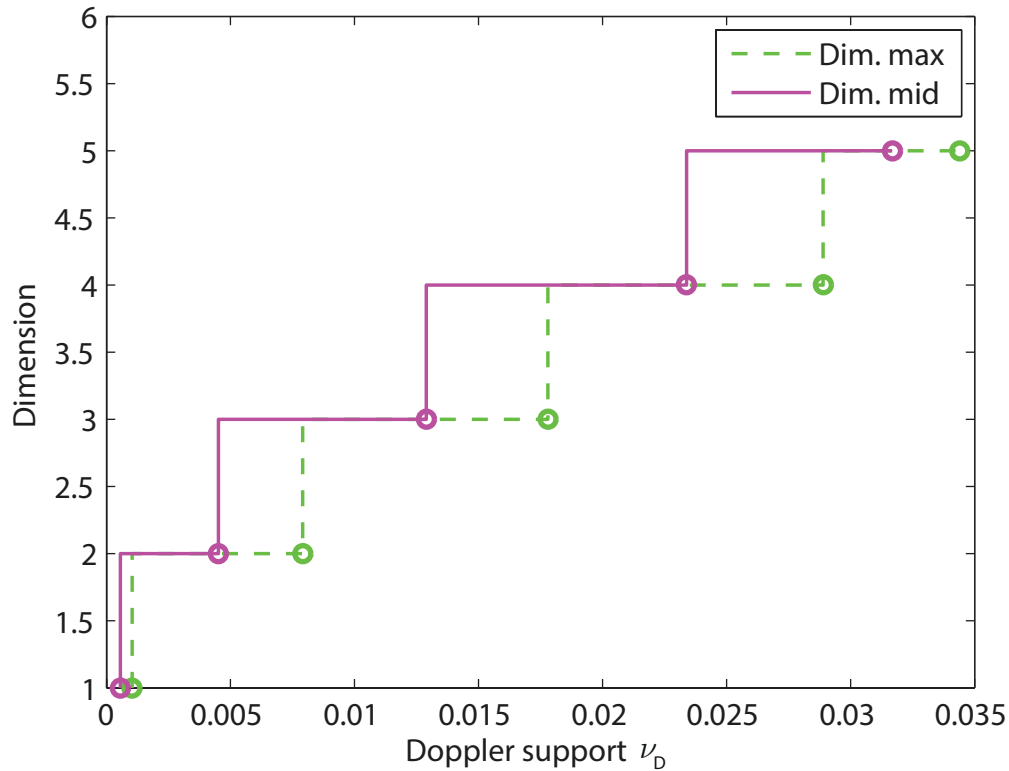


Figure 5.6: One sided normalized Doppler support and dimension for the hypothesis setup 'Dim. max' (green) and 'Dim. mid' (magenta);  $\Delta_t = 1$ ,  $M = 42$ ,  $v_{\max} = 200$  km/h, SNR = 10 dB

duration  $T_S = 71.43 \mu\text{s}$ . We simulate frames with  $M = 42$  symbols per frame which corresponds to three LTE consecutive subframes. This leads to  $\nu_{D_{\max}} = 0.0344$  and a time-bandwidth product (TBWP)  $M\nu_{D_{\max}} = 1.444$ . The SNR was set to 10 dB. To gain an intuitive insight on the optimal number of hypotheses the pilot distance is set to  $\Delta_t = 1$ , i.e., only pilot symbols are transmitted. This pilot pattern is e.g. relevant in the case of iterative channel estimation explained in Section 5.3 where after one iteration the fed back soft data symbols are utilized as pilot symbols for channel estimation, or for the pilot subcarriers in 802.11p. The maximum number of hypotheses tested is  $A_{\max} = 100$  and the number of bins is set to  $B = 20$  which corresponds to a bin size of 10 km/h.

In Fig. 5.7 we plot the overall average  $\overline{\text{MSE}}_{A_i}$  dependent on the hypothesis size  $A_i$ . We observe that the MSE has a minimum for a hypothesis size of 10. The minimum corresponds to the optimum number of hypotheses  $A_{\text{opt}}$ . A lower number  $A_i < A_{\text{opt}}$  leads to performance degradation, whereas a higher number  $A_i > A_{\text{opt}}$  leads to a

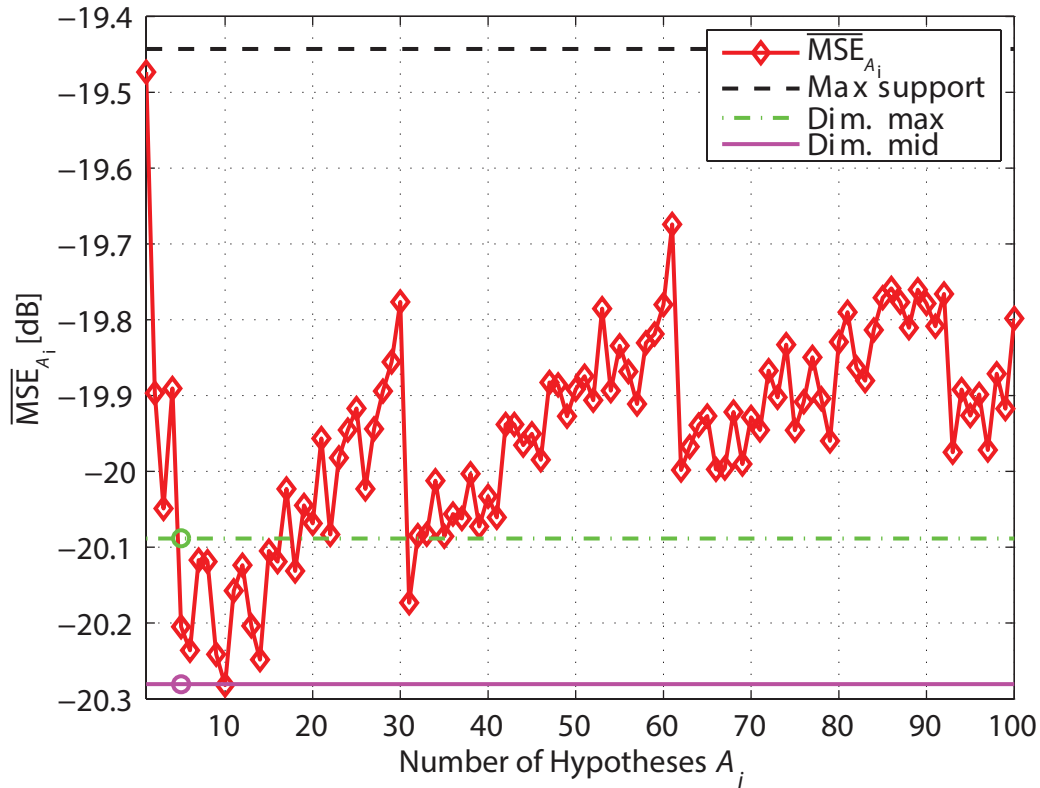


Figure 5.7:  $\overline{\text{MSE}}_{A_i}$  vs. hypothesis size  $A_i$  for a time-variant frequency-flat channel;  $\Delta_t = 1$ ,  $M = 42$ ,  $v_{\max} = 200$  km/h,  $\text{SNR} = 10$  dB

performance degradation and an increase of the computational complexity of the receiver. This is an important insight for the design of adaptive receiver structures of this kind to save complexity. The zigzag behavior of the curve is a result of the hypotheses design and of the properties of the hypothesis test.

The performance of the specifically chosen hypotheses setup are presented schematically by horizontal lines in Fig. 5.7. The number of utilized hypotheses is marked by circles of the corresponding color. For the setup 'Max support' (black line) we only consider one hypothesis with maximum Doppler support  $\nu_{\text{Dmax}}$ . Obviously, as already discussed in previous sections, assuming only the maximum Doppler support for channel estimation leads to a suboptimal estimation performance. From Fig. 5.7 we see that 'Dim. mid' (magenta line) obtains good performance results. For a pilot spacing of  $\Delta_t = 1$  it performs similar to the optimum number of hypotheses. The performance of 'Dim. mid' depends on  $\Delta_t$ , the TBWP and SNR. The setup does not always perform better than the optimum number of hypotheses, however, simulations show that it obtains good performance for different TBWP. Consider-

ing Fig. 5.6, we observe that the number of required hypotheses is only 5 which is less than  $A_{\text{opt}}$ . Thus the hypothesis setup 'Dim. mid' provides a good trade-off between estimation performance and complexity. For the setup only the parameters  $\nu_{\text{Dmax}}$ ,  $M$  and the SNR are required. Finally, we observe that the setup 'Dim. max' (green curve) with the same number of hypotheses as 'Dim. mid' results in a worse performance compared to 'Dim. mid'.

In Fig. 5.8 we show  $\overline{\text{MSE}}_b$  versus the normalized one sided Doppler bandwidth  $\nu_{\text{D}}$  for different hypothesis setups. We observe that the setup 'Dim. mid' performs similar to the setup with the optimum number of hypotheses. For small  $\nu_{\text{D}}$  adaptive subspace selection gains up to 4 dB compared to a hypothesis setup that only assumes  $\nu_{\text{Dmax}}$ . This results are similar to [32]. The gain decreases with increasing  $\nu_{\text{D}}$ . For larger Doppler bandwidths a performance loss compared to the maximum support can be observed. This performance loss originates from the hypothesis design for 'Dim. mid'. The last hypothesis of 'Dim. mid' is not designed for the maximum Doppler support. If channel realizations with a higher Doppler support are estimated with DPS sequences designed for a lower Doppler support, a performance degradation occurs, which can be seen in the figure. For performance comparison the Wiener filter (WF) bound with exact knowledge of  $\mathbf{R}_{\mathbf{h}}$  is shown, which can be calculated according to [127, Eq. (6)-(7)].

Finally, Fig. 5.9 shows  $\overline{\text{MSE}}_b$  versus  $A_i$  for different bins  $b$ . We observe that bins that correspond to lower speeds obtain a large performance gain when the number of hypotheses is increased. On the other hand, bins that correspond to higher speeds obtain a performance loss. Furthermore we see that depending on the bin the performance does not change significantly after passing a certain hypothesis size. This also underlines that increasing the number of hypotheses does not necessarily provide a better estimation performance.

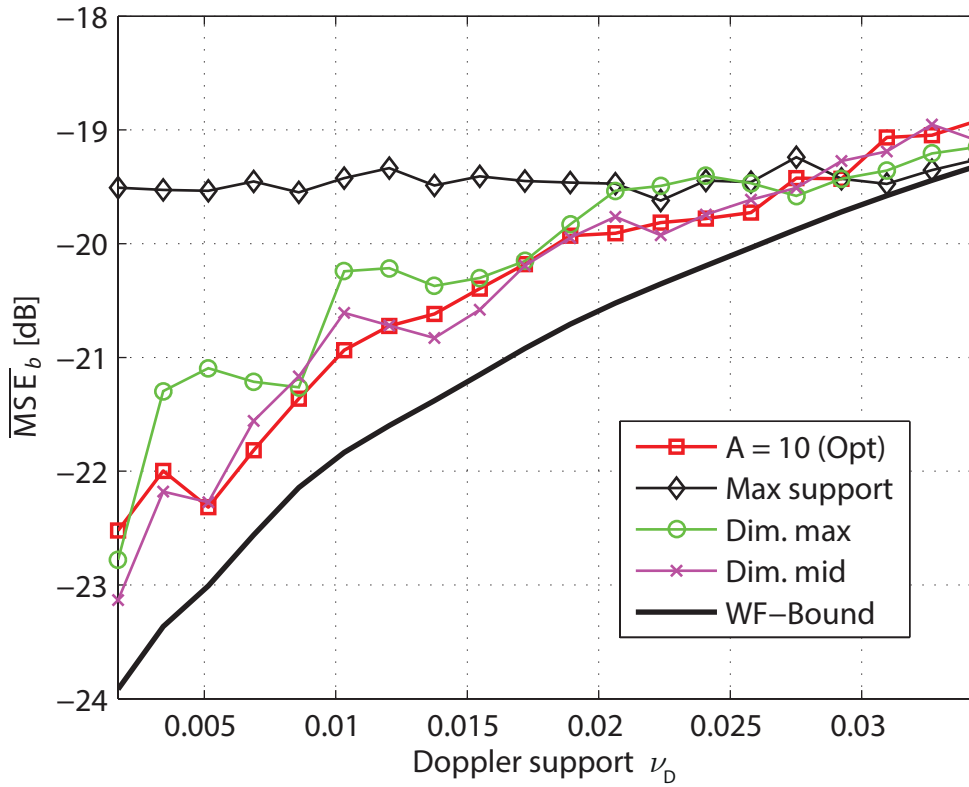


Figure 5.8:  $\overline{\text{MSE}}_b$  vs.  $\nu_D$ ;  $\Delta_t = 1$ ,  $M = 42$ ,  $v_{\max} = 200$  km/h, SNR = 10 dB

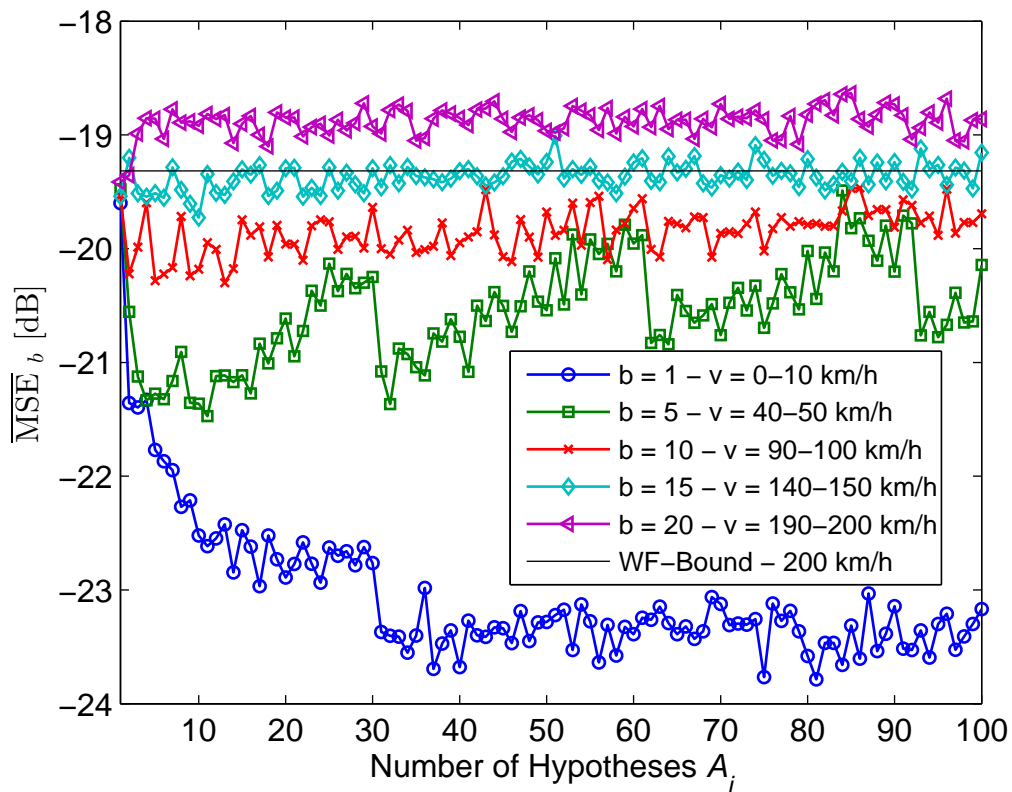


Figure 5.9:  $\overline{\text{MSE}}_b$  vs.  $A_i$ ;  $\Delta_t = 1$ ,  $M = 42$ ,  $v_{\max} = 200$  km/h, SNR = 10 dB

# 6 Conclusion

## 6.1 Summary

URLLC will play an essential role for time-sensitive applications for different vertical industries such as connected autonomous vehicles, industrial automation, smart grids, tactile internet and more. As a challenging research field, URLLC requires advancements in different technological areas. In this thesis two areas that enable the development of URLLC were investigated.

In the first part of the thesis, real-time wireless geometry-based channel emulation was presented. It allows for the repeatable and reproducible test of communication devices with realistic wireless communication channels in a laboratory environment. Wireless communication channels exhibit time- and frequency selective, non-stationary channel characteristics that depend on the position, velocity and on the environment of the communication devices. This includes the *continuous* change of path delay and Doppler shift dependent on the position and velocity of the communication devices. State of the art channel emulators cannot emulate such wireless propagation channels due to the underlying TDL model that only allows delays to be integer multiples of the sampling time. Geometry-based channel models use a path based modeling approach and can inherently model continuously changing path delays and Doppler shifts and the non-stationary properties of the channels. The high computational complexity of geometry-based channel models makes a direct implementation on FPGAs or DSPs difficult. To circumvent this problem, a channel emulation architecture that consists of a multi-core computer in connection with a SDR was shown. On the multi-core computer the geometry-based channel model is updated in real-time dependent on the positions, velocities and acceleration of the moving objects, while the SDR is used to perform the time-variant convolution of the CIR with the transmitted signal. The data rate of the CIR grows quadratic with the emulated bandwidth and becomes quickly a bottleneck, if the time-variant CIR has to be streamed between devices. To reduce the data rate of the CIR, a subspace projection algorithm based on DPS sequences to approximate the CIR with a small amount of basis coefficients is utilized. The basis coefficients can efficiently be obtained using a table look-up which allows for a real-time implementation of the algorithm. These basis coefficients are transmitted to the FPGA and utilized by a

basis expansion module to reconstruct the CIR. The computational complexity of the table look-up grows linearly with the number propagation paths, while the computational complexity of reconstructing the CIR on the FPGA is *independent* of the number of propagation paths. A comprehensive error analysis of the approximation was also provided.

To validate the channel emulator, the CIR was measured using the RUSK Lund channel sounder and compared with numerical simulations. As metric the second order moments, PDP and DSD, as well as the RMS delay spread and the RMS Doppler spread were utilized. To validate the fundamental capability of emulating continuously changing delays a single propagation path with changing Doppler shift was emulated. The measurement results showed an error of -35 dB between numerical simulation and emulation, which can be explained by thermal noise. Furthermore, a GSCM of a road-intersection scenario with more than 600 propagation paths was emulated and compared with numerical simulations and measurements of a measurement campaign in 2007. The results showed that the real-time geometry based channel emulator can emulate non-stationary channels with a large amount of propagation paths. Furthermore, the utilized GSCM can capture the statistics, especially the RMS delay- and RMS Doppler-spread of the considered road intersection. Finally, the backward compatibility of the emulator to emulate simple scenarios was shown by emulating ETSI ITS-G5 channel models.

The channel emulator was utilized to validate ViL tests for wireless communications. As scenario a left turn on a proving ground in Germany was considered. For validation, the PER and the RSSI of the measurement on the proving ground was compared with the PER and the RSSI of the measurement of the ViL test. The wireless communication channel for the ViL test was generated by the real-time geometry based channel emulator that was parameterized by a GSCM of an urban road-intersection. The GSCM was adapted to the road intersection scenario of the proving ground. Road signs, vegetation as well as moving objects were modeled. The position, velocity and acceleration were updated in real-time by virtual test drive. The results showed a good qualitative match of PER and RSSI. For an even closer match the large-scale fading as well path loss have to be calibrated.

To enable low latency links between transmitter and receiver, channel estimation algorithms have to be able to adapt to the current channel properties. In the second part of the thesis adaptive iterative channel estimation for non-stationary channels was investigated. A hypothesis test was utilized to adapt to the channel statistics of the current channel realization. The advanced channel estimation technique allows low latency communication links since, e.g., the number of iterations of the iterative channel estimator can be reduced and due to the better estimation performance retransmissions can be avoided. It was shown how to separate the non-contiguous pilot grid of LTE downlink to a contiguous, equidistant pilot grid. The

autocorrelation matrix of the contiguous, equidistant grid can be described by DPS sequences that are set up with a larger Doppler support. Using numerical simulation the performance of the hypothesis test was investigated. It was observed that compared to no subspace selection a gain of the MSE performance can be achieved. The results indicated that the longer the observation period, the higher the gain in MSE performance. Furthermore, the number of hypotheses for the hypothesis test was optimized numerically. Finally, a method of how to design the hypotheses that allows for a good trade-off between performance and computational complexity was presented and evaluated numerically.

## 6.2 Key Findings

In the following, the key findings of the thesis are summarized

### Wireless Channel Emulation

- The concept of geometry-based channel emulation was introduced replacing the TDL as basic building block for channel emulation. The emulator consists of a propagation module that is implemented on a general purpose multi-core PC and a convolution module that is implemented on an SDR equipped with an FPGA. The GSCM concept was extended by adding visibility conditions and diffraction at corners of larger objects as well as the effect of vegetation to obtain a real-time channel model, providing the path parameters for the geometry-based channel emulator.
- The partition of the non-stationary fading process in a sequence of local stationarity regions with a continuous phase transition at the boundaries of the stationarity regions was illustrated. Each local stationarity region is fully described by a set of propagation paths with given attenuation, delay and Doppler shift. Within the stationarity region a constant Doppler shift and correspondingly a linear increase of the delay is assumed.
- The utilization of a reduced-rank basis expansion model based on DPS sequences to approximate the GSCM was shown. The basis coefficients can be efficiently calculated by a table lookup in  $\mathcal{O}(1)$  which enables a real-time implementation of the GSCM. With the utilized model the computational complexity on the FPGA becomes independent of the number of propagation path.
- A comprehensive error analysis of the approximated GSCM was presented. This can be utilized for the parameterization of the channel emulator if, e.g., other bandwidths are required.

- Finally, the real-time emulator was utilized to emulate a V2X communication channel of a left turn scenario in a ViL test. A GSCM was utilized to model the communication channel, where for the first time the propagation properties were updated in real-time dependent on the position, velocity and acceleration obtained from the environment simulation of Virtual Test Drive. The GSCM was adapted from a GSCM developed for a road intersection scenario, where the effect of vegetation was modeled by diffuse scatterers. For the validation the PER and RSSI of the test on the proving ground were recorded and compared with the PER and RSSI of the ViL simulation. A quantitative match of the measurement results of the proving ground and the ViL test was observed. A further key finding was, that for a closer match between measurement on the proving ground and ViL test, the parameterization of the utilized GSCM for this scenario, especially the large-scale fading and the path loss coefficients, has to be calibrated by measurement data.

### Iterative Channel Estimation

- In this section it was shown how to apply an adaptive iterative channel estimation technique developed for a contiguous pilot pattern to a non-contiguous, equidistant pilot pattern. The auto-correlation matrix on the pilot grid can be obtained from modified DPS sequences. A hypothesis test was utilized to obtain the delay and Doppler support of the current channel realization on a per frame basis.
- A numerical optimization of the number of hypotheses for the hypothesis test was provided. An optimum number of hypotheses that provides the smallest channel estimation MSE was found.
- Finally, a simplified hypothesis setup was provided, that offers a good trade-off between MSE performance and computational complexity. For the setup only the maximum TBWP of the setup and the SNR are required.

### 6.3 Outlook

The developed concepts of this thesis build a starting point for further future developments.

A natural step forward is the extension to MIMO channel emulation. For MIMO emulation the GSCM can straight forwardly be extended by the position as well as the antenna pattern of the other considered TXs and RXs. For real-time emulation, either each channel is emulated separately, or the utilization of multi dimensional

DPS sequences can be considered [92]. For a correct emulation it has to be ensured that the starting point of the emulation of the different channels is synchronized. Furthermore, the phases of the different MIMO RF chains of the emulator have to be calibrated against each other, to ensure that the phase relations between channels can be emulated correctly.

Another step forward is multi node channel emulation that is required for developing and testing of, e.g., relaying applications in a laboratory environment. Considering as an example a relaying scenario with TX, RX and one relay node, in the first time slot the channel between TX and RX and TX and relay is emulated, while in the second time slot the channel between relay and RX is emulated. Similar to the MIMO emulation case the start point of emulation and the phases of the different RF chains have to be calibrated.

Furthermore, the extension to higher bandwidths and higher carrier frequencies (mmWave) for testing future communication technologies is a viable step forward. Finally, the emulation of radar targets is a possible future research field. For radar emulation extremely fast digital components like ADCs and DACs are required, that allow the emulation of targets with small distances.

## 6 Conclusion

---

# A Hypothesis Test for the Frequency Flat Channel

The signal model at pilot positions is given by

$$\mathbf{y}_p = \mathbf{D}_p \mathbf{h}_p + \mathbf{z}_p. \quad (\text{A.1})$$

The channel observations at the pilot positions  $\mathcal{P}$  are obtained by

$$\mathbf{w}_p = \mathbf{D}_p^H \mathbf{y}_p = \mathbf{h}_p + \mathbf{D}_p^H \mathbf{z}_p = \mathbf{h}_p + \mathbf{z}'_p, \quad (\text{A.2})$$

where  $\mathbf{z}'_p \sim \mathcal{CN}(0, \sigma_z^2 \mathbf{I}_{N_p})$  has the same statistics as  $\mathbf{z}_p$ . The fading process observed at the pilot positions is described by the eigenvectors of the autocorrelation matrix  $\mathbf{R}_{\mathbf{h}_p}$ . For an equidistant pilot grid the eigenvectors  $\mathbf{U}_p(W_t, \mathcal{P})$  of a fading process  $\tilde{\mathbf{R}}_{\mathbf{h}_p}$  that assumes a flat DSD are also spanned by sampled DPS sequences [21]. For the setup of  $\mathbf{U}^{(\mathcal{P})}$  we use [32, Eq. (20)-(25)] and set  $\nu'_D = \Delta_t \nu_D$  [21]. From this setup we obtain  $\Sigma^{(\mathcal{P})}$ . To determine the dimension  $D_p$  we use a slight variation of (5.24)

$$D^{(\mathcal{P})} = \underset{\mathcal{D}^{(\mathcal{P})} \in \{1, \dots, N_p\}}{\operatorname{argmin}} \left( \frac{1}{N_p} \sum_{i=\mathcal{D}^{(\mathcal{P})}}^{N_p-1} \lambda_i^{(\mathcal{P})}(W_t, \mathcal{P}) + \frac{\mathcal{D}^{(\mathcal{P})}}{N_p} \sigma_z^2 \right), \quad (\text{A.3})$$

where  $\lambda_i^{(\mathcal{P})}(W_t, \mathcal{P})$  are the eigenvalues of the fading process  $\tilde{\mathbf{R}}_{\mathbf{h}_p}$ .

For the hypothesis test we define a finite set of  $A$  hypotheses  $\{W_t(1), \dots, W_t(a), \dots, W_t(A)\}$  on the DSD support where each hypothesis has a different support

$$W_t(a) = \left( -\frac{a}{A} \nu_{D_{\max}}, \frac{a}{A} \nu_{D_{\max}} \right), \quad (\text{A.4})$$

$a \in \{1, \dots, A\}$ . Each hypothesis represents a subspace spanned by the columns of  $\mathbf{U}(W_t(a), M)$  which corresponds to the subspace  $\mathbf{U}^{(\mathcal{P})}(W_t(a), \mathcal{P})$  at pilot positions. The hypothesis test provides the hypothesis  $\hat{a} \in \{1, \dots, A\}$  that, according to the test, fits best to the current channel realization. For the sake of simplicity of notation we substitute  $\mathbf{U}^{(\mathcal{P})}(W_t(a), \mathcal{P})$  by  $\mathbf{U}_a^{(\mathcal{P})}$  in the following. We calculate the channel estimates on the pilot positions for each hypothesis according to [32, 119]

$$\hat{\mathbf{h}}_p(a) = \mathbf{U}_a^{(\mathcal{P})} \mathbf{U}_a^{(\mathcal{P})H} \mathbf{w}_p. \quad (\text{A.5})$$

The data error for hypothesis  $a$  can be expressed by

$$x_a = \frac{1}{N_p} \left\| \mathbf{w}_p - \hat{\mathbf{h}}_p(a) \right\|^2. \quad (\text{A.6})$$

We want to minimize the reconstruction error

$$z_a = \frac{1}{N_p} \left\| \mathbf{h}_p - \hat{\mathbf{h}}_p(a) \right\|^2 \quad (\text{A.7})$$

which cannot be directly observed at the receiver side since the actual channel  $\mathbf{h}_p$  is not known to the receiver. Knowing  $x_a$ , we are interested to obtain a probabilistic upper bound on  $z_a$  as

$$z_a < \bar{z}_a(x_a, p_1, p_2) \quad (\text{A.8})$$

that only depends on  $x_a$  and some constants  $p_1$  and  $p_2$ . This bound enables us to select the best hypothesis  $W_t(\hat{a})$ , i.e.,

$$\hat{a} = \underset{a \in \{1, \dots, A\}}{\operatorname{argmin}} \bar{z}_a(x_a, p_1, p_2). \quad (\text{A.9})$$

With the hypothesis  $W_t(\hat{a})$  and (5.20) we obtain  $\tilde{\mathbf{R}}_{\mathbf{h}}^{\hat{a}} \approx \check{\mathbf{R}}_{\mathbf{h}}^{\hat{a}}$  of the current channel realization that is used to obtain the channel estimate  $\hat{\mathbf{h}}_{\text{LMMSE}}^{\hat{a}}$  according to

$$\hat{\mathbf{h}}_{\text{LMMSE}}^{\hat{a}} = \tilde{\mathbf{R}}_{\mathbf{h}; \mathbf{h}_p}^{\hat{a}} \mathbf{D}_p^H \left( \mathbf{D}_p \tilde{\mathbf{R}}_{\mathbf{h}_p}^{\hat{a}} \mathbf{D}_p^H + \sigma_z^2 \mathbf{I}_{N_p} \right)^{-1} \mathbf{y}_p. \quad (\text{A.10})$$

The matrices  $\tilde{\mathbf{R}}_{\mathbf{h}; \mathbf{h}_p}^{\hat{a}}$  and  $\tilde{\mathbf{R}}_{\mathbf{h}_p}^{\hat{a}}$  are defined similarly as in Section 5.6.1. More detailed information on the hypothesis test can be found in [21, 32, 96].

## B List of Acronyms

We list all acronyms used in this thesis as follows

<b>3GPP</b>	3rd Generation Partnership Project
<b>ACF</b>	auto correlation function
<b>ADC</b>	analog-to-digital converter
<b>BEM</b>	basis-expansion model
<b>CE</b>	complex exponential
<b>CIR</b>	channel impulse response
<b>CP</b>	cyclic prefix
<b>CTF</b>	channel transfer function
<b>D2D</b>	device-to-device
<b>DAC</b>	digital-to-analog converter
<b>DC</b>	direct current
<b>DOD</b>	direction of departure
<b>DOA</b>	direction of arrival
<b>DPS</b>	discrete prolate spheroidal
<b>DPSWF</b>	discrete prolate spheroidal wave function
<b>DSD</b>	Doppler spectral density
<b>DSP</b>	digital signal processor
<b>ETSI</b>	European Telecommunications Standards Institute
<b>FIFO</b>	first-input first-output
<b>FFT</b>	fast Fourier transform
<b>FP</b>	fixed-point
<b>FPGA</b>	field programmable gate array
<b>GSCM</b>	geometry-based stochastic channel model
<b>GSM</b>	global system for mobile communications
<b>GPS</b>	global positioning system
<b>ICI</b>	inter-carrier interference
<b>IDFT</b>	inverse discrete Fourier transform
<b>IF</b>	intermediate frequency

<b>IFFT</b>	inverse fast Fourier transform
<b>ISI</b>	inter-symbol interference
<b>ITS</b>	intelligent transportation system
<b>MEC</b>	mobile edge computing
<b>MSE</b>	mean square error
<b>LLR</b>	log-likelihood ratio
<b>LO</b>	local oscillator
<b>LOS</b>	line-of-sight
<b>LMMSE</b>	linear minimum mean squared error
<b>LSF</b>	local scattering function
<b>LTE</b>	long term evolution
<b>LUT</b>	look-up table
<b>LTV</b>	linear time-variant
<b>MIMO</b>	multiple-input multiple-output
<b>MPC</b>	multi-path component
<b>MC</b>	Monte Carlo
<b>NI</b>	National Instruments
<b>NLOS</b>	non-line of sight
<b>OFDM</b>	orthogonal frequency division multiple access
<b>OTA</b>	over-the-air
<b>PC</b>	personal computer
<b>PDP</b>	power delay profile
<b>PER</b>	packet error rate
<b>QAM</b>	quadrature amplitude modulation
<b>QPSK</b>	quadrature phase shift keying
<b>RB</b>	resource block
<b>RBP</b>	resource block pair
<b>RF</b>	radio frequency
<b>RMS</b>	root mean square
<b>RSSI</b>	receive signal strength indicator
<b>RT</b>	ray tracing
<b>RX</b>	receiver
<b>SCME</b>	spatial channel model extended
<b>SDR</b>	software defined radio
<b>SISO</b>	single-input single-output
<b>SoCE</b>	sum of complex exponentials

---

<b>SNR</b>	signal-to-noise ratio
<b>SUT</b>	system-under test
<b>SSD</b>	soft sphere decoder
<b>TBWP</b>	time-bandwidth product
<b>TDL</b>	tap delay line
<b>TX</b>	transmitter
<b>UMTS</b>	universal mobile telecommunications systems
<b>UDP</b>	user datagram protocol
<b>URLLC</b>	ultra-reliable and low latency communication
<b>US</b>	uncorrelated-scattering
<b>USRP</b>	universal software radio peripheral
<b>VNA</b>	vector network analyzer
<b>ViL</b>	vehicle-in-the-loop
<b>V2X</b>	vehicle-to-everything
<b>VST</b>	vector signal transceiver
<b>VTD</b>	Virtual Test Drive
<b>WF</b>	Wiener filter
<b>WSS</b>	wide-sense-stationary
<b>WSSUS</b>	wide-sense-stationary uncorrelated-scattering



# Bibliography

- [1] ITU-R, “Framework and overall objectives of the future development of imt for 2020 and beyond,” Tech. Rep., 2015, [Online]. Available: <https://www.3GPP.org>.
- [2] A. F. Molisch, *Wireless Communications*, 2nd ed. Wiley Publishing, 2011.
- [3] Z. Xu, L. Bernadó, M. Gan, M. Hofer, T. Abbas, V. Shivaldova, K. Mahler, D. Smely, and T. Zemen, “Relaying for IEEE 802.11p at road intersection using a vehicular non-stationary channel model,” in *6th International Symposium Wireless Vehicular Communication (WIVEC 2014)*, Vancouver, Canada, Sep. 2014.
- [4] M. Shafi, A. F. Molisch, P. J. Smith, T. Haustein, P. Zhu, P. D. Silva, F. Tufveson, A. Benjebbour, and G. Wunder, “5G: A tutorial overview of standards, trials, challenges, deployment, and practice,” *IEEE Journal on Selected Areas in Communications*, vol. 35, no. 6, pp. 1201–1221, Jun. 2017.
- [5] ITU, “Minimum requirements related to technical performance for IMT-2020 radio interface(s),” Tech. Rep.
- [6] G. Fettweis and S. Alamouti, “5G: Personal mobile internet beyond what cellular did to telephony,” *IEEE Communications Magazine*, vol. 52, no. 2, pp. 140–145, Feb. 2014.
- [7] H. Chen, R. Abbas, P. Cheng, M. Shirvanimoghaddam, W. Hardjawana, W. Bao, Y. Li, and B. Vucetic, “Ultra-reliable low latency cellular networks: Use cases, challenges and approaches,” *IEEE Communications Magazine*, vol. 56, no. 12, pp. 119–125, Dec. 2018.
- [8] A. Mahmood, M. I. Ashraf, M. Gidlund, and J. Torsner, “Over-the-air time synchronization for urllc: Requirements, challenges and possible enablers,” in *2018 15th International Symposium on Wireless Communication Systems (ISWCS)*, Aug. 2018, pp. 1–6.

- [9] A. Frotzschler, U. Wetzker, M. Bauer, M. Rentschler, M. Beyer, S. Elspass, and H. Klessig, "Requirements and current solutions of wireless communication in industrial automation," in *2014 IEEE International Conference on Communications Workshops (ICC)*, Jun. 2014, pp. 67–72.
- [10] J. Sachs, G. Wikstrom, T. Dudda, R. Baldemair, and K. Kittichokechai, "5g radio network design for ultra-reliable low-latency communication," *IEEE Network*, vol. 32, no. 2, pp. 24–31, Mar. 2018.
- [11] M. Bennis, M. Debbah, and H. V. Poor, "Ultrareliable and low-latency wireless communication: Tail, risk, and scale," *Proceedings of the IEEE*, vol. 106, no. 10, pp. 1834–1853, Oct. 2018.
- [12] Y. Li, R. He, S. Lin, K. Guan, D. He, Q. Wang, and Z. Zhong, "Cluster-based nonstationary channel modeling for vehicle-to-vehicle communications," *IEEE Antennas and Wireless Propagation Letters*, vol. 16, pp. 1419–1422, Nov. 2017.
- [13] P. Popovski, J. J. Nielsen, C. Stefanovic, E. d. Carvalho, E. Strom, K. F. Trillingsgaard, A. Bana, D. M. Kim, R. Kotaba, J. Park, and R. B. Sorensen, "Wireless access for ultra-reliable low-latency communication: Principles and building blocks," *IEEE Network*, vol. 32, no. 2, pp. 16–23, Mar. 2018.
- [14] P. Popovski, C. Stefanovic, J. J. Nielsen, E. de Carvalho, M. Angjelichinoski, K. F. Trillingsgaard, and A. Bana, "Wireless access in ultra-reliable low-latency communication (URLLC)," *CoRR*, vol. abs/1810.06938, 2018. [Online]. Available: <http://arxiv.org/abs/1810.06938>
- [15] 3GPP, "ETSI TR 102 638 - Intelligent Transport Systems (ITS); Vehicular Communications; Basic Set of Applications; Definitions," Jun. 2009.
- [16] S. Sun, J. Hu, Y. Peng, X. Pan, L. Zhao, and J. Fang, "Support for vehicle-to-everything services based on lte," *IEEE Wireless Communications*, vol. 23, no. 3, pp. 4–8, Jun. 2016.
- [17] M. M. K. Tareq, O. Semiari, M. A. Salehi, and W. Saad, "Ultra reliable, low latency vehicle-to-infrastructure wireless communications with edge computing," *CoRR*, vol. abs/1808.06015, 2018. [Online]. Available: <http://arxiv.org/abs/1808.06015>
- [18] M. K. Abdel-Aziz, C. Liu, S. Samarakoon, M. Bennis, and W. Saad, "Ultra-reliable low-latency vehicular networks: Taming the age of information tail," *CoRR*, vol. abs/1811.03981, 2018. [Online]. Available: <http://arxiv.org/abs/1811.03981>

- [19] M. I. Ashraf, C.-F. Liu, M. Bennis, and W. Saad, "Towards low-latency and ultra-reliable vehicle-to-vehicle communication," in *2017 European Conference on Networks and Communications (EuCNC)*, Jun. 2017, pp. 1–5.
- [20] H. Ji, S. Park, J. Yeo, Y. Kim, J. Lee, and B. Shim, "Ultra-Reliable and Low-Latency Communications in 5G Downlink: Physical Layer Aspects," *IEEE Wireless Communications*, vol. 25, no. 3, pp. 124–130, Jun. 2018.
- [21] M. Hofer and T. Zemen, "Iterative Non-Stationary Channel Estimation for LTE Downlink Communications," in *2014 IEEE International Conference on Communications Workshops (ICC)*. IEEE, Jun. 2014, pp. 26–31.
- [22] M. Hofer, Z. Xu, and T. Zemen, "On the optimum number of hypotheses for adaptive reduced-rank subspace selection," in *2015 IEEE 82nd Vehicular Technology Conference (VTC2015-Fall)*, Sep 2015, pp. 1–5.
- [23] M. Hofer, Z. Xu, and T. Zemen, "Real-time channel emulation of a geometry-based stochastic channel model on a SDR platform," in *IEEE 18th Int. Works. Signal Process. Adv. Wireless Commun. (SPAWC)*, Sapporo, Japan, Jul. 2017.
- [24] M. Hofer, Z. Xu, D. Vlastaras, B. Schrenk, D. Loeschbrand, F. Tufvesson, and T. Zemen, "Validation of a real-time geometry-based stochastic channel model for vehicular scenarios," in *IEEE 87th Veh. Technol. Conf. (VTC-Spring)*, Jun. 2018.
- [25] M. Hofer, Z. Xu, D. Vlastaras, B. Schrenk, D. Loschenbrand, F. Tufvesson, and T. Zemen, "Real-time geometry-based wireless channel emulation," *IEEE Transactions on Vehicular Technology*, pp. 1–15, Feb. 2019.
- [26] M. Hofer, L. Bernadó, B. Rainer, Z. Xu, G. Temme, S. Khan, D. Behnecke, F. Utesch, M. Mahmood, and T. Zemen, "Evaluation of vehicle-in-the-loop tests for wireless v2x communication," in *2019 IEEE 90th Vehicular Technology Conference (VTC2019-Fall)*, Sep 2019 - to be presented, pp. 1–5.
- [27] M. Hofer and T. Zemen, "Method for Emulating a Radio Channel," *WO 2018/085769 A1*, May 2018.
- [28] F. Kaltenberger, "Low complexity simulation of wireless channels using discrete prolate spheroidal sequences," Ph.D. dissertation, Technical University Vienna, May 2007.
- [29] F. Hlawatsch and G. Matz, *Wireless Communications Over Rapidly Time-Varying Channels*, 1st ed. Academic Press, 2011.

- [30] P. Bello, “Characterization of randomly time-variant linear channels,” *IEEE Transactions on Communications Systems*, vol. 11, no. 4, pp. 360–393, Dec. 1963.
- [31] T. Zemen, “Wireless communications over time-variant channels,” Habilitation, TU Wien, 2012.
- [32] T. Zemen, L. Bernadó, N. Czink, and A. Molisch, “Iterative time-variant channel estimation for 802.11p using generalized discrete prolate spheroidal sequences,” *IEEE Trans. Veh. Technol.*, vol. 61, no. 3, pp. 1222–1233, Mar. 2012.
- [33] N. Czink, F. Kaltenberger, Y. Zhou, L. Bernadó, T. Zemen, and X. Yin, “Low-complexity geometry-based modeling of diffuse scattering,” *Proc. 4th Eur. Conf. Antennas Propag. (EuCAP)*, no. i, pp. 1–4, Apr. 2010.
- [34] D. Tse and P. Viswanath, *Fundamentals of Wireless Communication*. New York, NY, USA: Cambridge University Press, 2005.
- [35] P. Almers, E. Bonek, A. Burr, N. Czink, M. Debbah, V. Degli-Esposti, H. Hofstetter, P. Kyösti, D. Laurenson, G. Matz, A. Molisch, C. Oestges, and H. Özcelik, “Survey of channel and radio propagation models for wireless MIMO systems,” *EURASIP J. Wireless Commun. Netw.*, vol. 2007, no. 1, p. 019070, Feb. 2007.
- [36] G. Matz, “Doubly underspread non-WSSUS channels: Analysis and estimation of channel statistics,” in *IEEE 4th Int. Works. Signal Process. Adv. Wireless Commun. (SPAWC)*, Jun. 2003, pp. 190–194.
- [37] —, “On non-wssus wireless fading channels,” *IEEE Trans. Wireless Commun.*, vol. 4, no. 5, pp. 2465–2478, Sep. 2005.
- [38] A. Paier, T. Zemen, L. Bernadó, G. Matz, J. Karedal, N. Czink, C. Dumard, F. Tufvesson, A. F. Molisch, and C. F. Mecklenbrauker, “Non-wssus vehicular channel characterization in highway and urban scenarios at 5.2ghz using the local scattering function,” in *2008 International ITG Workshop on Smart Antennas*, Feb. 2008, pp. 9–15.
- [39] L. Bernadó, T. Zemen, F. Tufvesson, A. F. Molisch, and C. F. Mecklenbrauker, “Delay and Doppler spreads of nonstationary vehicular channels for safety-relevant scenarios,” *IEEE Trans. Veh. Technol.*, vol. 63, no. 1, pp. 82–93, Jan. 2014.

- [40] C. F. Mecklenbrauker, A. F. Molisch, J. Karedal, F. Tufvesson, A. Paier, L. Bernadó, T. Zemen, O. Klemp, and N. Czink, “Vehicular channel characterization and its implications for wireless system design and performance,” *Proc. IEEE*, vol. 99, no. 7, pp. 1189–1212, Jul. 2011.
- [41] T. Zemen, L. Bernado, N. Czink, and A. F. Molisch, “Iterative time-variant channel estimation for 802.11p using generalized discrete prolate spheroidal sequences,” *IEEE Transactions on Vehicular Technology*, vol. 61, no. 3, pp. 1222–1233, Mar. 2012.
- [42] L. Bernado, “Non-stationarity in vehicular wireless channels,” Ph.D. dissertation, Technical University Vienna, May 2012.
- [43] A. F. Molisch, F. Tufvesson, J. Karedal, and C. F. Mecklenbrauker, “A survey on vehicle-to-vehicle propagation channels,” *IEEE Wireless Communications*, vol. 16, no. 6, pp. 12–22, Dec. 2009.
- [44] A. Molisch and F. Tufvesson, “Propagation channel models for next-generation wireless communications systems,” *IEICE Transactions on Communications*, vol. E97B, no. 10, pp. 2022–2034, 2014.
- [45] W. Viriyasitavat, M. Boban, H. Tsai, and A. Vasilakos, “Vehicular communications: Survey and challenges of channel and propagation models,” *IEEE Vehicular Technology Magazine*, vol. 10, no. 2, pp. 55–66, Jun. 2015.
- [46] P. Unterhuber, S. Pfletschinger, S. Sand, M. Soliman, T. Jost, A. Arriola, I. Val, C. Cruces, J. Moreno, J. P. García-nieto, C. Rodríguez, M. Berbineau, E. Echeverría, and I. Baz, “A survey of channel measurements and models for current and future railway communication systems,” *Mob Inf. Syst*, vol. 2016, no. 7308604, p. 14, Jun. 2016.
- [47] J. Maurer, “Strahlenoptisches Kanalmodell fuer die Fahrzeug-Fahrzeug-Funkkommunikation,” Ph.D. dissertation, University Karlsruhe, 2005.
- [48] J. Maurer, T. Fugen, and W. Wiesbeck, “Narrow-band measurement and analysis of the inter-vehicle transmission channel at 5.2 GHz,” in *IEEE 55th Veh. Technol. Conf. (VTC-Spring)*, vol. 3, May 2002, pp. 1274–1278 vol.3.
- [49] J. Maurer, T. M. Schafer, and W. Wiesbeck, “A realistic description of the environment for inter-vehicle wave propagation modelling,” in *IEEE 54th Veh. Technol. Conf. (VTC-Fall)*, vol. 3, Oct. 2001, pp. 1437–1441 vol.3.

- [50] J. Maurer, T. Fugen, T. Schafer, and W. Wiesbeck, "A new inter-vehicle communications (IVC) channel model," in *IEEE 60th Veh. Technol. Conf. (VTC-Fall)*, vol. 1, Sept 2004, pp. 9–13 Vol. 1.
- [51] Z. Yun and M. F. Iskander, "Ray tracing for radio propagation modeling: Principles and applications," *IEEE Access*, vol. 3, pp. 1089–1100, Jul. 2015.
- [52] M. Gan, "Accurate and low-complexity ray tracing channel modeling," Ph.D. dissertation, Technical University Vienna, Austria, Nov. 2015.
- [53] G. Durgin, N. Patwari, and T. S. Rappaport, "An advanced 3d ray launching method for wireless propagation prediction," in *1997 IEEE 47th Vehicular Technology Conference. Technology in Motion*, vol. 2, May 1997, pp. 785–789 vol.2.
- [54] G. Acosta-Marum and M. A. Ingram, "Six time- and frequency- selective empirical channel models for vehicular wireless lans," *IEEE Vehicular Technology Magazine*, vol. 2, no. 4, pp. 4–11, Dec. 2007.
- [55] W. Weichselberger, M. Herdin, H. Ozcelik, and E. Bonek, "A stochastic mimo channel model with joint correlation of both link ends," *IEEE Transactions on Wireless Communications*, vol. 5, no. 1, pp. 90–100, Jan. 2006.
- [56] A. A. M. Saleh and R. Valenzuela, "A statistical model for indoor multipath propagation," *IEEE Journal on Selected Areas in Communications*, vol. 5, no. 2, pp. 128–137, Feb. 1987.
- [57] R. H. Clarke, "A statistical theory of mobile-radio reception," *The Bell System Technical Journal*, vol. 47, no. 6, pp. 957–1000, Jul. 1968.
- [58] M. Faili, "COST 207 - Digital land mobile radio communications," European Union, Tech. Rep., 1989.
- [59] ITU, "Guidelines for Evaluation of Radio Transmission Technologies for IMT-2000 System," 1997, Recommendation ITU-R M.1225.
- [60] J. Karedal, F. Tufvesson, N. Czink, A. Paier, C. Dumard, T. Zemen, C. F. Mecklenbräuker, and A. F. Molisch, "A geometry-based stochastic MIMO model for vehicle-to-vehicle communications," *IEEE Trans. Wireless Commun.*, vol. 8, no. 7, pp. 3646–3657, Jul. 2009.
- [61] M. Walter, D. Shutin, and U. Fiebig, "Delay-dependent doppler probability density functions for vehicle-to-vehicle scatter channels," *IEEE Transactions on Antennas and Propagation*, vol. 62, no. 4, pp. 2238–2249, Apr. 2014.

- [62] Q. Zhu, C.-X. Wang, Y. Tan, X. Chen, H. Li, Q. Wu, and Y. Fu, "A Novel 3D Non-Stationary Wireless MIMO Channel Simulator and Hardware Emulator," *IEEE Transactions on Communications*, vol. 66, no. 9, pp. 3865–3878, Apr. 2018.
- [63] K. Jiang, X. Chen, Q. Zhu, W. Zhong, Y. Wang, X. Yu, and B. Chen, "A geometry-based 3d non-stationary uav-mimo channel model allowing 3d arbitrary trajectories," in *2018 10th International Conference on Wireless Communications and Signal Processing (WCSP)*, Oct 2018, pp. 1–6.
- [64] P. Kyösti, J. Meinilä, L. Hentila, X. Zhao, T. Jämsä, C. Schneider, M. Narandzic, M. Milojević, A. Hong, J. Ylitalo, V.-M. Holappa, M. Alatossava, R. Bultitude, Y. Jong, and T. Rautiainen, "Winner ii channel models," *IST-4-027756 WINNER II D1.1.2 V1.2*, 02 2008.
- [65] F. Ademaj, M. K. Mueller, S. Schwarz, and M. Rupp, "Modeling of spatially correlated geometry-based stochastic channels," in *2017 IEEE 86th Vehicular Technology Conference (VTC-Fall)*, Sep. 2017, pp. 1–6.
- [66] S. Wu, C. Wang, e. M. Aggoune, M. M. Alwakeel, and X. You, "A general 3-d non-stationary 5g wireless channel model," *IEEE Transactions on Communications*, vol. 66, no. 7, pp. 3065–3078, July 2018.
- [67] Y. Yang, Q. Zhu, W. Li, X. Chen, W. Zhong, X. Yu, and K. Mao, "A general 3d non-stationary twin-cluster model for vehicle-to-vehicle mimo channels," in *2018 10th International Conference on Wireless Communications and Signal Processing (WCSP)*, Oct 2018, pp. 1–6.
- [68] K. Mahler, W. Keusgen, F. Tufvesson, T. Zemen, and G. Caire, "Tracking of wideband multipath components in a vehicular communication scenario," *IEEE Transactions on Vehicular Technology*, vol. 66, no. 1, pp. 15–25, Jan 2017.
- [69] K. Mahler, "Wideband Propagation Channel in Vehicular Communication Scenarios," Ph.D. dissertation, Technical University of Berlin, Germany, October 2016.
- [70] Accessed: 2019-04-15. [Online]. Available: <https://www.keysight.com/>
- [71] Accessed: 2019-04-15. [Online]. Available: <https://www.spirent.com/>
- [72] Accessed: 2019-04-15. [Online]. Available: <https://www.anritsu.com/>

- [73] 3GPP, “ETSI TR 138 901 - 5G; Study on channel model for frequencies from 0.5 to 100 GHz,” 2017.
- [74] ITU-R, “Report ITU-R M.2135-1 - Guidelines for evaluation of radio interface technologies for IMT-Advanced,” December 2009.
- [75] (2013, May) Real-Time MIMO Channel Emulation on the NI PXIe-5644R. National Instruments. Accessed: 2016-01-15. [Online]. Available: <http://www.ni.com/example/31556/en/>
- [76] D. Vlastaras, S. Malkowsky, and F. Tufvesson, “Stress test of vehicular communication transceivers using software defined radio,” in *IEEE 81st Veh. Technol. Conf. (VTC-Spring)*, vol. 41, no. 2, May 2015, pp. 1–4.
- [77] G. Ghiaasi, M. Ashury, D. Valstaras, M. Hofer, Z. Xu, and T. Zemen, “Real-time vehicular channel emulator for future conformance tests of wireless its modems,” in *Proc. 10th Eur. Conf. Antennas Propag. (EuCAP)*, Apr. 2016.
- [78] “MKG Sys,” Accessed: 2016-01-15. [Online]. Available: <https://www.mkgsys.com/>
- [79] T. Fernández-Caramés, M. González-López, and L. Castedo, “FPGA-based vehicular channel emulator for real-time performance evaluation of IEEE 802.11p transceivers,” *EURASIP J. Wirel. Commun. Netw.*, vol. 2010, no. 1, p. 607467, Feb. 2010.
- [80] J. Matai, P. Meng, L. Wu, B. Weals, and R. Kastner, “Designing a hardware in the loop wireless digital channel emulator for software defined radio,” in *2012 Int. Conf. Field-Prog. Technol*, Dec. 2012, pp. 206–214.
- [81] T. Blazek, C. Mecklenbräuker, G. Ghiaasi, D. Smely, and M. M. Ashury, “Vehicular channel models: A system level performance analysis of tapped delay line models,” in *IEEE Proc. 15th Int Conf. on ITS Telecommun.*, May 2017, Warsaw, Poland.
- [82] G. Ghiaasi, T. Blazek, M. Ashury, S. R. Ramalho, and C. Mecklenbräuker, “Real-time emulation of nonstationary channels in safety-relevant vehicular scenarios,” *Hindawi*, Feb. 2018.
- [83] A. Schwind, P. Berlt, M. Lorenz, C. Schneider, and M. A. Hein, “Implementation of a mimo channel emulator for over-the-air lte testing using software defined radio,” in *2018 11th German Microwave Conference (GeMiC)*, Mar. 2018, pp. 307–310.

- [84] L. C. Jäger, P. Berlt, C. Bornkessel, and M. A. Hein, “Distributed spatial channel emulation for virtual drive testing based on multiple software-defined radios,” in *Proc. 13th Eur. Conf. Antennas Propag. (EuCAP)*, Apr. 2019, pp. 1–5.
- [85] Z. Xu, M. Gan, and T. Zemen, “Cluster-based non-stationary vehicular channel model,” in *Proc. 10th Eur. Conf. Antennas Propag. (EuCAP)*, Apr. 2016, pp. 1–5.
- [86] Z. Xu, M. Gan, C. F. Mecklenbraeuer, and T. Zemen, “Cluster spreads for time-variant vehicular channels,” in *Proc. 9th Eur. Conf. Antennas Propag. (EuCAP)*, May 2015, pp. 1–5.
- [87] 3GPP, “ETSI TS 103 257 - Intelligent Transport Systems (ITS); Access Layer; ITS-G5 Channel Models and Performance Analysis Framework,” Mar. 2017.
- [88] I. Val, F. Casado, P. M. Rodriguez, and A. Arriola, “Fpga-based wideband channel emulator for evaluation of wireless sensor networks in industrial environments,” in *Proceedings of the 2014 IEEE Emerging Technology and Factory Automation (ETFA)*, Sep. 2014, pp. 1–7.
- [89] L. Bernadó, T. Zemen, F. Tufvesson, A. F. Molisch, and C. F. Mecklenbräuer, “Time- and frequency-varying  $K$ -factor of non-stationary vehicular channels for safety-relevant scenarios,” *IEEE Trans. Intell. Transp. Syst.*, vol. 16, no. 2, pp. 1007–1017, Apr. 2015.
- [90] M. Walter, T. Zemen, and D. Shutin, “Empirical relationship between local scattering function and joint probability density function,” in *2015 IEEE 26th Int. Symp. Pers. Indoor Mob. Radio Commun. (PIMRC)*, Aug. 2015, pp. 542–546.
- [91] M. Walter, D. Shutin, and A. Dammann, “Time-variant Doppler PDFs and characteristic functions for the vehicle-to-vehicle channel,” *IEEE Trans Veh. Technol.*, vol. PP, no. 99, pp. 1–1, Jun. 2017.
- [92] F. Kaltenberger, T. Zemen, and C. W. Ueberhuber, “Low-complexity geometry-based MIMO channel simulation,” *EURASIP J. Adv. Signal Process.*, vol. 2007, no. 1, p. 095281, Dec. 2007.
- [93] F. Kaltenberger, G. Steinböck, G. Humer, and T. Zemen, “Low-complexity geometry based MIMO channel emulation,” *European Space Agency, (Special Publication) ESA SP*, vol. 626 SP, no. Oct., 2006.

- [94] D. Slepian, “Prolate spheroidal wave functions, Fourier analysis, and uncertainty-V: The discrete case,” *Bell Syst. Techn. J.*, vol. 57, no. 5, pp. 1371–1430, May 1978.
- [95] F. Kaltenberger, T. Zemen, and C. Ueberhuber, “Low-complexity doubly selective channel simulation using multidimensional discrete prolate spheroidal sequences,” *15th IST Mobile Wireless Commun. Summit (IST SUMMIT)*, 2006.
- [96] T. Zemen, C. Mecklenbrauker, F. Kaltenberger, and B. Fleury, “Minimum-energy band-limited predictor with dynamic subspace selection for time-variant flat-fading channels,” *IEEE Trans. Signal Process.*, vol. 55, no. 9, pp. 4534–4548, Sep. 2007.
- [97] T. Zemen and A. Molisch, “Adaptive reduced-rank estimation of nonstationary time-variant channels using subspace selection,” *IEEE Trans. Veh. Technol.*, vol. 61, no. 9, pp. 4042–4056, Nov. 2012.
- [98] *Device Specifications, NI USRP-2594R, 10 MHz to 6 GHz Tunable RF Transceiver*, National Instruments.
- [99] D. J. Thomson, “Spectrum estimation and harmonic analysis,” *Proc. IEEE*, vol. 70, no. 9, pp. 1055–1096, Sep. 1982.
- [100] L. Bernado, T. Zemen, A. Paier, J. Karedal, and B. H. Fleury, “Parametrization of the local scattering function estimator for vehicular-to-vehicular channels,” in *2009 IEEE 70th Veh. Technol. Conf. (VTC-Fall)*, Sep. 2009, pp. 1–5.
- [101] L. Bernadó, T. Zemen, F. Tufvesson, A. F. Molisch, and C. F. Mecklenbraeuker, “The (in-) validity of the WSSUS assumption in vehicular radio channels,” in *2012 IEEE 23rd Int. Symp. Pers. Indoor Mob. Radio Commun. (PIMRC)*, Sep. 2012, pp. 1757–1762.
- [102] D. B. Percival and A. T. Walden, *Spectral Analysis for Physical Applications: Multitaper and Conventional Univariate Techniques*. Cambridge University Press, 1993.
- [103] E. Zochmann, C. Mecklenbraeuker, M. Lerch, S. Pratschner, M. Hofer, D. Loeschenbrand, J. Blumenstein, S. Sangodoyin, G. Artner, S. Caban, T. Zemen, A. Prokes, M. Rupp, and A. F. Molisch, “Measured delay and Doppler profiles of overtaking vehicles at 60 GHz,” in *Proc. 12th Eur. Conf. Antennas Propag. (EuCAP)*, Apr. 2018.

- [104] A. Paier, L. Bernadó, J. Karedal, O. Klemp, and A. Kwoczek, “Overview of vehicle-to-vehicle radio channel measurements for collision avoidance applications,” in *IEEE 71st Veh. Technol. Conf. (VTC)*, Taipei, Taiwan, May 2010.
- [105] METIS. (2015, July) Deliverable D1.4 - METIS channel models. [Online]. Available: [https://www.metis2020.com/wp-content/uploads/METIS\\_D1.4\\_v3.pdf](https://www.metis2020.com/wp-content/uploads/METIS_D1.4_v3.pdf)
- [106] J. E. Berg, “A recursive method for street microcell path loss calculations,” in *IEEE 1995 6th Int. Symp. Pers. Indoor Mob. Radio Commun. (PIMRC)*, vol. 1, Sep. 1995, pp. 140–143 vol.1.
- [107] L. Bernado, A. Roma, A. Paier, T. Zemen, N. Czink, J. Karedal, A. Thiel, F. Tufvesson, A. F. Molisch, and C. F. Mecklenbrauker, “In-tunnel vehicular radio channel characterization,” in *2011 IEEE 73rd Veh. Technol. Conf. (VTC-Spring)*, May 2011, pp. 1–5.
- [108] T. Bokc, M. Maurer, and G. Farber, “Validation of the vehicle in the loop (vil); a milestone for the simulation of driver assistance systems,” in *2007 IEEE Intelligent Vehicles Symposium*, Jun. 2007, pp. 612–617.
- [109] J. Bonney, G. Bowering, R. Marotz, and K. Swanson, “Hardware-in-the-loop emulation of mobile wireless communication environments,” in *2008 IEEE Aerospace Conference*, Mar. 2008, pp. 1–9.
- [110] N. Franchi, G. Fischer, and R. Weigel, “Radio hardware in-the-loop emulation for testing vehicular communication systems,” in *2013 IEEE 5th International Symposium on Wireless Vehicular Communications (WiVeC)*, Jun. 2013, pp. 1–4.
- [111] “IEEE Std. 802.11p-2010, Part 11: Wireless LAN Medium Access Control (MAC) and Physical Layer (PHY) specifications: Amendment 7: Wireless Access in Vehicular Environment,” *IEEE Std*, Jul. 2010.
- [112] M. Fischer, A. Richter, J. Schindler, J. Plättner, G. Temme, J. Kelsch, D. Assmann, and F. Köster, “Modular and scalable driving simulator hardware and software for the development of future driver assistance and automation systems,” *New Developments in Driving Simulation Design and Experiments*, pp. 223–229, 2014.
- [113] J. Gacnik, O. Häger, M. Hannibal, and F. Köster, “Service-oriented architecture for future driver assistance systems,” in *Congress proceedings // FISITA World Automotive Congress : 14 - 19 September 2008, Munich, Germany /*

ed. by ATZ/ATZautotechnology ; Vol. 1: Mobility concepts, man machine interface, process challenges, virtual reality, 2008.

- [114] A. Adegoke, D. S. David, and S. Salami, "Vegetation attenuation and its dependence on foliage density," *European Journal of Engineering and Technology*, vol. 4, no. 3, 2016.
- [115] Y. Mao, C. You, J. Zhang, K. Huang, and K. B. Letaief, "A survey on mobile edge computing: The communication perspective," *IEEE Communications Surveys Tutorials*, vol. 19, no. 4, pp. 2322–2358, Fourthquarter 2017.
- [116] ETSI, "Mobile Edge Computing - Introductory White Paper," Tech. Rep., 2014. [Online]. Available: [https://portal.etsi.org/Portals/0/TBpages/MEC/Docs/Mobile-edge-Computing\\_-\\_Introductory\\_Technical\\_White\\_Paper\\_V1%2018-09-14.pdf](https://portal.etsi.org/Portals/0/TBpages/MEC/Docs/Mobile-edge-Computing_-_Introductory_Technical_White_Paper_V1%2018-09-14.pdf)
- [117] H. Li, G. Shou, Y. Hu, and Z. Guo, "Mobile edge computing: Progress and challenges," in *2016 4th IEEE International Conference on Mobile Cloud Computing, Services, and Engineering (MobileCloud)*, Mar. 2016, pp. 83–84.
- [118] T. Zemen and C. Mecklenbrauker, "Time-Variant Channel Estimation Using Discrete Prolate Spheroidal Sequences," *IEEE Transactions on Signal Processing*, vol. 53, no. 9, pp. 3597–3607, Aug. 2005.
- [119] S. Beheshti and M. Dahleh, "A new information-theoretic approach to signal denoising and best basis selection," *Signal Processing, IEEE Transactions on*, vol. 53, no. 10, pp. 3613–3624, Oct. 2005.
- [120] 3GPP, "Technical Specification Group Radio Access Network; (E-UTRA) and (E-UTRAN); Physical Channels and Modulation; (Release 8)," Tech. Rep., Sep. 2008. [Online]. Available: <http://www.3gpp.org/ftp/Specs/html-info/36211.htm>
- [121] C. Studer, M. Wenk, A. Burg, and H. Bolcskei, "Soft-Output Sphere Decoding: Performance and Implementation Aspects," in *Fortieth Asilomar Conference on Signals, Systems and Computers, 2006. ACSSC '06.*, Oct. 2006, pp. 2071–2076.
- [122] T. Zemen, C. Mecklenbrauker, J. Wehinger, and R. Muller, "Iterative Joint Time-Variant Channel Estimation and Multi-User Detection for MC-CDMA," *IEEE Transactions on Wireless Communications*, vol. 5, no. 6, pp. 1469–1478, Jun. 2006.

- 
- [123] M. Tuechler, A. Singer, and R. Koetter, "Minimum Mean Squared Error Equalization Using A Priori Information," *Signal Processing, IEEE Transactions on*, vol. 50, no. 3, pp. 673–683, Aug. 2002.
- [124] 3GPP, "Technical Specification Group Radio Access Network; (E-UTRA) and (E-UTRAN); Overall Description; stage 2," Tech. Rep., Sep. 2008. [Online]. Available: <http://www.3gpp.org/ftp/Specs/html-info/36300.htm>
- [125] W. Haselmayr, D. Schellander, and A. Springer, "Iterative Channel Estimation and Turbo Equalization for Time-Varying Channels in a Coded OFDM-LTE System for 16-QAM and 64-QAM," in *IEEE 21st International Symposium on Personal Indoor and Mobile Radio Communications (PIMRC)*, Sep. 2010, pp. 614–618.
- [126] X. Mestre, "Improved Estimation of Eigenvalues and Eigenvectors of Covariance Matrices Using Their Sample Estimates," *IEEE Transactions on Information Theory*, vol. 54, no. 11, pp. 5113–5129, Oct. 2008.
- [127] A. Ispas, M. Dorpinghaus, G. Ascheid, and T. Zemen, "Characterization of non-stationary channels using mismatched wiener filtering," *Signal Processing, IEEE Transactions on*, vol. 61, no. 2, pp. 274–288, Jan. 2013.